Marquette University

e-Publications@Marquette

Failure Mechanisms and Key Parameters of FRP Debonding from Cracked Concrete Beams

Tayyebeh Mohammadi
Marquette University

FAILURE MECHANISMS AND KEY PARAMETERS OF FRP DEBONDING FROM CRACKED CONCRETE BEAMS

by

Tayyebeh Mohammadi, B.S., M.S.

A Dissertation submitted to the Faculty of the Graduate School,
Marquette University,
in Partial Fulfillment of the Requirements for
the Degree of Doctor of Philosophy

Milwaukee, Wisconsin

August 2014

ABSTRACT
FAILURE MECHANISMS AND KEY PARAMETERS OF FRP DEBONDING FROM CRACKED CONCRETE BEAMS

Tayyebeh Mohammadi, B.S., M.S.

Marquette University, 2014

Intermediate crack (IC) induced debonding failure of Fiber Reinforced Polymer (FRP)-strengthened reinforced concrete beams starts at the tip of flexural/shear cracks within the shear span and propagates towards the FRP plate termination. In this study, experimental and numerical programs are performed to characterize and predict the failure mechanisms of IC debonding failure, and identify the key parameters affecting such failure. It is found that the bond-slip relation obtained from the pullout test does not represent the bond-slip relation of the FRP/concrete interface in the FRP-strengthened concrete beams, and it cannot be directly used for predicting the load capacity of the FRP-strengthened concrete beams. A mathematical and systematic method is also successfully established to predict the variation of the FRP-bonded concrete specimens' capacities.

In the experimental program, the bond-slip behavior of the FRP/concrete interface is obtained by single shear pullout and beam tests. In the beam specimens, a notch at the mid-span of the beam represents the main flexural/shear crack. In order to study the sensitivity of the IC debonding failure to the location of the major flexural/shear crack, the notch is located at different locations along the shear span of the beam. In all beam specimens, a concrete wedge located at the edge of the notch detached with the FRP debonding failure. This phenomenon shows that the initiation of debonding is due to a diagonal crack formation close to the major flexural/shear crack inside the concrete.

Numerical analyses are performed using the experimentally-obtained bond-slip relations to model the shear pullout and beam tests. The application of concrete damaged plasticity model in XFEM is proposed to model the constitutive behavior of concrete. The numerical analyses show that the boundary conditions of the concrete block at the loaded end play an important role in the resulting bond-slip relationship and stress state of the FRP/concrete interface in the pullout tests. According to the numerical analyses, the diagonal crack formation observed in the experiments is due to a local moment at the tip of the notch. This causes the difference in behaviors of beam specimens than pullout specimens.

The variation of localized FRP stiffness and concrete strength is combined into a single parameter as the variation of the interfacial fracture energy. A systematic method using the concept of Brownian motion is successfully established to determine the range of the interfacial fracture energies and load carrying capacities of the FRP-bonded concrete specimens.

ACKNOWLEDGMENTS

Tayyebeh Mohammadi, B.S., M.S.

TABLE OF CONTENTS

iv

LIST OF TABLES

LIST OF FIGURES

Chapter 1 Introduction

The serviceability and safety of building and bridge structures may gradually degrade due to long term use, natural environmental deterioration, poor initial design and/or construction, increased design loads, extreme events such as earthquakes, and/or lack of maintenance. More than 30 percent of the existing bridges in the United States are in need of various levels of repairs, rehabilitation, or replacement (FHWA 2011).

The effects of severe winters and the extensive use of road salt often worsen the deterioration causing spalling of concrete and exposure of the steel reinforcement. In addition to the bridge superstructure elements, there is also need to address deteriorating elements in parking structures, masonry walls, load-bearing walls and even concrete facades. It is needed to use materials that are not susceptible to the same causes that trigged the deterioration in the first instance. Since the rebuilding of old infrastructure is very expensive and time consuming, cost-efficient and durable techniques of strengthening/rehabilitating are needed.

There is a growing interest in the use of Fiber Reinforced Polymer (FRP) composite materials for the strengthening and retrofitting of concrete beams. This strengthening technique involves the bonding of a FRP plate/sheet to the tensile face of the beam in order to provide additional external reinforcement. FRPs are composite materials comprised of high strength fibers embedded in a polymer matrix. The result is a rigid material that has high strength and stiffness, yet light weight. The fibers provide the stiffness and strength of the composite in the direction of their primary orientation while

the polymer matrix holds the fibers in alignment, transfers loads between fibers and serves to protect the fibers from mechanical and environmental damages.

The first time that carbon fiber reinforced polymers (CFRP) were used to retrofit a damaged bridge was in Switzerland in 1991(Meier 1995). Since then, externally bonded FRP plate/sheet for repair/strengthening of concrete structures have been widely used in civil engineering due to the good material properties of FRP for this application (e.g., Bakis et al. 2002, Teng et al. 2002, Bank 2006, Hollaway 2010). Main advantages of FRP composites are their very high strength- and stiffness-to-weight ratios, corrosion resistance, easy installation, and outstanding fatigue behavior, (ACI 440.2R 2008). Although the material cost of FRP composites is higher than traditional strengthening material such as steel, their life cycle cost including: equipment, time, detours, and the most important maintenance is lower.

Along with the advantages, the use of externally bonded FRP plates/sheets introduces a new and unique mode of failure in the strengthened structures, which has not been fully understood. Failure of FRP-strengthened reinforced concrete (RC) beams subjected to flexural loading is often caused by debonding of FRP with a thin layer of concrete that is a sudden and brittle failure (e.g., Aprile et al. 2001, Buyukozturk et al. 2004, Oehlers and Seracino 2004, Rosenboom and Rizkalla 2008, Teng and Chen 2009). Because of the FRP debonding, the capacity of the FRP plate/sheet may not be fully engaged and the utilization of FRP materials is relatively inefficient as compared to the hypothetical case having 'perfect bond'. Therefore, characterizing and prediction of the failure mechanisms of FRP debonding from strengthened concrete beams, and identifying the key parameters affecting such failure, are required.

1.1 Debonding Failure of Concrete Members Strengthened with FRP

In civil infrastructure applications, FRP composite materials have been mainly used for rehabilitation or repair of deteriorated structures. When used for these purposes, FRP is usually bonded to the exterior surface or mounted inside but close to the surface of the repaired member (so called, near-surface mounted or NSM). Debonding along the FRP/concrete interface is one of the principal failure mechanisms of concrete beams externally strengthened with FRP.

Generally, FRP debonding along the FRP/concrete interface can be categorized into two main failure modes (Teng et al. 2003) as shown in Figure 1.1. The first failure mode is plate-end (PE) debonding (Figure 1.1a) which initiates at the ends of the FRP plate and propagates in the direction of increasing moment. This failure mode results from the high interface stresses at the end of discontinuities. Many studies have been carried out to investigate and predict this type of debonding failure mode (e.g., Abdelouahed 2006, Yao and Teng 2007, Teng and Yao 2007, Tounsi et al. 2009). End wrapping and mechanical anchorage have been found to be efficient methods of mitigating the PE debonding failure in FRP repaired or retrofitted concrete beams. The second failure mode is the intermediate crack induced debonding (IC debonding) which initiates at a flexural/shear crack (intermediate crack) in the concrete within the shear span and propagates towards the plate end in the direction of decreasing moment as shown schematically in Figure 1.1b. This type of FRP debonding failure, unlike PE debonding, is difficult to prevent. Therefore, it must be taken into consideration in the design process and addressed as a limit state.
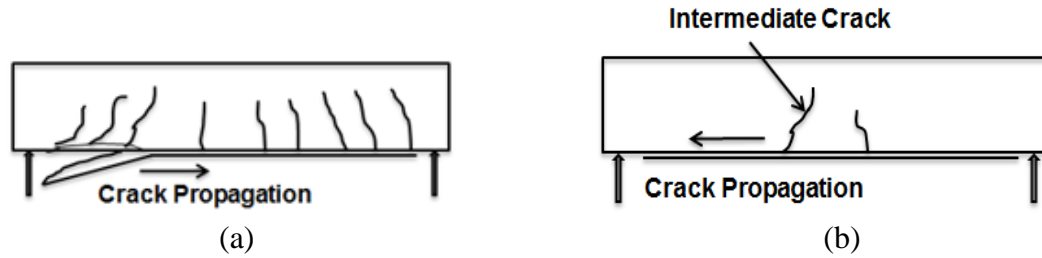
Figure 1.1 FRP debonding failure: (a) PE debonding, (b) IC debonding

There are no universally accepted standards for determining bond capacity between FRP and concrete. Currently, the bond between FRP and concrete is tested by applying shear stress to the FRP/concrete interface of a FRP bonded concrete specimen. According to Chen and Teng (2001) and Chen et al. (2001), suitable general test methods include: double pullout tests (e.g., Brosens and Gemert 1997, Yoshizawa et al. 2000, Nakaba et al. 2001, Serbescu et al. 2013), single shear pullout tests (e.g., Chajes et al. 1996, Taljsten 1997, Bizindavyi and Neale 1999, Leung and Tung 2006, Mazzotti et al. 2008), and beam tests (e.g., Fukuzawa et al. 1997, Benjeddou et al. 2007, Gartner et al. 2011). These test methods are presented in Figures 1.2a through c. There are a number of variations of the beam tests; these are summarized by Harries et al. (2012).

The test results are applied to determine the bond-slip (interface shear stress vs. relative slip between FRP and concrete) relationship of FRP/concrete interfaces. Such a relationship is then used to model and predict the debonding failure of the FRP/concrete joints. A typical bond-slip curve is shown in Figure 1.3. The area under the bond-slip curve is defined as the mode II fracture energy, G_{fII}, which is a property of the FRP-concrete system.
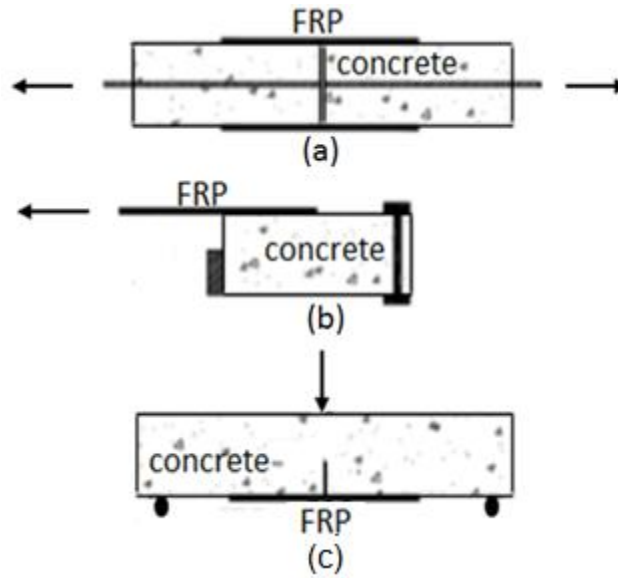
Figure 1.2 Bond test methods: (a) double pullout, (b) single pullout, and (c) beam
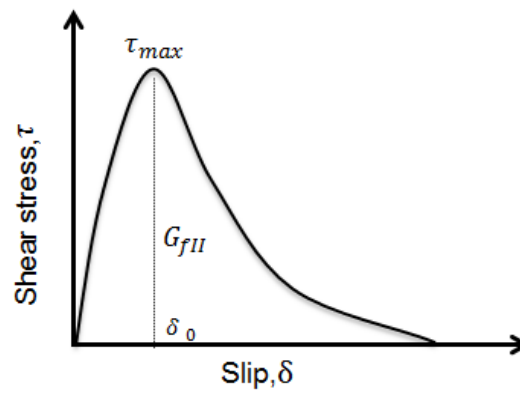
Figure 1.3 Typical bond-slip curve of a FRP/concrete interface

In the double or single pullout test, the in-plane shear stress is applied to the FRP/concrete interface by applying a uniaxial tension load in the plane of the FRP, typically in the strong or longitudinal direction of the FRP fiber orientation. The tensile strain gradient in the FRP (representing the shear strain along the interface) is recorded and is used to determine the bond-slip relation. Often the obtained bond-slip relation is

used for nonlinear fracture mechanics or cohesive crack models in numerical analyses to predict FRP debonding from the concrete substrate.

IC debonding failure in FRP-strengthened RC beams is due to the development of high interfacial stresses at locations of flexure/shear cracks in concrete. Although the interface is usually modeled as an FRP/concrete joint subjected to shear, the real loading condition at the crack tip includes both shear and normal stresses. The use of pullout test results to predict the behavior of FRP-strengthened concrete beams may not represent the *in situ* phenomenon. Therefore, some studies have used beam bond tests to study the debonding behavior in FRP-strengthened RC beams. In this study, the application of shear test results for predicting the IC debonding failure in FRP-strengthened concrete beams is investigated experimentally and numerically.

1.2 Research Objectives

The overall objective of this dissertation is to characterize and predict the failure mechanisms of IC debonding failure, and identify the key parameters affecting such failure. In order to achieve this objective, experimental tests and finite element simulations are performed on FRP bonded concrete specimens.

Experiments are designed to obtain the bond-slip behavior of the FRP/concrete interface. The numerical approach is focused on the application of fracture mechanics and the finite element (FE) method for predicting FRP debonding failure. In order to validate the FE model, the numerical predictions are compared to the experimental results obtained from two types of bond tests (i.e., single shear pullout and beam tests). The ultimate failure load, strain distribution, load vs. displacement curve, and failure

mechanism are considered in the comparison. To achieve the general objective of this research, the following more specific objectives are identified:

1. Apply different methods in FE analysis to find the best approach to model and predict IC debonding failure in concrete beams strengthened by FRP plates.

2. Investigate the important factors affecting the behavior of strengthened beams by numerical analysis.

3. Establish the bond-slip behavior experimentally by single shear pullout test and compare it with that calculated using well-accepted methods from available literature.

4. Establish the bond-slip behavior experimentally by beam test and compare it with that obtained from shear pullout test.

5. Experimentally study the sensitivity of the behavior and failure of FRP-strengthened concrete beams to variations in the location of the major flexural/shear crack that triggers the IC debonding failure.

6. Numerically study of the behavior of FRP-strengthened concrete beams by FE analyses.

7. Use Brownian motion and white noise concepts from probability theory to predict the interfacial fracture energy and load carrying capacity variation in FRP bonded concrete specimens.

Many researchers have assumed that the FRP/concrete interface is subjected to a pure Mode II loading (in-plane shear) condition when IC debonding failure occurs. Therefore, they use the single shear pullout test results to predict the IC debonding failure in beams. However, there is no systematic study to validate if the shear test results can be

directly used to predict the debonding failure of FRP-strengthened concrete beams. In this study, the behavior of FRP-strengthened concrete beams is studied experimentally and numerically to verify the application of shear test results in strengthened beam design.

1.3 Outline and Organization of the Dissertation

In this dissertation, experimental and analytical procedures are proposed to predict the debonding failure of concrete elements externally strengthened with bonded FRP composite materials. The objectives conducted during this dissertation are organized in chapters as following:

Chapter 1 presents an introduction to the subject, highlighting current experimental and numerical needs, and the objectives of this study.

Chapter 2 presents a literature review covering experimental, analytical, and numerical methods to obtain the mechanical properties of FRP/concrete joints. The applicability of such methods when predicting the debonding failure of these joints is discussed. Also, key factors affecting the FRP/concrete bond strength are summarized according to different methods in the literature.

Chapter 3 presents the theoretical basis for the application of damage mechanics principles to the study of concrete behavior. Application of a concrete damaged plasticity model in the extended finite element method (XFEM) is proposed for modeling the cracking behavior of concrete in tension.

Chapter 4 introduces different constitutive models for simulating FRP debonding failure in finite element analyses. These methods including cohesive elements, Virtual

Crack Closure Technique (VCCT), cohesive surface, and Extended Finite Element Method (XFEM)-based cohesive method are validated by experimental results obtained by other researchers to determine the most accurate and applicable method to predict IC debonding failure in strengthened concrete beams. Then, the mechanical properties required for using the selected method (XFEM) are discussed.

Chapter 5 presents the experimental method and results of single shear pullout tests to establish the bond-slip behavior. The FE model using the experimentally obtained bond-slip relationship is validated by experimental results, and is then used to study the stress state of the FRP/concrete interface and the sensitivity of single shear test results to changes in boundary conditions.

Chapter 6 presents, firstly, the experimental results from beam tests conducted to investigate the behaviour and bond-slip relationship of concrete beams strengthened externally by FRP plates. The beams are notched at different locations to study the sensitivity of the strengthened beams to the location of a major flexural/shear crack. Secondly, numerical model validated by experimental results is applied to find the stress state of the FRP/concrete interface in beams. This stress state is compared with the one obtained in the shear tests to verify the application of the bond-slip relationship obtained using the shear test in the analysis of strengthened beams.

Chapter 7 presents the prediction of interfacial fracture energy variation in FRP bonded concrete specimens using Brownian motion and white noise concepts adapted from probability theory. In an effort to effectively model the effects of the variation of interfacial fracture energy on the load versus deflection responses of FRP bonded concrete specimens subjected to Mode I and Mode II loading, a random white noise using

a one-dimensional standard Brownian motion is added to the governing equations,

yielding a stochastic differential equation. By solving this stochastic equation, the bounds

of load carrying capacity variation with 95% probability are found for different

experimental tests.

Chapter 8 presents the conclusions of this research and recommendations for

future research work.

Chapter 2 Literature Review

In the case of concrete flexural members strengthened with FRP composite materials, the behavior of FRP/concrete interface, hereafter called the bond-slip behavior, often governs the structural performance of elements being repaired. In the present study, experimental and numerical procedures are proposed to find the bond-slip behavior of strengthened concrete beams in order to predict the debonding behavior at the tip of a flexural/shear crack.

Generally there are two types of test procedures used to find the bond-slip behavior reported in the literature: shear pullout tests, and beam tests. Often, empirical and analytical equations are developed by using the test results from these two experimental methods. Numerical analyses using finite element techniques are also validated by these test results.

In this chapter, for the sake of clarity, the studies and analyses of shear tests and beam tests are described separately. The FRP/concrete interface at the tip of a major flexural/shear crack is subjected to mixed-mode loading conditions including in-plane shear and normal stresses. Therefore, the researches that have been performed to study the fracture of the FRP/concrete interface under mixed-mode loading conditions are also reviewed. The principal findings from the literature review of the FRP debonding from the concrete substrate are summarized at the end of this chapter.

2.1 Shear Pullout Tests

In a double (Fig. 1.2a) or single (Fig 1.2b) pullout test, the in-plane shear stress is applied to the FRP/concrete interface by applying uniaxial tension in the plane of the FRP typically along the direction of principal (longitudinal) fiber orientation. Normally, the bond-slip relation obtained from the pullout tests is used for nonlinear fracture mechanics or cohesive crack models in numerical analyses to predict FRP debonding failure from the concrete substrate.

The bond-slip relationships from experimental tests are commonly derived in one of two ways: (a) from direct measurement of FRP axial strains (that is called conventional method after here), or (b) from indirect analytical solutions modified by test results.

In the former method many strain gauges are attached with small intervals along the FRP surface as shown in Figure 2.1. The bond stress and slip are then obtained from the following equations:

$$\tau_i = \frac{t_f E_f}{\Delta x}(\varepsilon_i - \varepsilon_{i-1}) \tag{2.1}$$

$$\delta_i = \frac{\Delta x}{2}(\varepsilon_0 + 2\sum_{j=1}^{i-1}\varepsilon_j + \varepsilon_i) \tag{2.2}$$

where τ_i is the average interfacial bond stress in the increment i having length Δx, ε_i and ε_{i-1} are the measured strain values of ith and $(i-1)^{\text{th}}$ gauges arranged along the FRP sheet, E_f and t_f are the elastic modulus and thickness of the FRP plate/sheet, respectively, δ_i is the local slip between the FRP sheet and concrete at the section i, ε_0 is the strain in the FRP sheet at the free end of bonded area, and ε_j is the strain value of the jth gauge.

It has been concluded from available literature that the conventional method

cannot produce accurate bond-slip curves and large irregular differences are observed among curves along the bonded length (e.g., Dai et al. 2005, Lu et al. 2007, Baky et al. 2012).
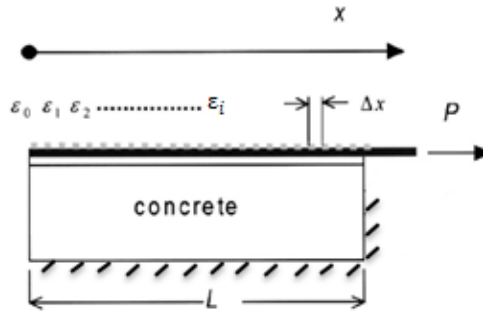
Figure 2.1 Shear pullout test (Dai et al. 2005)

For example, Figure 2.2 presents the local bond stress-slip relationships at different locations from loaded end in a pullout test reported by Dai et al. (2005). The large scatter of the bond-slip behavior may be due to the discrete nature of concrete cracks, random distribution of concrete aggregates, different concrete volumes attached to the FRP after initial damage affecting the stiffness of the debonding element, and/or local bending of FRP laminates. Therefore, many researches have been conducted to achieve more accurate bond-slip behavior from pullout tests.
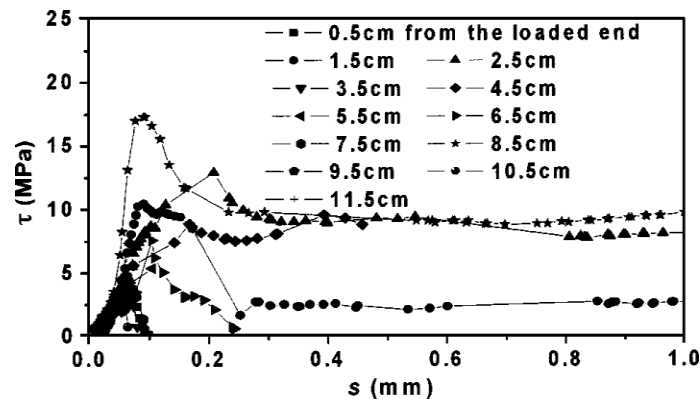
Figure 2.2 Local bond stress-slip relationships at different locations from loaded end (Dai et al. 2005)

A more stable analytical method in determining the bond-slip behavior of the FRP/concrete interfaces through single pullout bond tests, without the necessity of recording the strain distribution of the FRP sheet, is proposed by Dai et al. (2005). By this method, the local interfacial bond stress-slip model can be obtained from the relationship between the pullout force and the loaded end slip. Only two parameters, the interfacial fracture energy and the interfacial ductility index, which take into account the effects of all interfacial components, are necessary in this model. The proposed equations account for the effect of adhesive properties by considering the adhesive shear modulus (G_a) and thickness (t_a) as follows:

$$\tau_{max} = 0.5BG_f \tag{2.3a}$$

$$G_f = 0.466 \left(\frac{G_a}{t_a}\right)^{-0.352} f_c'^{0.236}(E_f t_f)^{0.023} \tag{2.3b}$$

$$B = 6.846(E_f t_f)^{0.108} \left(\frac{G_a}{t_a}\right)^{0.833} \tag{2.3c}$$

where τ_{max} (*MPa*) is the maximum shear stress (bond strength), G_f (*N/mm*) is the interfacial fracture energy, G_a (*GPa*) is the shear modulus of adhesive, t_a and t_f (*mm*) are the thicknesses of adhesive and FRP plate, respectively, f_c' (*MPa*) is the compressive strength of concrete, and E_f (*MPa*) is the Young's modulus of FRP.

Since it is difficult to obtain accurate bond-slip curves from experimental tests, Lu et al. (2005) proposed three analytical models for the bond-slip relationship based on finite element analysis results. This numerical modeling approach relies on the accurate modeling of concrete failure close to the adhesive. To properly simulate the failure in the concrete close to the interface, a meso-scale finite element approach was used in conjunction with a fixed angle model. Debonding was simulated as the fracture of

concrete elements. From the meso-scale finite element results, a bond-slip relation was

obtained with numerical smoothing calibrated by test results. This model is accurate, but

it is too complicated for practical application. Therefore, a simplified model without a

significant loss of accuracy was proposed in the same study. In addition, further

simplification has been made to obtain a bilinear bond-slip curve which can be used to

derive a simple explicit design equation for bond strength. The comparison among the

three proposed models is shown in Figure 2.3. The bilinear version of the proposed model

taking into account the FRP width effect is:

$$\tau_{max} = 1.5\beta_w f_t \tag{2.4a}$$

$$G_f = 0.308\,\beta_w{}^2\sqrt{f_t} \tag{2.4b}$$

$$\beta_w = \sqrt{\frac{2.25 - b_f/b_c}{1.25 + b_f/b_c}} \tag{2.4c}$$

where b_f and b_c are the FRP plate and concrete block widths, respectively, and f_t is the

tensile strength of concrete.
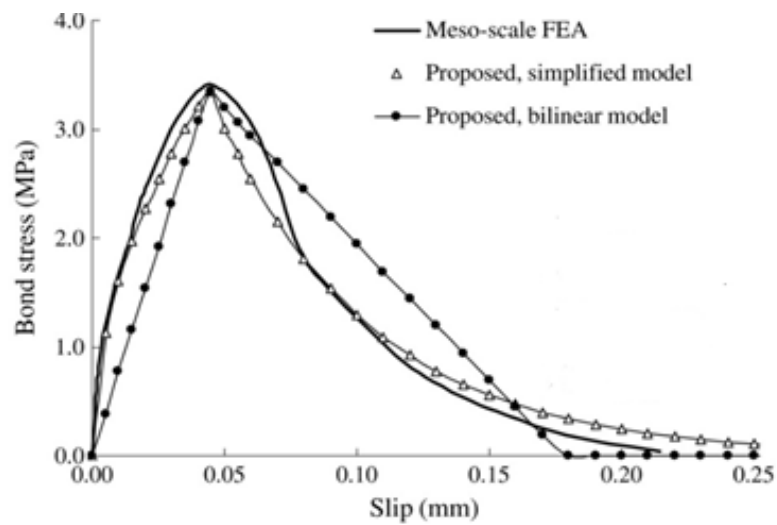
Figure 2.3 Bond–slip curves from meso-scale finite element simulation and proposed bond–slip models by Lu et al. (2005)

Equations 2.3a to c, which are derived from experiments, and Equations 2.4a to c, which are derived from numerical analyses, are popular models of the bond-slip behavior that have served to validate other methods in the literature (e.g., Baky et al. 2012, Toutanji et al. 2013) . The former consider the adhesive contribution and the latter consider the FRP width contribution to the bond strength and the interfacial fracture energy. They are used in Chapters 4 and 5 to determine the bond strength and the interfacial fracture energy of the FRP/concrete interface in shear pullout specimens.

Lu et al. (2005) assessed the existing models (up to 2005) and found that the bilinear bond-slip model can be a good approximation for the shape of bond-slip curves. It is also confirmed in other studies (e.g., Liu et al. 2007, Yuan et al. 2012, Serbescu et al. 2013). A correct estimate of the elastic stiffness branch of the bond-slip relationship requires the compliances of both adhesive and a thin layer of attached concrete be taken into account (e.g., Ferracuti et al. 2007, Toutanji et al. 2012, Baky et al. 2012).

Some studies have implemented expression proposed by Popovics (1973) for the constitutive law of concrete as bond-slip behavior of the FRP/concrete interface in shear pullout tests (e.g., Karbhari et al. 2006, Ferracuti et al. 2007, Toutanji et al. 2013) that is given as:

$$\tau = \tau_{max}\left(\frac{s}{s_0}\right)\frac{n}{(n-1)+\left(\frac{s}{s_0}\right)^n} \tag{2.5}$$

where s_0 is the slip when the maximum shear stress is achieved, and n is a parameter mainly governing the softening branch of the bond-slip. The interface law proposed by Ferracuti et al. (2007), based on the application of Popovics's law, is depicted in Figure 2.4 in non-dimensional form for different values of parameter n. The experimental FRP strains were used to calibrate the proposed bond-slip behavior for finding an appropriate

value of n.
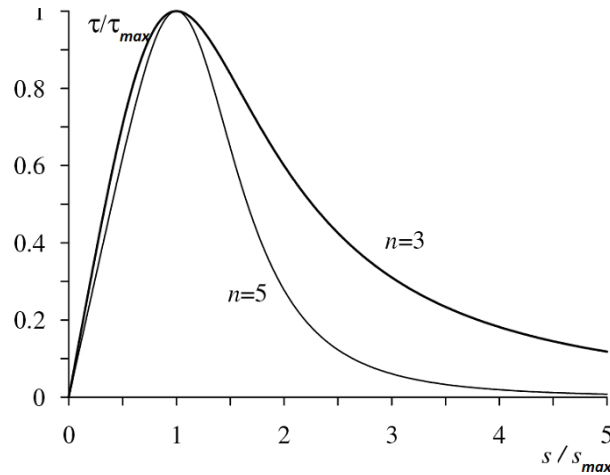
Figure 2.4 Proposed interface law by Ferracuti et al. (2007) for different values of parameter n

Based on the experimental pullout tests, it was found that the debonding failure occurs at a certain depth in the concrete substrate from the FRP/concrete interface; typically 1-5 mm (Bank 2006). Therefore, the bond strength may be expressed as a function of the concrete strength. Toutanji et al. (2013) proposed a failure criterion where the maximum principal stress on a small element in the concrete substrate, σ_e, shown in Figure 2.5, is limited to the tensile strength of concrete, f_t; therefore simply setting $\sigma_e = f_t$ can predict the debonding initiation between FRP composites and reinforced concrete beams. The interfacial fracture energy, the maximum shear stress, and corresponding local slip are required as intermediate parameters to determine the maximum transferable load. The maximum interfacial shear stress and the corresponding local slip were approximated by developing an analytical solution considering the effect of the adhesive thickness besides to the concrete. The predicted maximum applied load from the numerical solution was in good agreement with single and double plies of FRP

from experimental data conducted by Dai et al. (2005). For three plies, however, variation

of 20–30% was observed which Toutanji et al. attribute to experimental uncertainties.

More FRP plies require thicker FRP to be pinched and pulled by the testing machine

resulting in greater kinking of the FRP plate.
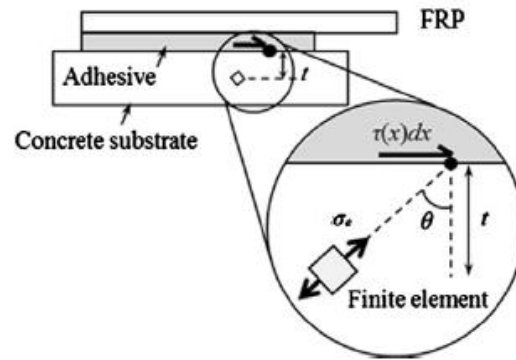
**Figure 2.5 Maximum principal stress in the concrete substrate element in pullout
test proposed by Toutanji et al. (2013)**

Baky et al. (2012) developed a 3D nonlinear micromechanics-based finite element

model using the micro-plane theory for concrete. In their formulation, the micro-plane

constitutive law was implemented as a user-defined subroutine in the ADINA finite

element package to run the simulations. The numerical results showed that stress

distribution has the same trend along the interface in the first few millimeters inside the

concrete adjacent to the adhesive/concrete interface. Also, it was confirmed that

FRP/concrete joints subjected to shear loading do not represent the case of pure shear

stress, and there are normal stress components along the interface that have a significant

effect on the local bond strength (this is analogous to the concept of shear friction).

Therefore, a failure criterion for the interface defining the relationship between the

maximum shear stress and the state of stress along bonded length was first defined before

deriving the bond-slip law. Like the study of Toutanji et al. (2013), it was assumed that when the maximum principal stress reaches the concrete tensile strength, the corresponding shear stress is equal to the maximum shear stress. Then a new mathematical approach was proposed by them (Baky et al. 2012) to describe the entire local bond–slip relationship. Their proposed interface law accounts for the nonlinear contributions of the FRP laminates, adhesive and concrete layers.

As mentioned above, Baky et al. (2012) and Toutanji et al. (2013) proposed their models based on this assumption that the bond strength of the interface is a function of concrete tensile strength. This assumption is used in Chapters 5 and 6 to investigate the stress state of the FRP/concrete interface.

Benvenuti et al. (2012) presented an analysis focusing on the finite element modeling of debonding tests in FRP-reinforced concrete blocks using the extended finite element model (XFEM) approach for the first time. It takes into consideration the mechanical properties of concrete, adhesive and FRP. Both FRP and adhesive layers were considered as linear elastic materials, while the constitutive behavior of the concrete was governed by an elasto-damaging constitutive law. In XFEM, as soon as a critical damage threshold is reached in the concrete, additional degrees of freedom, representative of the displacement discontinuity corresponding to the debonding process, are added.

2.2 Beam Tests

As is evident from the previous discussion, the stress state in concrete close to the FRP/concrete interface plays an important role in the bond-slip behavior and in the overall debonding failure process. Since the loading type, boundary conditions, and

deflections are different in FRP-strengthened beams from those of the FRP/concrete joint under shear force in pullout tests, the stress state of the concrete along the FRP/concrete interface in beams may not be the same as that in the pullout specimens. Because of this, the use of pullout test results to predict the behavior of FRP-strengthened concrete beams may not represent the actual debonding phenomenon. Therefore, some researches were conducted to study the IC debonding behavior in FRP-strengthened concrete beams. Lu et al. (2007) used the meso-scale finite-element method to determine whether the bond-slip behavior of the interface in a FRP-strengthened beam can be predicted by a bond-slip model derived from pullout tests. They concluded that the proposed model based on pullout tests can be used for the bonded region outside of the cracked constant moment region of a test beam. For the cracked constant moment region, a model with a more brittle descending branch was proposed. It is worth to mention that in real structures, there is rarely a constant moment region.

The assumption of bilinear equation for the bond-slip behavior works for FRP-strengthened beams, too. Faella et al. (2008) formulated a numerical model for simulating the flexural behavior of FRP-strengthened RC beams considering bilinear stress–slip relationships. The characteristics of this bilinear equation were determined according to the fib-CEB-FIP bulletin 14- approach 2 (2001). It is proved that end debonding failure depends only on the value of fracture energy and not on the shape of the interface law; on the contrary, IC debonding failure is controlled by the bond strength.

Rabinovitch (2008) compared the application of a linear elastic fracture mechanics (LEFM) approach and a cohesive interface (cohesive zone) modeling approach in the debonding analyses of concrete beams strengthened with externally

bonded FRP strips. He believes that the main advantages of the cohesive interface

approach is its ability to predict the initiation and progress of the debonding process and

to describe the complete spectrum of the response ranging from full bonding to complete

separation; its major disadvantage is the computational effort and resources required for

the numerical solution of the governing equations compared to the LEFM method. He

reported the results of the two models were in good agreement. Thus, in cases where

quantitative information regarding the initiation and progress of the debonding process is

available, the LEFM model can be used for a reasonable quantitative appraisal of the

debonding mechanism. Its relative simplicity and the saving in computational effort

contribute to its attractiveness. However, the LEFM model predicts lower critical values

of the peak loads in some cases. In the cases that a reliable description of the debonding

process is not available, and in the cases that the quantitative evaluation of the entire

spectrum of unstable branches is of interest, the cohesive interface model overcomes the

restrictions of the LEFM approach and provides a more comprehensive description.

Gunes et al. (2009) developed an analytical prediction of interfacial fracture

energy in FRP-strengthened RC beams. It was shown that all debonding at the

FRP/concrete interface takes place sufficiently close to mode II conditions and mode II

fracture energy of concrete is at least an order of magnitude higher than mode I fracture

energy. It is concluded that the proposed model performs better than ACI 440.2R (2008)

equations for estimating the debonding load.

Harries et al. (2010) conducted experimental research in support of the

development of a standard test method for assessing FRP-to-concrete bond. A simple

concrete beam specimen similar to that used to determine the modulus of rupture of

concrete was used during the tests. To achieve controlled debonding behavior, the beam was notched to represent cracked concrete. This study addresses specific issues associated with standardizing such a test specimen including: a) the width of the FRP relative to the concrete substrate width; b) the geometry of the induced notch; and c) the effect of providing an initially un-bonded region in the vicinity of the notch. The authors recommend having a 51 *mm* wide FRP strip on a 152 *mm* square concrete section and a saw-cut notch 19 *mm* deep without consideration of un-bonded region. Harries et al. (2012) adjusted the specimen geometry so that the notch is one half of the specimen depth (76 *mm* in a 152 *mm* specimen and 51 *mm* in 102 *mm* prisms). They also proposed a set of simplified and rigorous equations based on fundamental mechanics and specimen geometry to predict the average bond stress over the entire bonded area to one side of the notch. These equations were intended for use in cases where strain measurement is impractical, such as in tests involving harsh environmental exposure. This method is presently being developed by ASTM Committee D30.10 as a standard test method. The experimental data from this study is used to validate the applied numerical analysis of FRP-strengthened beams in Chapter 4.

FE analyses are also used to predict IC debonding failure. For instance, Obaidat et al. (2010) presented a finite element analysis which was validated by laboratory tests of eight beams under four point bending loading. The commercial numerical analysis tool ABAQUS was used and different material models were evaluated with respect to their ability to describe the behavior of the beams. A perfect bond model and a cohesive bond model were assumed for the concrete–CFRP interface. A plastic damage model was applied for the concrete. The numerical results indicated that the equation proposed by Lu

et al. (2005) for maximum shear stress results in too high a value. Obaidat et al. used half of this value in the subsequent analyses. The analytical results showed good agreement with experimental data in terms of the load–displacement response, crack pattern and debonding failure mode when the cohesive bond model was used. The perfect bond model failed to capture the softening behavior of the beams.

Chang et al. (2012) presented a numerical study of single flexural crack induced debonding based on a progressive damage model. In practice, the adhesive layer is never a homogeneous medium because it contains heterogeneities, such as imperfection of FRP concrete bond, bubbles or voids at various length-scales, varying adhesive thicknesses along bond length, etc. So, they considered these local-scale heterogeneities in numerical modeling. To achieve this, the adhesive layer between the concrete and the FRP plate was assumed to be composed of many elements of the same size. The mechanical properties of these elements were assumed to conform to a Weibull distribution. The numerical results indicate that although local debonding nucleates at random heterogeneities, the dominant debonding 'event' initiates from the pre-existing crack and propagates to the FRP plate ends as the applied load increases.

2.3 Mixed-Mode Loading Condition

There is another group of researches on the IC debonding failure in FRP-strengthened concrete beams following the idea that the FRP/concrete at the tip of flexural/shear crack is subjected to mixed-mode loading. For a crack occurring in the shear span (i.e., non-zero shear-to-moment ratio), the relative vertical displacement prior to a critical diagonal crack forming between the two faces of the crack produces peeling

stresses (mode I) at the interface in addition to the shear stress (mode II) due to flexural loading on the beam as shown in Figure 2.6.
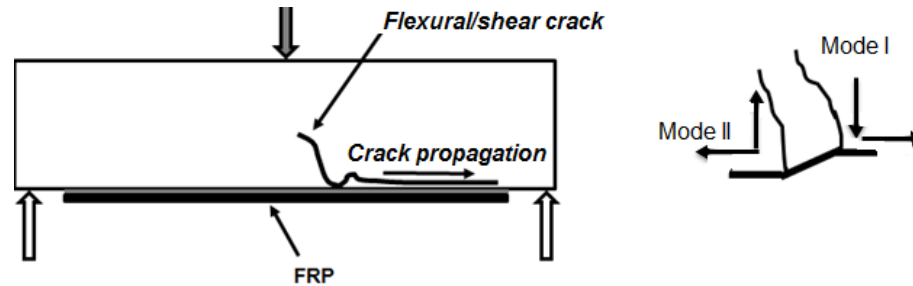
Figure 2.6 Typical Mixed-mode intermediate crack (IC) debonding failure

Karbhari and Engineer (1996) developed a special test setup to introduce different interfacial peeling angles between thin flexible FRP sheet and a concrete substrate. The theoretical equations were derived for this test setup to separate mode I and mode II components of the interfacial fracture energy, and therefore establish a quantitative comparison of interfacial adhesion mechanisms and energies of FRP to concrete interface bond under mixed-mode loading conditions. It was found that there is a linear relationship between the critical mode I and mode II strain energy release rates when the FRP to concrete interface is subjected to a mixed-mode loading condition as shown in Figure 2.7. The test setup used by Karbhari and Engineer (1996) was limited in so far as the bonded FRP must be very flexible; therefore, the method is not appropriate for FRP materials more typical of structural applications.
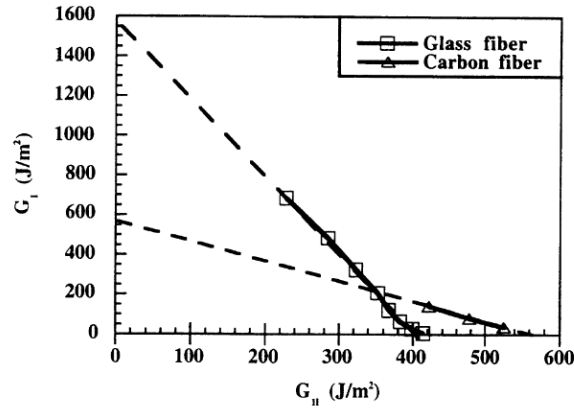
Figure 2.7 G_I vs. G_{II} for the material used by Karbhari and Engineer (1996)

Wan et al. (2004) used introduced modified double cantilever beam (MDCB) specimens and a customized test frame to introduce different loading angles in order to evaluate the bond characteristics and toughness of FRP bonded to concrete under mixed-mode loading. This method overcame some of the limitations of the technique proposed by Karbhari and Engineer (1996). It was shown, for materials more suited to civil infrastructure repair, that the FRP debonding from the concrete substrate is predominantly controlled by mode I deformation with a small portion of mode II deformation at the crack tip for loading angles between 0° and 60°. The experimental data from this study is used to validate the applied numerical analysis of the FRP/concrete interface behavior under mixed-mode loading in Chapter 4.

Niu et al. (2006) investigated mechanisms associated with diagonal cracks and modeled debonding initiation and propagation through a fracture mechanics based finite element approach. It was seen that debonding propagation is mainly caused by mode II fracture mechanisms and that the interfacial failure path is primarily governed by the relationships between concrete cracking behavior and interfacial properties. In this study, a bilinear elastic softening model was used to model the interface stress-slip behaviors in

both the shear (mode II) and normal (mode I) directions. No coupling effect between mode I and II stress-slip laws was considered. Since it is proved in some studies (e.g., Karbhari and Engineer 1996, Dai et al. 2009) that there is some relationship between mode I and II fracture energies, the assumption of "no coupling effect" appears to be an oversight in this work.

Pan and Leung (2007) developed a specimen including a concrete block and a metal fixture, which were externally bonded with the same FRP sheets and were jointed with a steel hinge presented in Figure 2.8. Different relative vertical displacements between the concrete and steel parts were introduced to create combined pulling and peeling forces on the FRP to concrete interface. It was observed when a vertical displacement was applied to introduce peeling, the load for debonding to initiate decreased. However, for the ultimate load, the effect of peeling appeared to depend on the length of the FRP plate. For the relatively short FRP (150 mm in length), the peeling effect corresponding to 8 mm vertical displacement can reduce the ultimate debonding load by over 40%. For the longer FRP (450 mm in length), the same peeling effect may only reduce the ultimate load by about 10–25%. A new theoretical model for debonding analysis under such a situation was developed. In the model, the interfacial behavior was described by four parameters, with one of them, the interfacial shear strength, affected by the maximum interfacial normal stress.
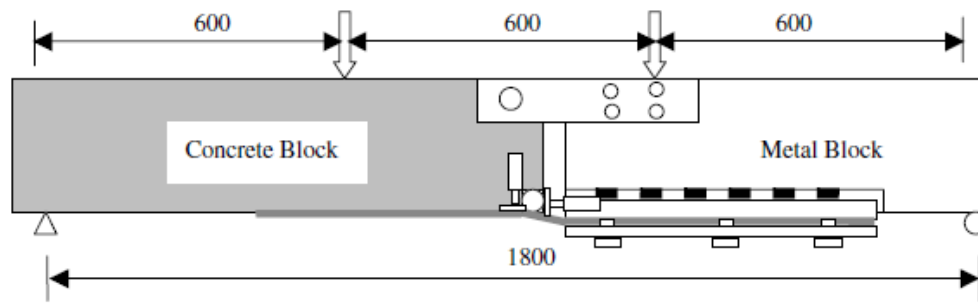
Figure 2.8 Set up for mixed-mode debonding test used by Pan and Leung (2007)

Dai et al. (2009) proposed an experimental method to evaluate the fracture

properties of the FRP/concrete interface under coupled shear (mode II) and peeling

(mode I) loading conditions. An analytical model was developed to evaluate the mode I

and mode II strain energy release rates and the corresponding fracture mechanisms of the

FRP to concrete interface under a pure bending action, a pure dowel action, and the

coupled action of both. A linear failure envelope is proposed to describe the fracture

properties of the CFRP to concrete interface under the coupled action. The experimental

data from this study is used to validate the applied numerical analysis of the

FRP/concrete interface behavior under mixed-mode loading in Chapter 4.

2.4 Principal Findings from Literature Review

The principal findings, observations, and results from literature review of FRP

debonding from concrete substrate are summarized as follows:

1. There is a significant scatter in bond-slip behaviors along the FRP/concrete

    interface gained from direct measurement of FRP axial strains (conventional

    method) in shear pullout tests.

2. Currently, there are different proposed bond-slip models obtained from

experiments, analytical methods, and numerical analysis. They represent a range of approaches and perspectives and consider different material properties. Therefore, they may give different results. Some of the well-known models are going to be used in this study in Chapter 5 for the comparison with conducted experimental results.

3. The debonding crack occurs in concrete at a few (1-5) millimeters from the FRP/concrete interface.

4. Since the FRP debonding occurs in the concrete side, the bond strength may be considered as the function of the concrete strength.

5. Generally, the concrete strength (f_c'), FRP tension stiffness ($E_f t_f$), adhesive shear stiffness ($\frac{G_a}{t_a}$), and FRP plate width to concrete width ratio (b_f / b_c) are significant parameters affecting the local bond-slip behavior of FRP/concrete interface subjected to in-plane shear stress in shear pullout tests.

6. The bilinear bond-slip curve assumption does not decrease the accuracy of the proposed models to predict the failure load relative to the nonlinear bond-slip curves.

7. In developing an analytical bond-slip curve, the shear stiffness of both the adhesive layer and a very thin layer of concrete attached to the debonded FRP should be considered.

8. Debonding failure in FRP-strengthened concrete beams is likely to occur due to the development of high interfacial stresses at locations of flexure/shear cracks in concrete. Although the region is usually modeled as an FRP/concrete joint under tensile loading, the real loading condition is more complex

involving components of tension, shear and bending loads acting together. Thus the use of simple shear pullout tests for the determination of bond strength is a gross simplification. There is no systematic study to validate if the shear test results can be directly used to predict the debonding failure of FRP-strengthened concrete beams.

9. There is currently no commonly accepted experimental or analytical approach to define the bond-slip curve to predict IC debonding failure in FRP-strengthened beams.

10. Typical flexural/shear cracks in the concrete substrate lead to a mixed-mode debonding mode. To date, the mixed-mode debonding is studied by different specialized experimental setups and there is no common agreed method.

11. There is a relationship between mode I and mode II interfacial fracture energies in mixed-mode loading condition. The increasing of interfacial mode I fracture energy results in the decreasing of mode II fracture energy.

The principal findings, mentioned above, are used in numerical and experimental parts of the present study in the next chapters to investigate IC debonding failure and mixed-mode behavior in FRP-strengthened concrete beams. The bond-slip behaviors in beam and shear specimens are also compared to verify the application of shear pullout test results in strengthened beams to predict IC debonding failure.

Chapter 3 Concrete Modeling in Finite Element Method Using Fracture Mechanics

Concrete is a material comprised of a mixture of cement and fine (sand) and coarse (gravel) stone or other aggregate. When mixed with water, hydration of the cement occurs, forming a matrix which binds the aggregate into a composite solid. Concrete has a high compressive strength but a relatively weak and brittle tensile behavior.

Fracture mechanics is the study of the response and failure of structures as a consequence of crack initiation and propagation. One of the outstanding advantages of fracture mechanics is that stiffness and size effects are naturally included in the analysis.

Without additional tensile reinforcement, cracking of concrete represents a catastrophic failure. When reinforced, cracking occurs but may be controlled and distributed within the structural member. This fact points the research community to apply fracture mechanics for concrete cracking modeling.

The conventional finite element method (FEM) is well-known as a reliable numerical technique for studying the behavior of an extensive range of engineering and physical problems. For problems comprising a continuous or homogenous media without discontinuities, the FEM is a well-suited as a method of analysis. However, for problems having non-smooth and non-regular solution characteristics, the extended finite element model (XFEM) technique is more appropriate.

In this chapter, the application of fracture mechanics in the FEM to model the cracking behavior of concrete is first explained. Then, the XFEM and its formulations are presented. Finally, the combination of XFEM-based cohesive method and concrete damaged plasticity model to simulate the cracking of concrete is proposed.

3.1 Application of Fracture Mechanics in Concrete Behavior Modeling

Fracture mechanics was originally developed for the analysis of brittle materials where flaws in the material initiated the propagation of a single crack (Shah and McGarry 1971). Such materials are classified as brittle and show linear tension stress-stain behavior and the stress suddenly drops to zero when a brittle material fractures.

Almost all engineering materials contain unavoidable defects. Conventional strength-based design methods consider the effect of these defects through consideration of a stress concentration factor, K_t. For example, for an infinite plate subject to a uniaxial stress field, σ_N, with a small elliptical hole through its thickness as shown in Figure 3.1, the maximum stress along the edge of the hole, σ_{max}, is K_t times greater than the free field stress, σ_N. From an elastic stress analysis, the relationship between σ_{max} and σ_N is (Shah et al. 1995):

$$\sigma_{max} = K_t \sigma_N = \left(1 + \frac{2a_1}{a_2}\right)\sigma_N \tag{3.1}$$

where a_1 and a_2 are the long and short radii of the hole, respectively.
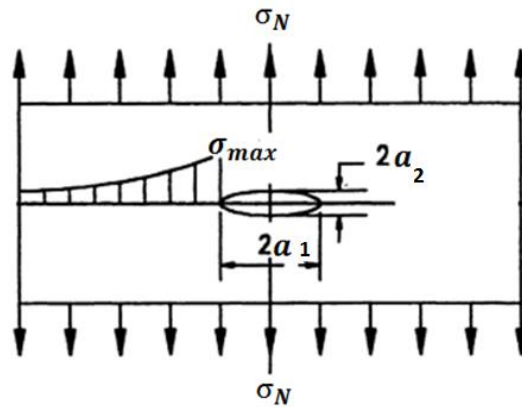
**Figure 3.1 Distribution of internal stress in region of an elliptical hole
(shah et al. 1995)**

Factor K_t theoretically approaches infinity for a very narrow hole or a sharp crack (i.e., as a_2 approaches 0). Therefore, the conventional analysis method is not valid for a sharp crack. The point $\sigma_{max} \to \infty$ as $a_2/a_1 \to 0$ is the basic idea of linear elastic fracture mechanics (LEFM). According to the LEFM, the nominal stress, σ_N, in the plate in Figure 3.1 when $a_2 = 0$ can be expressed as:

$$\sigma_N = \frac{K_I}{\sqrt{\pi a_1}} \tag{3.2}$$

where a_1 is half of the crack length, and K_I is the stress intensity factor. The value of K_I accounts for the singularity at the crack tip and depends on load, geometry, boundary conditions, and crack size. It can serve as a fracture criterion. A crack grows when:

$$K_I \geq K_{Ic} \tag{3.3}$$

where K_{Ic} is the critical stress intensity factor which is a property of the material based on LEFM. Both K_I and K_{Ic} may be determined experimentally applying Equations 3.2 and 3.3.

The value of stress theoretically approaches infinity at the tip of a crack due to the singularity. Because no material can withstand infinite stress, a certain size of inelastic zone (fracture process zone or FPZ) forms at the crack tip for a real material. If this inelastic zone is small compared to the fracture dimensions in a structure, LEFM is an appropriate 'approximate' method of analysis. Otherwise, energy dissipated in the FPZ must be considered. The FPZ uses part of the energy provided by the applied load and causes nonlinearity in the response of the structure. Since concrete is not completely brittle and is classified as quasi-brittle material, the application of LEFM in concrete fracture analysis is limited to large structures such as dams.

3.1.1 Fracture Process and Strain Localization of Concrete

Concrete is weak in tension, having tensile strength that ranges from 8 to 15% of its compressive strength. For this reason, the fracture of concrete members is controlled by concrete cracking due to tensile stress. The cracks in a concrete member propagate in the direction perpendicular to the direction of principal tensile stresses but are also affected locally by the composition of the concrete composite material. The mechanical behavior of concrete subjected to different loading conditions is governed by the initiation and propagation of these cracks. This point leads the researchers to apply fracture mechanics for concrete damage analysis.

The typical stress-displacement curve of a concrete under uniaxial tension can be divided into four stages based on initiation and propagation of cracks (Shah et al. 1995) as shown in Figure 3.2. The first stage, from the origin to point A, is essentially an un-cracked linear behavior in which the initiation of internal cracks is negligible. During the second stage, from points A to B (at about 80% of maximum tensile capacity) internal cracks initiate and propagate. In the third stage, from points B to C, the internal cracks start to localize into a major crack. The major crack propagates with increasing load up to the peak load-carrying capacity in this stage. This phenomenon is called strain localization. The fourth, post-peak stage is after maximum load; in this the major crack propagation is unstable and continues with load decreasing. Generally, the concrete behaves as a nonlinear quasi-brittle material in tension. The behavior of concrete under uniaxial compression has the similar trend.
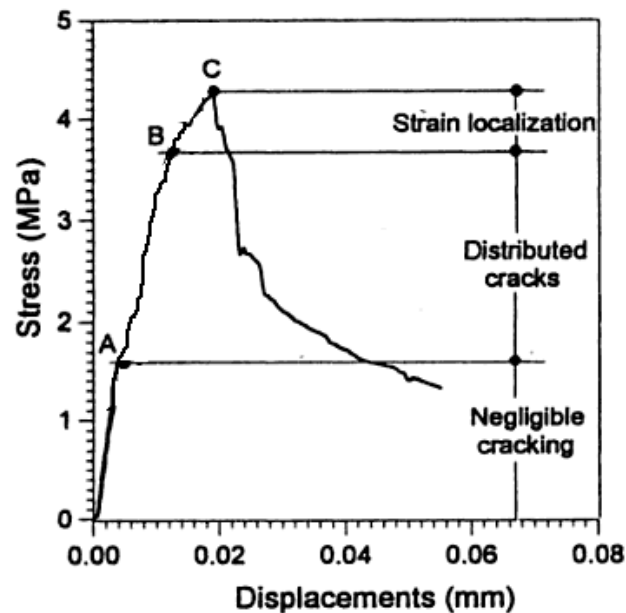
Figure 3.2 Stress-stain behavior of concrete subjected to uniaxial tension stress (Shah et al. 1995)

3.1.2 Fictitious Crack Model

As mentioned before, because of the stress concentration at the tip of a crack, the FPZ forms around the crack tip. When the crack propagates in concrete, new crack surfaces are formed that may be in contact and are tortuous in nature. This causes toughening mechanisms in the FPZ such as aggregate bridging. Since new crack surfaces are in contact, they may continue to resist some tensile stress that is described by the softening branch (Point C to failure in Figure 3.2) of the stress-displacement relationship. The fracture behavior of concrete is significantly influenced by the FPZ. Since LEFM does not consider the FPZ, it cannot result in accurate analysis of concrete fracture. Hillerborg et al. (1976) proposed a fictitious crack model for concrete fracture modeling. In this model, the toughening mechanisms in the FPZ are simulated by a cohesive

pressure, σ_w, on the crack surfaces as shown in Figure 3.3. This cohesive pressure has a tendency to close the crack and is a function of the crack opening displacement, w.
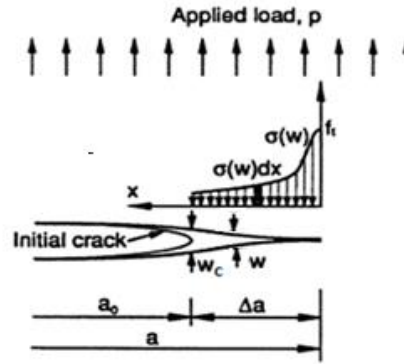
Figure 3.3 Modeling of FPZ by cohesive pressure (Shah et al. 1995)

Using the fictitious crack model, the post-fracture behavior or softening of concrete can be defined by a stress-displacement curve as shown in Figure 3.4. The area under this curve is denoted as fracture energy, G_F, that is given by:

$$G_F = \int_0^{w_c} \sigma_w \, dw \tag{3.4}$$

where w_c is the critical crack opening displacement when the softening stress is equal to zero. The fracture energy, G_F, presents the energy absorbed per unit area of concrete and is considered a material property if the concrete. The fictitious crack model is the basis for the concrete cracking model in this dissertation.
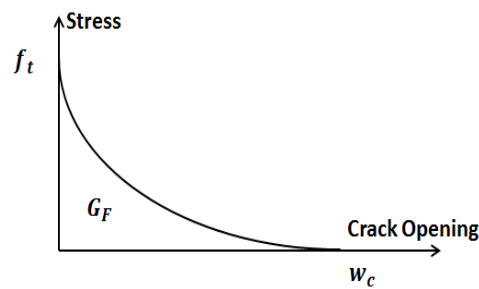
Figure 3.4 Softening curve of concrete in fictitious crack model

3.1.3 Concrete Damaged Plasticity Model

Concrete damaged plasticity model is a continuum, plasticity-based damage model which simulates the constitutive behavior of concrete. It assumes that the two main failure mechanisms of concrete are cracking in tension and crushing in compression (Lubliner et al. 1989, Lee and Fenves 1998). This model can describe the nonlinear behavior of concrete including failures in both tension and compression. The evolution of the yield (or failure) surface is controlled by two hardening variables, $\tilde{\varepsilon}_t^{pl}$ and $\tilde{\varepsilon}_c^{pl}$, linked to the failure mechanisms, which are referred to as equivalent plastic strains in tension and compression, respectively. Key aspects of the concrete damaged plasticity model provided in the finite element code ABAQUS (version 6.13) are presented in following sections.

3.1.3.1 Tensile Behavior of Concrete Modeling

The response of concrete under uniaxial tension is assumed linear up to the tensile strength, f_t, as shown in Figure 3.5. For strain softening behavior specification, the post-failure stress is considered as a function of cracking strain, $\tilde{\varepsilon}_t^{ck}$. The cracking strain is defined as the total strain minus the elastic strain corresponding to the undamaged material; that is, $\tilde{\varepsilon}_t^{ck} = \varepsilon_t - \varepsilon_t^{el}$, where $\varepsilon_t^{el} = \frac{\sigma_t}{E_0}$, as illustrated in Figure 3.5.

By assuming no stiffness degradation after the peak stress (as done in this dissertation), the model behaves as a plasticity model; consequently, the equivalent plastic strain is equal to the cracking strain, $\tilde{\varepsilon}_t^{pl} = \tilde{\varepsilon}_t^{ck}$. The stress-strain relationship in tension may be expressed as:

$$\sigma_t = E_0(\varepsilon_t - \tilde{\varepsilon}_t^{pl}) = E_0(\varepsilon_t - \tilde{\varepsilon}_t^{ck}) \tag{3.5}$$
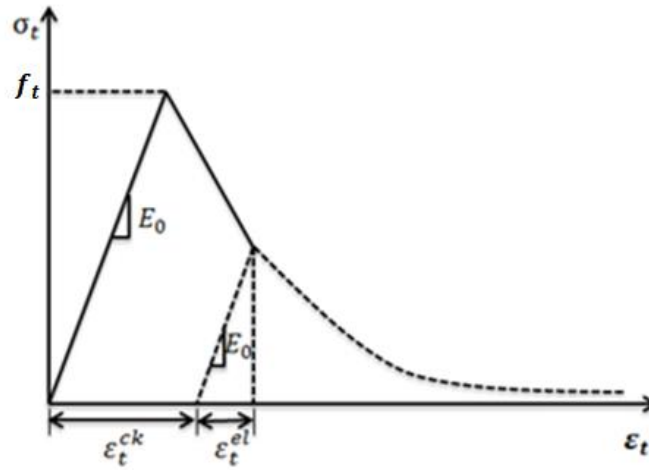
Figure 3.5 Tension stress-strain behavior in concrete damaged plasticity model (Abaqus/standard User's Manual 2013)

Continuum theories, such as damaged-plasticity, use the formulation of their constitutive equations in stress-strain relation forms as shown in Equation 3.5. However, this approach causes mesh sensitivity in the finite element analysis of quasi-brittle materials such as concrete, in the sense that the finite element analysis does not converge to a unique solution as the mesh is refined because mesh refinement leads to narrower crack bands. The mesh sensitivity is due to strain localization behavior as described before. In addition, the damaged plasticity model needs to re-scale the stress-strain curve in terms of plastic strain.

The fictitious model proposed by Hillerborg et al. (1976) may be used for dealing with these two issues. This model defines the energy required to open a unit area of crack, G_F, as a material parameter. With this approach the concrete tensile behavior is characterized by a stress-displacement response (Figure 3.4) rather than a stress-strain response. A concrete specimen will crack across some section under tension. After it has

been pulled apart sufficiently (most of the stress has been removed so that the undamaged elastic strain is small), its length will be determined primarily by the opening at the crack. The opening does not depend on the specimen size.

3.1.3.2 Compressive Behavior of Concrete Modeling

In concrete damaged plasticity model, the stress-strain behavior of concrete in uniaxial compression can be defined outside of the elastic range. Also, the strain-stress curve can be beyond the ultimate stress as shown in Figure 3.6. Compressive stress is a function of inelastic (or crushing) strain, $\tilde{\varepsilon}_c^{in}$. The compressive inelastic strain, $\tilde{\varepsilon}_c^{in}$, is defined as the total strain minus the elastic strain corresponding to the undamaged material, $\tilde{\varepsilon}_c^{in} = \varepsilon_c - \varepsilon_c^{el}$, where $\varepsilon_c^{el} = \frac{\sigma_c}{E_0}$, as illustrated in Figure 3.6.

Because of the assumption that no stiffness degrades after the peak stress, the equivalent plastic strain in compression is equal to the compressive inelastic strain, $\tilde{\varepsilon}_c^{pl} = \tilde{\varepsilon}_c^{in}$. Therefore, the stress-strain relationship in compression may be expressed as:

$$\sigma_c = E_0(\varepsilon_c - \tilde{\varepsilon}_c^{pl}) = E_0(\varepsilon_c - \tilde{\varepsilon}_c^{in}) \tag{3.6}$$
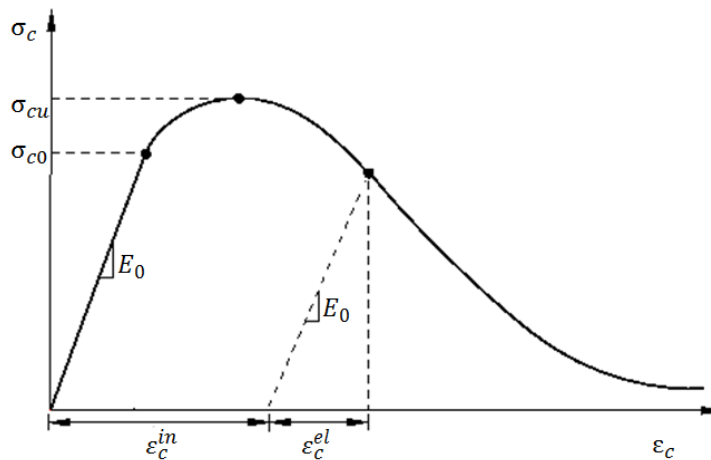
Figure 3.6 Compressive behavior modeling in concrete damaged plasticity model (Abaqus/standard User's Manual 2013)

3.1.3.3 Yield Function and Flow Rule

The yield function represents a surface that determines the states of failure or damage. The yield function in terms of stresses and plastic strains $F(\sigma, \tilde{\varepsilon}^{pl})$ is given by (Lubliner et al. 1989):

$$F(\tilde{\sigma}, \tilde{\varepsilon}^{pl}) = \frac{1}{1-\alpha}(q - 3\alpha p + \beta(\tilde{\varepsilon}^{pl})\hat{\sigma}_{max} - \gamma\langle -\hat{\sigma}_{max}\rangle) - \tilde{\sigma}_c(\tilde{\varepsilon}_c^{pl}) \le 0$$
$$p = \frac{1}{3}\tilde{\sigma}:I$$
$$q = \sqrt{\frac{3}{2}S:S} \tag{3.7}$$
$$S = pI + \tilde{\sigma}$$
$$\beta(\tilde{\varepsilon}^{pl}) = \frac{\tilde{\sigma}_c(\tilde{\varepsilon}_c^{pl})}{\tilde{\sigma}_t(\tilde{\varepsilon}_t^{pl})}(1-\alpha) - (1+\alpha)$$

where α and γ are dimensionless material properties, q is the Mises equivalent stress, p is hydrostatic pressure, S is the stress deviator, $\hat{\sigma}_{max}$ is the algebraically maximum principal stress, and $\tilde{\sigma}_c(\tilde{\varepsilon}_c^{pl})$ and $\tilde{\sigma}_t(\tilde{\varepsilon}_t^{pl})$ are tensile and compressive cohesion stresses, respectively.

In biaxial compression, with $\hat{\sigma}_{max} = 0$, $F(\tilde{\sigma}, \tilde{\varepsilon}^{pl})$ reduces to the well-known Drucker-Prager yield condition (Drucker and Prager 1952). In such case, the coefficient α can be determined from the initial equibiaxial and uniaxial compressive yield stress, σ_{b0} and σ_{c0}, as:

$$\alpha = \frac{\sigma_{b0} - \sigma_{c0}}{2\sigma_{b0} - \sigma_{c0}} \tag{3.8}$$

Typical experimental values of the ratio σ_{b0}/σ_{c0} for concrete are in the range from 1.10 to 1.16, yielding values of α between 0.08 and 0.12 (Abaqus/standard user's manual 2013).

The coefficient γ enters the yield function only for stress states of triaxial compression, when $\hat{\sigma}_{max} < 0$. Since plane stress analysis is used in this study, parameter γ does not play a role in the yield function. Figure 3.7 presents the damaged plasticity yield surface in plane stress analysis.
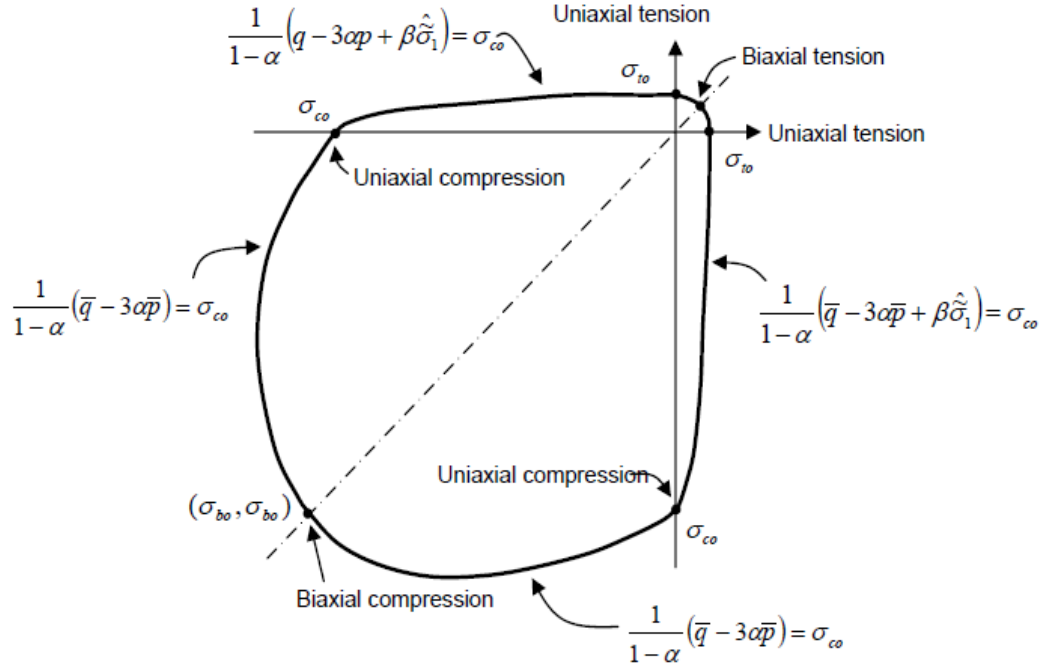
Figure 3.7 Yield surface in plane stress (Abaqus/standard user's manual 2013)

The damaged plasticity model using non-associated potential flow may be presented as:

$$\dot{\varepsilon}^{pl} = \dot{\lambda}\frac{\partial G(\tilde{\sigma})}{\partial \tilde{\sigma}} \tag{3.9}$$

Where $\dot{\varepsilon}^{pl}$ is the equivalent plastic strain rate, $\varepsilon^{pl} = \int_0^t \dot{\varepsilon}^{pl}dt$.

The flow potential G picked for this model is the Drucker-Prager hyperbolic function:

$$G = \sqrt{(\epsilon\sigma_{t0}tan\psi)^2 + q^2} - ptan\psi \tag{3.10}$$

where the dilation angle, ψ, is measured in the $p - q$ plane at high confining pressure, σ_{t0} is the uniaxial tensile stress at failure, and ϵ is a parameter referred to as the eccentricity that defines the rate at which the function approaches the asymptote. The flow potential tends to a straight line as the eccentricity tends to zero (Figure 3.8).
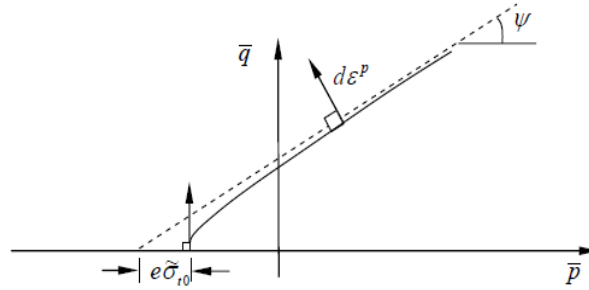
Figure 3.8 Flow potential in $p - q$ plane (Abaqus/standard user's manual 2013)

3.2 Extended Finite Element Model (XFEM)

Cracks in a FE model may cause singular stresses and strains close to a crack-tip, or a jump in displacement across a crack. For the numerical estimation of these non-smooth variables, there are two primarily different approaches. The first method is a polynomial approximation based on finite element shape functions, and requires the element mesh to conform to the discontinuities. In addition, a refined mesh is essential at the location close to the crack tip and remeshing is required in order to model the evolution of interfaces, e.g., crack propagations. However, an effective remeshing procedure can be difficult for complex geometries because the elements must conform to the geometry of the discontinuity or projection errors are introduced. Moreover, this is computationally expensive and not suitable for developing cracks. The second method is based on enriching the polynomial approximation space with discontinuous functions,

such that non-smooth solutions can be modeled independent of the mesh. This is a basic

principle of XFEM, and was pioneered by Melenk and Babuska (1996) and developed by

Belytschko and Black (1999) and Moës et al. (1999). The principal points of the XFEM

method provided in the finite element code ABAQUS (version 6.13) are presented in

following sections.

3.2.1 General Formulation of XFEM

For the crack modeling, the enrichment functions typically consist of the near-tip

asymptotic functions that catch the singularity around the crack tip and a discontinuous

function that characterizes the jump in displacement across the crack surfaces. The

degree of freedom enrichment is done with special displacement functions as shown in

Equation 3.11:

$$u = \sum_i N_i(x) \left[u_i + a_i H(x) + \sum_{j=1}^{4} b_i^j F_j(x) \right] \tag{3.11}$$

where $N_i(x)$ are the usual nodal shape functions; u_i is the usual nodal displacement; a_i

are the enriched degrees of freedom associated with crack separation away from the tip;

$H(x)$ is the associated discontinuous jump function across the crack; b_i^j are the nodal

enriched degrees of freedom associated with near-tip displacement; and $F_j(x)$ are the

asymptotic crack tip functions. In the bracket of Equation 3.11, the first term is valid for

all nodes in the model; the second term is used for nodes whose shape function is cut by

the crack interior (the part between the old and new crack tips); and the third term is

applicable only for nodes whose shape function is cut by the new crack tip.

Figure 3.9 shows normal and tangential coordinates for a smooth crack. The

discontinuous jump function across the crack surfaces, $H(x)$, is given by:

$$H(x) = \begin{cases} 1 & if \ (x - x^*).n \geq 0 \\ -1 & otherwise \end{cases} \tag{3.12}$$

where x is a sample (Gauss) point, x^* is the point on the crack closest to x , and n is the

unit outward normal vector to the crack at x^*.

The asymptotic crack tip functions in an isotropic elastic material, $F_j(x)$, are

given by:

$$F_j(x) = \left[\sqrt{r} \sin\frac{\theta}{2}, \sqrt{r} \cos\frac{\theta}{2}, \sqrt{r} \sin\frac{\theta}{2} \sin\theta , \sqrt{r} \cos\frac{\theta}{2} \cos\theta \right] \tag{3.13}$$

where r and θ are the polar coordinates from the crack tip as shown in Figure 3.9.
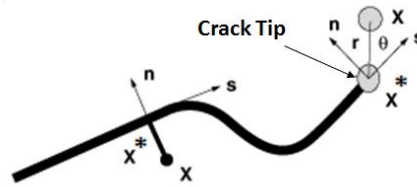
**Figure 3.9 Normal and tangential coordinates for a smooth crack
(Abaqus/standard user's manual 2013)**

3.2.2 Phantom Node Method

Modeling the crack tip singularity accurately requires continuously keeping track

of where the crack propagates. It is difficult because the degree of crack singularity

depends on the location of the crack in a non-isotropic material. Therefore, the

asymptotic singularity functions are considered only when modeling stationary cracks.

Moving cracks are modeled using an alternative approach based on traction-separation

cohesive behavior.

The XFEM-based cohesive method can be used to model crack initiation and

propagation along an arbitrary, solution-dependent path since the crack propagation is not

tied to the element boundaries in a mesh. The cohesive method is based on the insertion

of a cohesive segment through an element once a decohesion (damage) criterion is met.

The segments can be placed at arbitrary locations and in arbitrary directions, allowing for

the modeling of complex crack patterns. The segment is taken to extend through the

element to the boundary in which it is inserted. The cohesive behavior is explained in the

next chapter in details.

The XFEM-based cohesive method is based on the partition of unity property of

finite element shape functions and enriching the approximation space with discontinuous

functions. In this case, the near-tip asymptotic singularity is not needed. The

displacement jump across a crack is calculated using the Phantom node method.

Phantom nodes, which are superposed on the original real nodes, are introduced to

represent the discontinuity of the cracked elements, as shown in Figure 3.10. When the

element is undamaged, each phantom node is completely tied to its corresponding real

node. When the element is cut by a crack, the cracked element splits into two parts. Each

part is formed by a combination of some real and phantom nodes depending on the

orientation of the crack. Each phantom node and its corresponding real node are no

longer constrained together and can move separately.
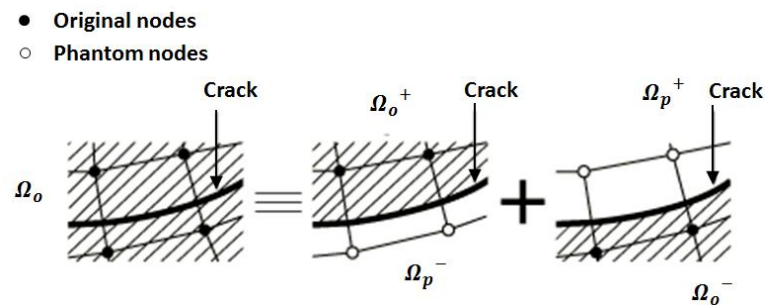
Figure 3.10 Principle of the phantom node method
(Abaqus/standard user's manual 2013)

The separation is governed by the traction-separation law until the cohesive strength of the cracked element is zero, after which the phantom and the real nodes move independently. To have a set of full interpolation bases, the part of the cracked element that is in the real domain, Ω_o, is extended to the phantom domain, Ω_p. Then the displacement in the real domain, Ω_o, can be interpolated by using the degrees of freedom for the nodes in the phantom domain, Ω_p. The jump in the displacement field is calculated by simply integrating only over the area from the side of the real nodes up to the crack, i.e., $\Omega_o{}^+$ and $\Omega_o{}^-$. This method provides an effective and attractive engineering approach and has been used for simulation of the initiation and growth of multiple cracks in solids by Song et al. (2006) and Remmers et al. (2008). It has been proven to exhibit almost no mesh dependence if the mesh is sufficiently refined.

3.3 Application of Concrete Damaged Plasticity Model in XFEM-Based Cohesive Method

As described in section 3.1, the concrete damaged plasticity model can simulate the constitutive behavior of concrete both in tension and compression. Although the application of this method in conventional finite element method is a well-known successful method, the concrete cracking in tension cannot be simulated as discrete cracks. Actually, the cracks in concrete subjected to tension are modeled as plastic displacements due to the continuum behavior assumption. On the other hand, XFEM-based cohesive model is able to simulate discrete cracks using phantom node method and traction-separation law. A crack is modeled as a geometrical discontinuity in displacement across the crack. In the specimens used in conducted experimental program of this study, concrete is subjected to both tensile and compressive stresses while

concrete is cracked in the region close to FRP/concrete interface. Therefore, the combination of concrete damaged plasticity model and XFEM-based cohesive method is proposed in this research to model the concrete behavior. The compressive behavior of concrete is modeled using the concrete damaged plasticity model. The concrete damaged plasticity model is used in coordination with the XFEM-based cohesive method to model the concrete behavior in tension. The damaged plasticity model is used until the tensile crack initiation is detected, at which a cohesive segment is inserted and the XFEM is activated.

The cohesive segments method is based on the fictitious crack using nonlinear fracture mechanics. The crack initiation criterion is the maximum principal stress criterion, in which a crack is initiated if the maximum principal tensile stress reaches the tensile strength of the concrete. The crack propagates perpendicular to the direction of the maximum principal tensile stress. The evolution of the crack is governed by the fracture energy, which represents the tension-softening behavior of the concrete during cracking. This method (application of concrete damaged plasticity model in XFEM-based cohesive method) is proposed for concrete modeling in the finite element analysis of the experiments of this study as described in Chapters 5 and 6.

Chapter 4 Modeling of FRP Debonding Failure in FRP/Concrete Joints

Since the debonding failure of FRP/concrete joints is due to a moving crack within concrete close to and along the FRP/concrete interface, fracture mechanics is more appropriate for the analysis. Because of that, fracture mechanics-based approaches to study the debonding failure of FRP bonded concrete joints have received attention (Chen and Teng 2001). In order to apply fracture mechanics for FRP debonding failure analysis, the traction-separation law (i.e. the stress-displacement relationship) is required to be defined. Damage modeling can simulate the degradation and eventual failure of the bond by using the traction-separation law.

In this chapter, four different fracture mechanics-based methods are investigated to model the FRP debonding in the finite element analysis including: cohesive elements, virtual crack closure technique (VCCT), cohesive surface, and XFEM. The finite element software ABAQUS is used for the numerical analysis. The results from different methods are compared with experimental results to find the most accurate method to model IC debonding failure of FRP-strengthened concrete beams.

4.1 Application of Cohesive Elements

For the first trial, cohesive elements are applied in the finite element models to predict IC debonding failure when the FRP/concrete interface is subjected to mixed-mode loading (the peeling force (mode I) and the shear force (mode II)). Cohesive elements are normally used to model the behavior of adhesive joints, interfaces in composites, and other situations where the integrity and strength of interfaces may be of interest. The

experimental results obtained from tests conducted by Dai et al. (2009) are used to validate the numerical analyses. Dai et al. (2009) developed an experimental test setup shown in Figure 4.1 to introduce different stress conditions into the FRP/concrete interface through loading the FRP-strengthened RC beams in different ways. As shown in the figure, a steel bar connected to the loading system was used to impose dowel force vertically onto the FRP sheets through a ball hinge and a stiff plate to create a localized mode I stress in the FRP concrete interface. The trapezoid shape was chosen for the void block to simulate the direction of actual diagonal flexural/shear cracks. In addition, a steel framework provided reactive bending force to the strengthened RC beams. As a result, the dowel force was introduced into the FRP sheets and a mode II interfacial stress condition was generated in the FRP/concrete interface. The mixed-mode loading condition could be achieved by altering the dowel force and bending force ratios. Six RC beams that externally bonded with two layers of CFRP sheets were tested. Dimensions of the specimens are shown in Figure 4.2. A 20 *mm* long initial crack (unbounded area) was set between the FRP sheets and the concrete beams. Two beams were subjected to dowel action and bending action only. Four additional specimens were loaded under mixed-mode action by a constant level of dowel force (35%, 50%, 75% and 90% of the interface dowel force capacity) while bending force was increased from zero to the failure loads of the beams. The bending load, dowel load, mid-span deflection, peeling crack opening displacement, and the relative displacement (interfacial slip) between the concrete and the CFRP sheet at the tip of the initial crack, and strains in FRP at different locations were measured during tests.
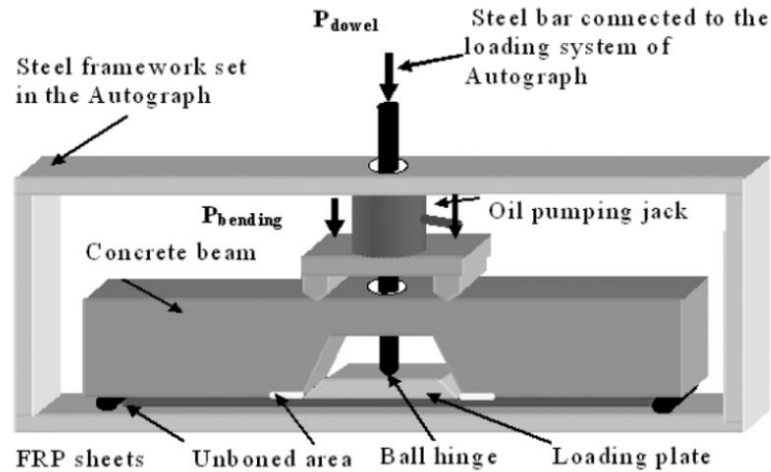
Figure 4.1 Sketch of test set up used by Dai et al. (2009)
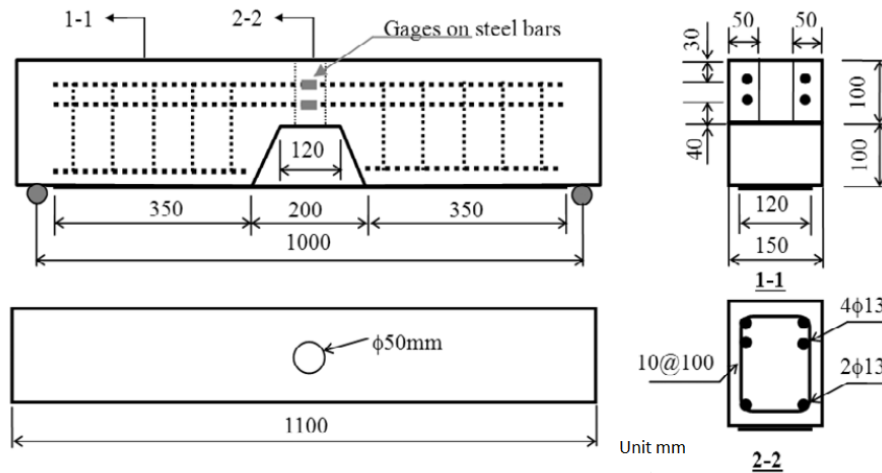
Figure 4.2 Dimensions of test specimens used by Dai et al. (2009)

It is observed in many experimental researches that debonding occurs in concrete at a few millimeters from the FRP/concrete interface and is essentially parallel to the interface. This phenomenon is due to two reasons: first, the penetration of adhesive into the concrete and increasing the toughness and the strength of a thin layer of mortar right next to the interface (Coronado and Lopez 2008); and second, the concrete substrate is the weakest component in FRP/concrete interface with a relatively small tensile strength. Based on this experimental observation, a thin damage band exposed to the mixed-mode

loading condition is modeled separately along the interface. Cohesive elements are used to model this damaged band.

4.1.1 Finite Element Analysis Using Cohesive Elements

Because of the symmetrical condition, only half of the beam is modeled. Concrete and FRP are modeled using 4-node bilinear 2D elements (CPE4R). The steel bars embedded in concrete (shown in Figure 4.2) are modeled using two nodes truss elements (T2D2). The damage band is modeled using four node two dimensional cohesive elements (COH2D4). The typical mesh of the model is shown in Figure 4.3.

Tied contact is used to connect the FRP sheet to the damage band, and the damage band to the rest of the concrete beam. The tied contact can fuse two regions together even though the meshes created on the surfaces of the regions are dissimilar. In this approach, the nodes on the slave surface have the same displacement as the point on the master surface to which it is closest.
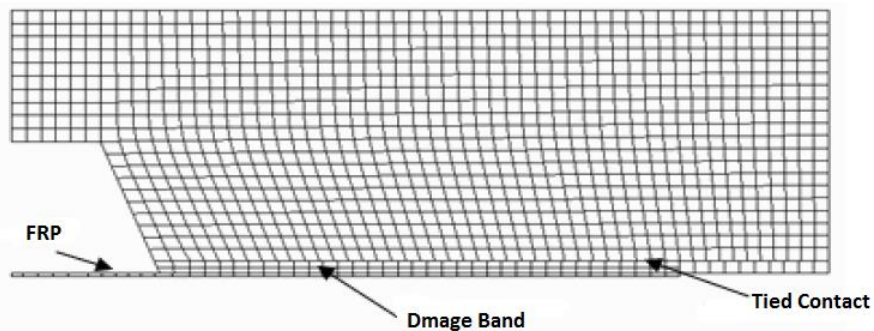
Figure 4.3 Typical finite element mesh for specimens used by Dai et al. (2009)

The behavior of steel is modeled as perfectly elastic-plastic response as shown in Figure 4.4a. The behavior of FRP is simulated using a brittle cracking model (Figure 4.4b); consequently, the stress-strain curve of FRP is assumed to be linear up to when the

failure stress is reached. At this point, the material loses all its load-carrying capacity suddenly. The concrete damaged plasticity model is used to model the nonlinear behavior of concrete. The concrete and damage band modeling are explained in details in the following.
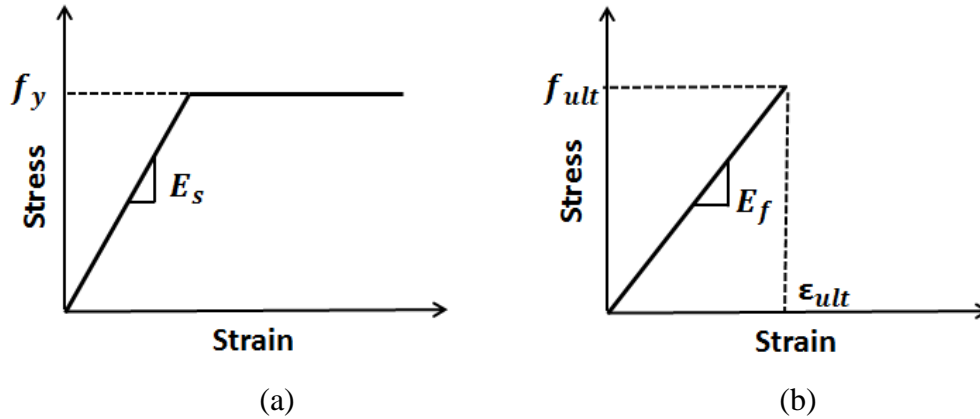
Figure 4.4 Stress-strain behaviors applied in FE analysis using cohesive element: (a) Steel, (b) FRP

4.1.2 Concrete Behavior Modeling

As it is described in the previous chapter, cracking plays an important role in concrete behavior. Since the strain localization occurs during cracking in quasi-brittle material like concrete, the failure behavior prediction by finite element analysis needs a special method. The concrete damaged plasticity model is able to simulate the behavior of concrete failure due to cracking both in tension and compression as discussed in the previous chapter.

In order to use the concrete damaged plasticity model, two curves should be determined. The first is the softening curve of concrete under uniaxial tension. Many different shapes have been proposed in the literature for the concrete softening curve,

which includes linear, bilinear, power functions, etc. (Shah et al. 1995). In this study, a simple linear stress strain softening curve as shown in Figure 4.5 is used. Two parameters are required to define the linear strain softening of concrete: maximum bearing stress, and fracture energy that is equal to the area under the softening curve. The concrete tensile strength, f_t, is considered as maximum stress that is estimated by $f_t = 0.62\sqrt{f_c'}$ (MPa) (ACI 318.R 2013) where f_c' (MPa) is the concrete compressive strength. Equation 4.1 proposed by Bazant and Becq-Giraudon (2002) can be used for assessment of the fracture energy G_F(N/m):

$$G_F = 2.5\alpha_0 \left(\frac{f_c'}{0.051}\right)^{0.46} \left(1 + \frac{d_a}{11.27}\right)^{0.22} \left(\frac{w}{c}\right)^{-0.3} \tag{4.1}$$

where d_a (mm) is the average aggregate diameter, $\alpha_0 = 1.44$ for crushed or angular aggregates, and $\frac{w}{c}$ is the water cement ratio.
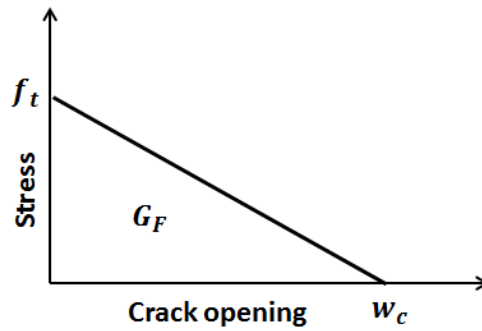
Figure 4.5 Linear approximation of concrete strain softening curve

The second curve needed for the concrete damaged plasticity model is the stress-strain curve of concrete under uniaxial compression. The concrete compression stress-strain curve is nonlinear and has a different shape for different concrete. In this study, the model proposed by Todeschini et al. (1964) as shown in Figure 4.6 is used to represent the concrete behavior under compression. For estimation of concrete Young's modulus,

E_c (*MPa*), Equation 4.2 (ACI 318.R 2013) is used:

$$E_c = 4700\sqrt{f_c'} \qquad\qquad (4.2)$$
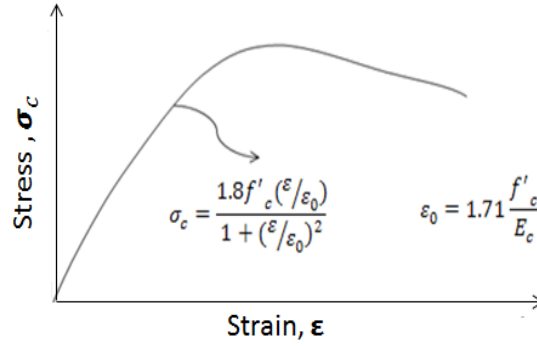
Figure 4.6 Compressive behavior model of concrete under uniaxial compression (Todeschini et al. 1964)

4.1.3 Damage Band Modeling

A damage band is created separately from the rest of the concrete to simulate the FRP/concrete interface subjected to mixed-mode loading along the initial crack. The cohesive elements are applied for the mesh of this band. The damage band must be discretized with a single layer of cohesive elements through the thickness.

In order to model the FRP/concrete interface, the constitutive response of cohesive elements is defined by a traction-separation law derived from fracture mechanics. In this study, a bilinear traction-separation law is assumed to model the bond behavior of the interface as shown in Figure 4.7. The failure mechanism consists of two components: a damage initiation criterion and a damage evolution law. In the bilinear law, the initial response is the ascending linear branch up to the damage initiation criterion. The damage initiation criterion uses the maximum traction to define the beginning of the interface response degradation. The area under the traction-separation

response is assumed equal to the fracture energy required for separating the unit area of the interface. The damage evolution law uses the fracture energy concept to describe FPZ at the tip of the damage.
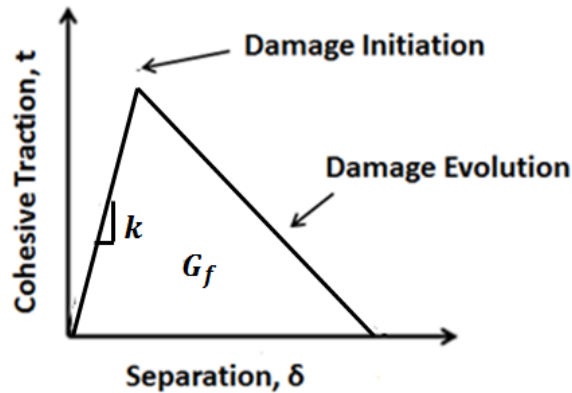
Figure 4.7 Bilinear traction-separation law in cohesive element

In general, cracks may be stressed in three different modes: mode I, the cleavage or tensile-opening mode; mode II, the in-plane shear mode; and mode III, the out-of-plane shear or tearing mode as shown in Figure 4.8. In a two-dimensional (2D) analysis, when the interface is subjected to mixed-mode loading, there are both opening (normal) and slip (shear) displacements of the crack. The initiation and propagation criteria of the traction-separation law can model the mixed-mode loading condition. Figure 4.9 is a schematic representation of the dependence of damage initiation and evolution on the mixed-mode for a traction-separation response. The figure shows the tractions on the vertical axis and the magnitudes of the normal and shear separations along the two horizontal axes. The unshaded triangles in the two vertical coordinate planes represent the responses under pure normal and shear separations. The shaded vertical planes A and B symbolize the damage responses in Mode I and Mode II under mixed-mode conditions, respectively, while the shaded triangle C shows the bond behavior of the interface under

mixed-mode loading. δ_m in this figure is the effective displacement defined as:

$$\delta_m = \sqrt{\delta_n{}^2 + \delta_s{}^2}$$

(4.3)

Where δ_n and δ_s are the normal and shear separations, respectively.

Figure 4.8 Three modes of a crack displacement (Shah et al. 1995)

Figure 4.9 Mixed-mode response in cohesive elements

In the present finite element analysis using cohesive elements, damage is assumed to initiate when the maximum nominal stress ratio reaches a value of one. This criterion can be represented as:

$$max \left\{ \frac{\sigma}{\sigma_n}, \frac{\tau}{\tau_s} \right\} = 1 \qquad (4.4)$$

where σ_n, and τ_s are the normal and shear bond strengths, respectively, and σ and τ are the normal and shear stresses of the cohesive element, respectively.

The power law model described in Wu and Reuter (1965) can provide mixed-mode contribution in the behavior of the cohesive element by:

$$\left(\frac{G_I}{G_{IC}} \right)^\alpha + \left(\frac{G_{II}}{G_{IIC}} \right)^\beta = 1 \qquad (4.5)$$

where G_I and G_{II} are the fracture energy components of Modes I and II, respectively; G_{IC} and G_{IIC} are the critical fracture energies in pure Mode I and pure Mode II loadings, respectively. It has been proposed by several researchers (Karbhari and Engineer 1996, Dai et al. 2009) that the relationship between the fracture energy components G_I and G_{II} of the FRP/concrete interface is linear. Therefore, the values of α and β are assumed to be equal to 1 in this study.

4.1.4 Material Properties Applied in FE Analysis Using Cohesive Element

The material properties used in the present FE model are presented in Table 4.1. The tensile and shear strengths of concrete are assigned to the damage band to control the initiation of the crack. The values of critical mode I and mode II fracture energies, G_{IC} and G_{IIC} assigned to the damaged band are calculated by Dai et al. (2009).

Table 4.1 Material properties applied in the FE analysis using cohesive elements

Properties	Concrete	Damage Band	FRP	Steel
Modulus of Elasticity, E (*GPa*)	31.5	31.5	230	210
Tensile Strength, (*MPa*)	4	4	3550	-
Compressive Strength, f_c', (*MPa*)	45	45	-	-
Shear Modulus, G, (*GPa*)	13	13	-	-
Shear Strength, τ_s, (MPa)	1	1	-	-
Fracture Energy, G_f, (*N/mm*)	0.1	Mode I=0.60 Mode II=0.99	-	-
Ultimate Strain	>0.003	>0.003	0.015	>0.2
Poisson's Ratio	0.2	0.2	0.3	0.3

4.1.5 Sensitivity Analysis

Several parameters can affect the FRP debonding failure. In this part of the study, thickness of damaged band and bending stiffness of FRP are selected to study their effects on the IC debonding failure of FRP-strengthened RC beams. Two beams from Dai et al. (2009), B4 and B6, are chosen to demonstrate the sensitivity analysis of these two parameters. Beams B4 and B6 are subjected to 50% and 90% of its dowel force capacity, respectively.

To find the accurate damage band thickness, four thicknesses are used in different FE models. They are 2, 4, 7, and 10 *mm*. The load vs. mid-span deflection curves for B4 and B6 are shown in Figure 4.10. It can be seen in the figure that the beam behaviors are not very sensitive to the damage band thicknesses although the model with 10-*mm*-thick of damage band produces the results closer to the experimental data. In the following models, 10 *mm* is used as the thickness of the damaged band. By comparing Figure 4.10a (dowel force is 50% of its capacity) to 4.10b (dowel force is 90% of its capacity), it can be seen that the effect of the damage band thickness is smaller when larger dowel force is applied. Larger dowel force introduces large mode I force to the FRP/concrete interface. Therefore, it can be concluded that the thickness of damage band is not a key parameter

when mode I loading dominates the debonding failure.
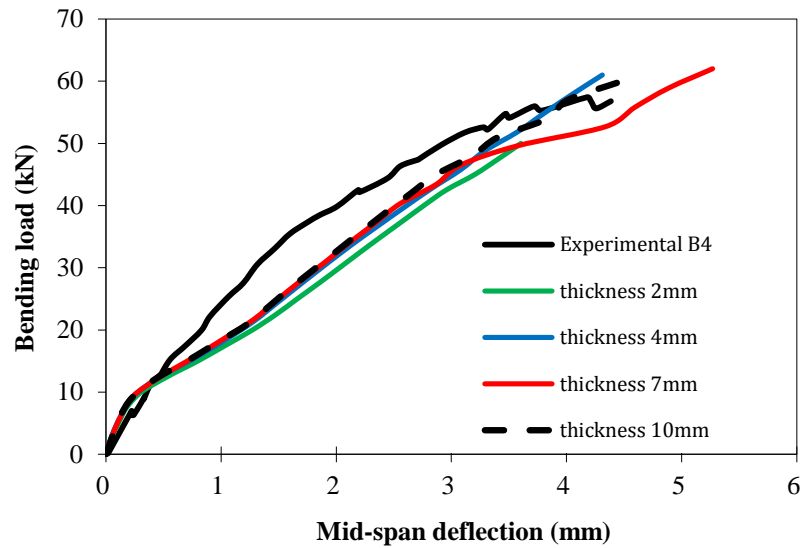
(a) Beam B4
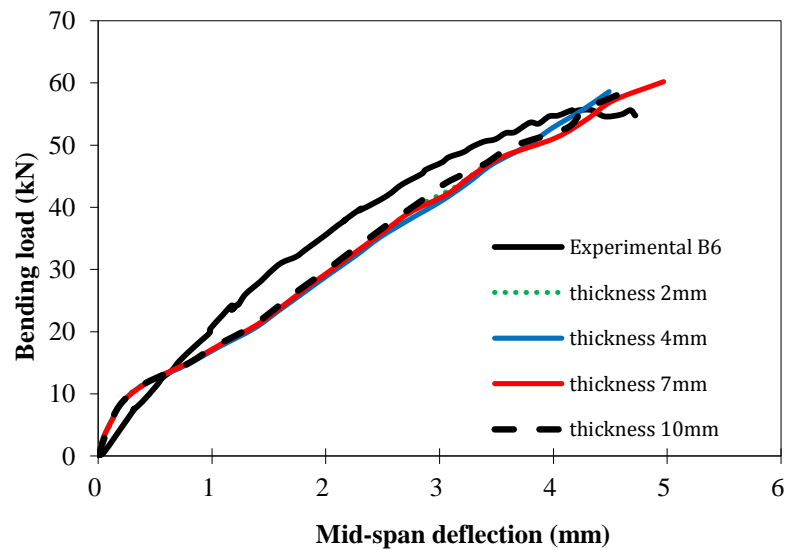
(b) Beam B6

Figure 4.10 Sensitivity to the thickness of damage band

In the experimental program reported by Dai et al. (2009), the CFRP sheets were applied to the RC beam by wet lay-up. The flexural stiffness of a CFRP sheet is relatively

small and is significantly influenced by the hand layer-up process. Therefore, it is hard to obtain the accurate flexural stiffness of CFRP in the beams. Dai et al. (2009) proposed the experimental magnitude of $EI = 228000$ N/mm^2 for the two layers of CFRP sheets in the beams by using the least-square root regression of the dowel force vs. crack tip opening displacement relationship. It is assumed that the debonded FRP acted as a cantilever beam. Because the crack length kept changing when the load was increased (i.e., the length of cantilever beam changed at different loading stages), the slope of dowel force vs. the crack tip opening displacement curve might not represent the FRP bending stiffness. In this study, three FRP flexural stiffness values, i.e., EI, $2EI$ and $3EI$, where EI $= 228000$ N/mm^2, are chosen to study the FRP flexural stiffness effects on the beams B4 and B6. The numerical results are compared to the experimental data as shown in Figure 4.11. It can be seen that FRP flexural stiffness has a significant effect on the behavior of the strengthened beams. The stiffness and ultimate loading capacity of the strengthen beam increased with the increase of FRP bending stiffness. The bending stiffness of $3EI =$ 684000 N/mm^2 has the best agreement with the experimental data. Therefore, 684000 N/mm^2 is assigned to the FRP bending stiffness in the following models.

4.1.6 Numerical Results of FE Analysis Using Cohesive Element

Five strengthened beams with IC debonding failure (B2 to B6) are analyzed in the FE models by using the parameters discussed in the previous sections. The bending peak loads of both numerical and experimental results are presented in Table 4.2. The experimental and numerical bending load vs. mid-span deflection curves of the beams are shown in Figure 4.12. The change of FRP axial strain with increasing of the bending load,

for beam B4 and B6 are shown in Figure 4.13. The FRP strains were obtained on the outer surface of the CFRP sheet at the center of the beam.
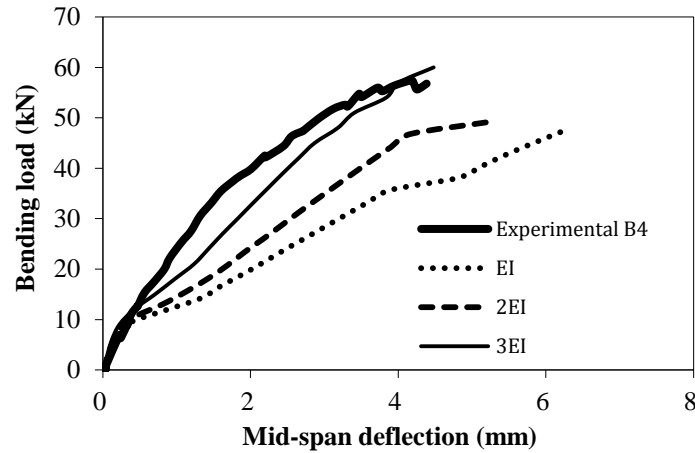
(a) Beam B4
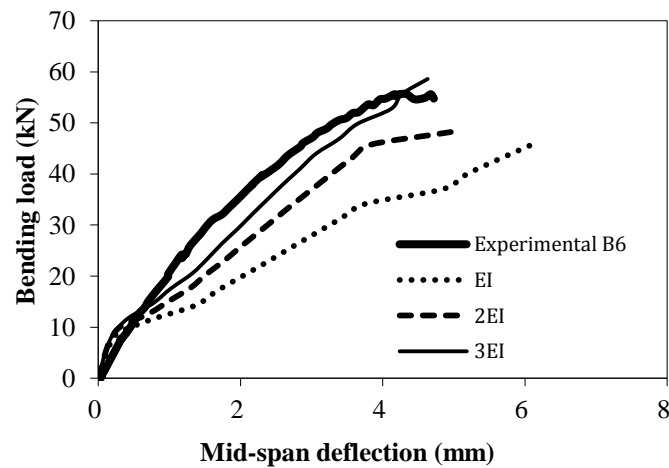
(b) Beam B6

Figure 4.11 Sensitivity to the FRP bending stiffness

Table 4.2 Summary of experimental and numerical results of the bending peak load

Beam	P_{dowel} (N)	$P_{bending, max}$ Experimental (KN)	$P_{bending, max}$ Numerical (KN)
B1	2000	0	-
B2	0	62	63.6
B3	700	65.2	62.7
B4	1000	57.4	60
B5	1400	53.6	59.4
B6	1900	55.6	58.6
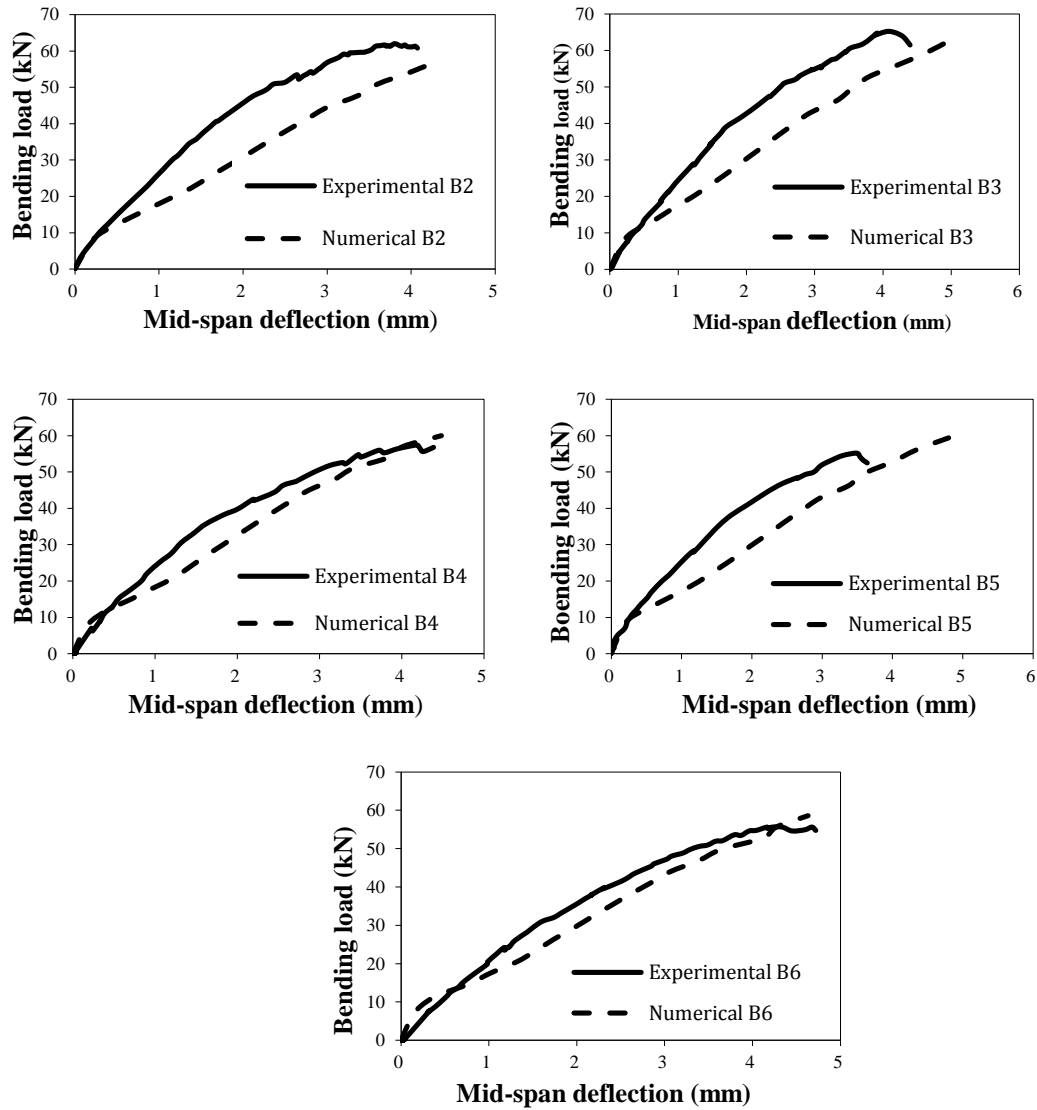
Figure 4.12 Numerical and experimental results for load-deflection behavior
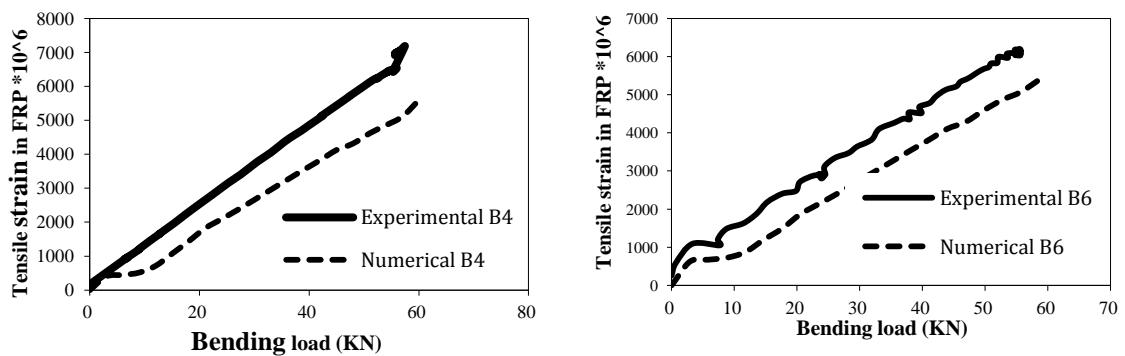
Figure 4.13 Predicted numerical FRP strain–load curves vs. experimental data

It can be seen in Figures 4.12 and 4.13 that the applied FE analysis using cohesive elements is able to capture the trend of beam behaviors. However, the numerical results of all beams are softer than the experimental data and have larger mid-span deflections. This issue is more noticeable in beams with smaller dowel loads. It means that the FE model using cohesive elements is not able to capture the stiffness and bearing load during the FRP debonding when the interface loading is dominated by Mode II force (shear). However, it can predict the peak load well with the mean parentage error of 3.5%.

The responses of the FE models and the actual beams are almost identical before the initial crack starts to propagate (Figure 4.12). However, the models show more flexible responses as the crack propagates. When the load increases, the cohesive elements continue to deform and therefore the crack propagates continuously in the FE models. In the real beams, the crack stops at a stable condition until the fracture energy at the crack tip accumulates to the critical fracture energy. Therefore, the crack propagation in the real beams is not continuous. It can be seen in Figure 4.12 that the load vs. displacement curves are 'jagged' for the real beams representing the repeated stable and crack propagating stages. In the ultimate stage, the behaviors of FE models and real beams become similar again. This is because FRP sheets in both the model and real beams have debonded completely from the concrete at this ultimate stage.

The another disadvantage of using cohesive elements for debonding modeling is that it is not possible to track the crack initiation and propagation since there is not a 'real' crack in the model and the behavior of modeling is controlled by cohesive element deformation (Figure 4.14). Hence, it is not possible to check the relationship between crack length and load. Using the cohesive elements deformation to model the cracking in

concrete may also result in the numerical model being more flexible than the experimental results.
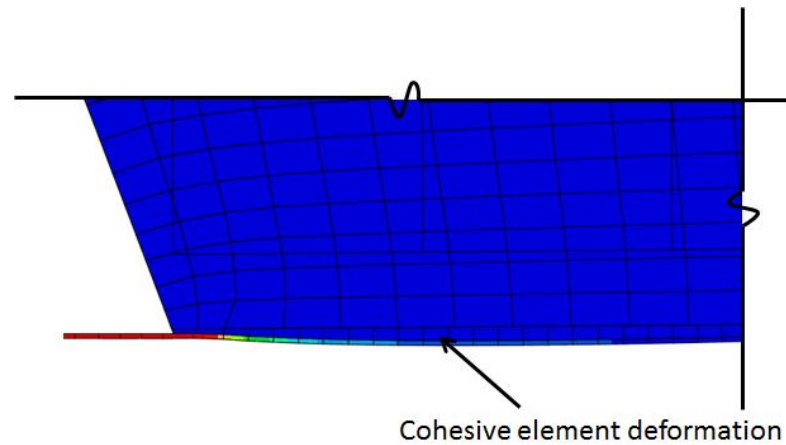
Figure 4.14 Cohesive element deformation to model cracking in concrete

4.1.7 Conclusion of Cohesive Element Application in FE Analysis

Two main conclusions are obtained in this part of study: first, FRP flexural stiffness has a noticeable effect on the behaviors of the strengthened beams; and second, the cohesive elements are not sufficient enough for the numerical analysis of debonding failure of FRP-strengthened concrete beams if crack propagation is an objective of study. Further study is conducted based on these conclusions to find other methods to model FRP debonding behavior in the FE analysis that are presented in the following section.

4.2 Application of VCCT, Cohesive Surface, and XFEM Methods for FRP Debonding Modeling

In order to find an appropriate numerical technique, three additional methods including the virtual crack closure technique (VCCT), cohesive surface, and XFEM are studied to investigate their abilities to model the FRP/ concrete interface debonding

failure when the interface is subjected to the mixed-mode loading condition. All of these methods are fracture mechanics-based models.

The experimental data obtained from Wan et al. (2004) are used to validate the numerical models in this part of study. Wan et al. (2004) developed a modified double cantilever beam (MDCB) test as shown in Figure 4.15 to evaluate the bond interfacial fracture energies between FRP and a concrete substrate under mixed-mode loading. The test frame includes a loading device, a load indicator, an adjustable MDCB holder to impose variable loading angles, and a displacement indicator. In this test set up, when the support rotates to different angles with respect to the horizontal plane (Figure 4.15b), the crack tip is subjected to different mixed-mode (Modes I and II) loading conditions. The loading angle α was changed between 0° and 60° during the test. The experimental process and analysis of the experimental results can be found in Wan et al. (2004).

(a)   (b)
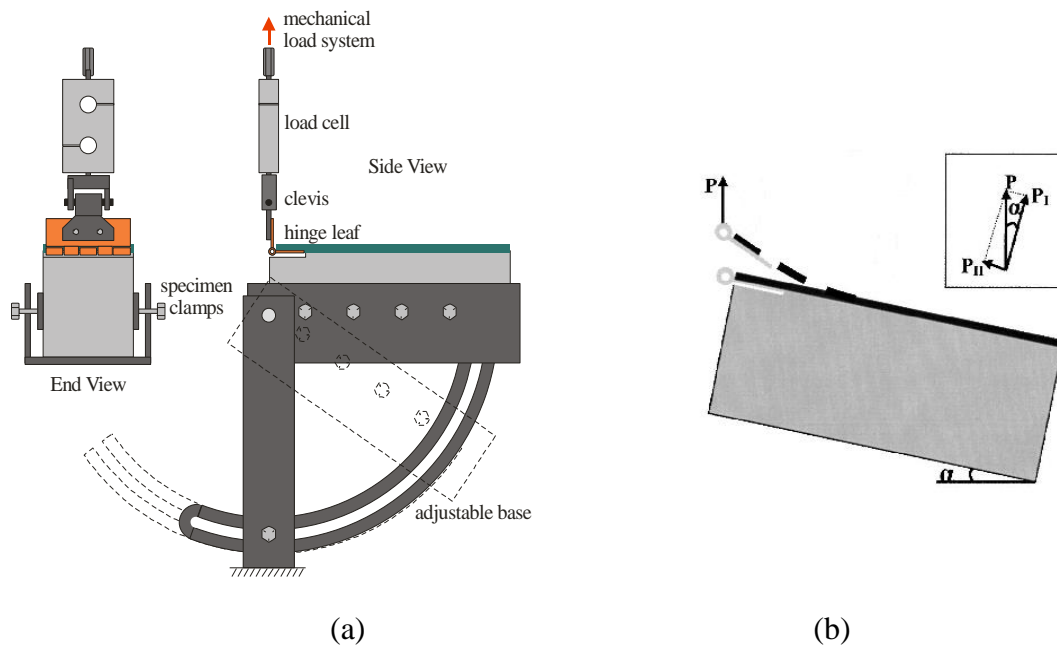
Figure 4.15 Schematic of MDCB test: (a) test frame and holder, (b) specimen (Wan et al. 2004)

4.2.1 Virtual Crack Closure Technique (VCCT)

The virtual crack closure technique (VCCT) uses LEFM principles in FE analysis and is therefore appropriate for materials in which brittle crack propagation occurs along predefined surfaces. In VCCT, it is assumed that the strain energy released when a crack is extended by a certain amount is the same as the energy required to close the crack by the same amount (Krueger 2004). Figure 4.16 shows the fraction criterion of VCCT for a crack extension when bonded surfaces are subjected to Mode I loading. Nodes 2 and 5 in this figure start to release when:

$$\frac{G_I}{G_{IC}} = \frac{1}{2}\left(\frac{v_{1,6}\, F_{v,2,5}}{bd}\right)\frac{1}{G_{IC}} = 1 \tag{4.6}$$

where G_I is the Mode I fracture energy, G_{IC} is the critical Mode I fracture energy, b is the width, d is the length of the elements at the crack front, $F_{v,2,5}$ is the vertical force between nodes 2 and 5, and $v_{1,6}$ is the vertical displacement between nodes 1 and 6. Assuming that the crack closure is governed by linear elastic behavior, the energy to close the crack (and thus the energy to open the crack) is calculated from Equation 4.6. The Same equation can be written for Mode II. In the general two dimensional analysis involving Mode I and II, the fracture criterion is defined as:

$$\frac{G_{equiv}}{G_{equivC}} = 1 \tag{4.7}$$

where G_{equiv} is the equivalent fracture energy calculated at a node, and G_{equivC} is the critical fracture energy. The power law, Equation 4.5, is used to calculate G_{equivC}. A linear fracture criterion for mixed-mode loading is assumed in this study:

$$\left(\frac{G_I}{G_{IC}}\right) + \left(\frac{G_{II}}{G_{IIC}}\right) = 1 \tag{4.8}$$

where G_I and G_{II} are the fracture energy components of Modes I and II, respectively; G_{IC}

and G_{IIC} are the critical fracture energies in pure Mode I and pure Mode II loadings,

respectively.
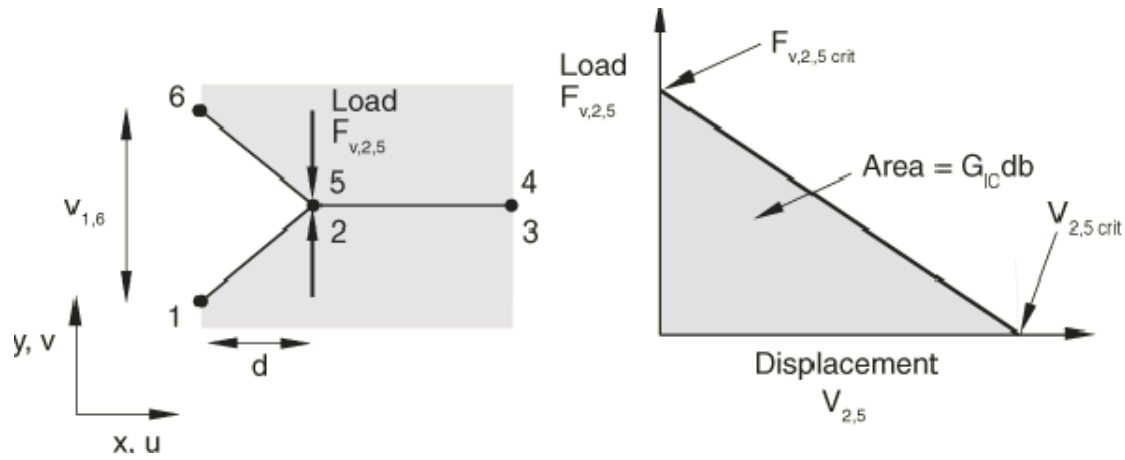
**Figure 4.16 Fraction criterion of VCCT for pure mode I
(Abaqus/standard user's manual 2013)**

4.2.2 Cohesive Surface Method

The conventional cohesive element method allows the specification of the

traction-separation behavior for elements to model FRP debonding failure. The cohesive

surface method uses the same approach for the modeling but specifies the traction-

separation behavior for the predefined surfaces instead of elements. The formulae and

laws that govern cohesive surface behavior are very similar to those used for cohesive

elements with traction-separation constitutive behavior. The failure mechanism including

the degradation and the eventual separation between the two cohesive surfaces consists of

two components: a damage initiation criterion and a damage evolution law. However, it

is important to recognize that damage in surface-based cohesive behavior is an interaction

property, not a material property. Concepts of strain and displacement (used in behavior

model formulae for cohesive elements) are reinterpreted as contact separations. Contact

separations are the relative displacements between the nodes on the predefined bonded surfaces along the contact normal and shear directions.

The damage initiates when the contact stresses and/or contact separations satisfy damage initiation criterion. For the present study, an elliptic form for damage initiation criterion is considered:

$$\left(\frac{\sigma}{\sigma_n}\right)^2 + \left(\frac{\tau}{\tau_s}\right)^2 = 1 \tag{4.9}$$

where σ_n and τ_s are the normal and shear bond strengths of the interface, respectively; σ and τ are the normal and shear stresses of the contact under mixed-mode loading, respectively.

The damage evolution law describes the rate at which the cohesive stiffness is degraded after the initiation criterion has been reached. Again, a linear fracture criterion for mixed- mode loading is assumed as given by Equation 4.8.

4.2.3 Extended Finite Element Model (XFEM)

Extended finite element model (XFEM) was proposed in the context of fracture mechanics by Belytschko and Black (1999). XFEM allows the presence of discontinuities (cracks) in an element of the finite element model by enriching the element with additional degrees of freedom. This technique can model crack opening and increases the accuracy of the approximation near the crack tip.

Modeling the crack tip singularity accurately requires continuously keeping track of where the crack propagates. It is difficult because the degree of crack singularity depends on the location of the crack in a non-isotropic material. The alternative approach to solve this issue is using cohesive segments within the framework of XFEM. Unlike

VCCT and cohesive surface methods, which need to have predefined paths align with element boundaries for the crack propagation, the XFEM-based cohesive behavior method can model crack initiation and propagation along an arbitrary, solution-dependent path in the bulk material, and crack propagation is not tied to the element boundaries in a mesh. In the finite element analysis using XFEM-based cohesive model, Equations 4.9 and 4.8 are used as the damage initiation and damage evolution criteria, respectively.

4.2.4 Comparison of Applied Methods

VCCT, cohesive surface, and XFEM methods are applied to model the MDCB specimen debonding behaviors. The specimen dimensions and typical mesh of the model are shown in Figure 4.17.

(a)   (b)
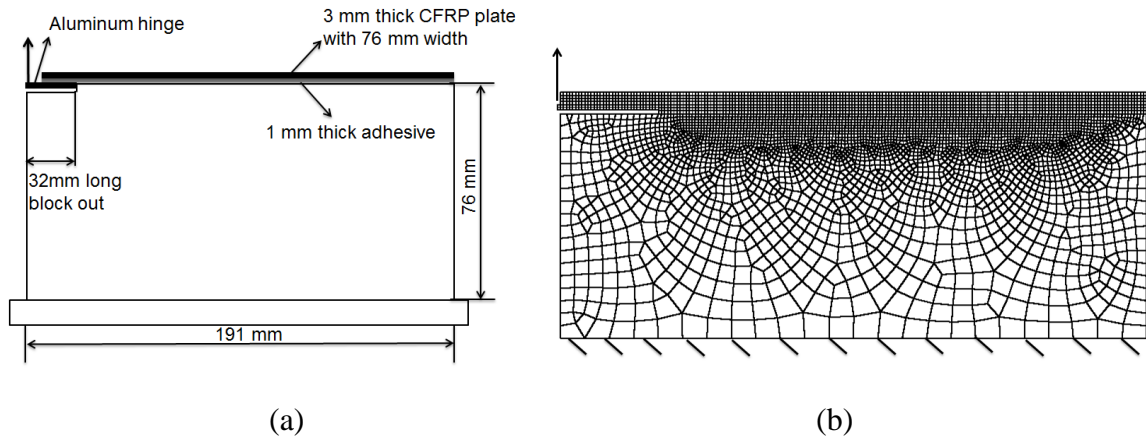
Figure 4.17 MDCB specimens: (a) specimen dimensions, (b) typical mesh

In XFEM, it is required to define a domain region in which the crack probably propagates through. A damage area is created to simulate the concrete close to the FRP/concrete interface in the FE model using XFEM. The traction-separation law

presented in Equations 4.8 and 4.9 is assigned to this area to predict FRP debonding failure.

Concrete material is modeled using the concrete damaged plasticity model. The behaviors of the FRP, epoxy, and aluminum hinge are modeled using a brittle cracking model. Since the debonding occurs in the concrete side of the interface, the normal strength of the interface, σ_n, is assumed to be equal to the concrete tensile strength. The shear strength, τ_s, and the critical fracture energy in pure mode II, G_{IIC}, of the interface are obtained from the bilinear model proposed by Lu et al. (2005) (Equations 2.4a to c).

The material properties used in the FE models are presented in Table 4.3. The concrete fracture energy, G_F, is required in order to use the concrete damaged plasticity model. G_F is assumed to be equal to 0.15 *N/mm* regarding to the concrete compressive strength; this value is consistent with recommendations of Wittman (2002). Coronado and Lopez (2008) indicated that the fracture energy of the interface, G_{IC}, is higher than the plain concrete fracture energy. Therefore, G_{IC} is assumed to be equal to 0.2 *N/mm* for the MDCB specimens.

Table 4.3 Material properties used in FE analysis for the MDCB specimens

Material Property	Concrete	FRP	Interface	Epoxy	Hinge
Young Modulus, E, (*GPa*)	33.10	217.5	-	3.18	70
Poison Ratio, v	0.28	0.20	-	0.34	0.30
Compressive Strength, f_c', (*MPa*)	53	-	-	-	-
Tensile Strength, f_t, (*MPa*)	4.59	-	-	-	-
Normal Strength, σ_n, (*MPa*)	–	-	4.59	-	-
Shear Strength, τ_s, (*MPa*)	-	-	5.13	-	-
Fracture Energy, G_F, (*N/mm*)	0.15	-	$G_{IC}=0.20, G_{IIC}=0.37$	-	-

Three FRP-strengthened concrete blocks tested by Wan et al. (2004) with different loading angles are analyzed using FE models incorporating VCCT, cohesive surface, and XFEM techniques. Figure 4.18 shows the curves of load vs. vertical

displacement at the loading end for experimental data and the numerical results. It can be seen in the figure, that all three methods are able to predict the trend of specimen behaviors and the debonding failure.
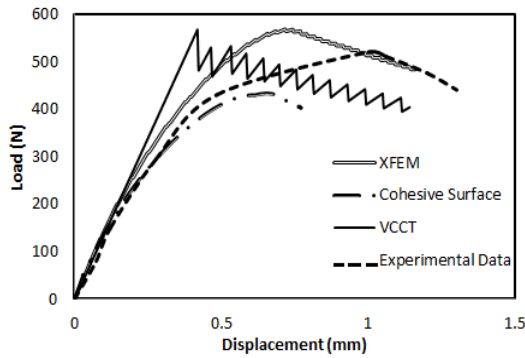
(a) Specimen C4B11 ($\alpha=0°$)
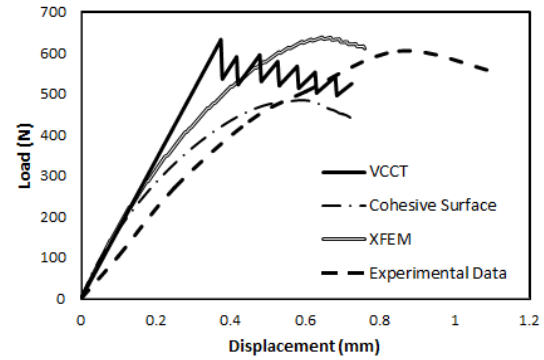
(b) Specimen C4B12 ($\alpha=30°$)
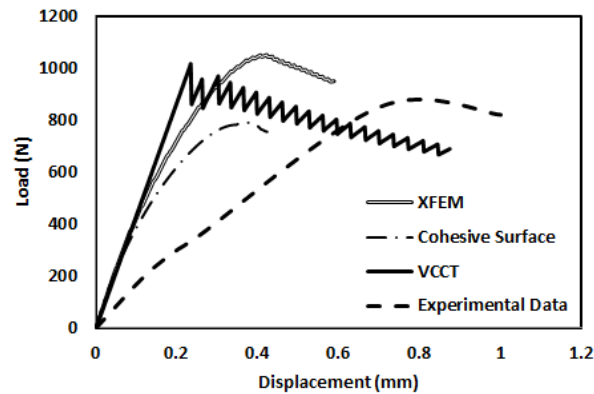
(c) Specimen C4B13 ($\alpha =60°$)

Figure 4.18 Load vs. vertical displacement at the loading end curves:

VCCT uses LEFM principles and assumes linear behavior for the materials. Therefore, its application is easy and analysis time is the shortest among the three methods. However, it is not able to capture the nonlinear behavior of the debonding failure resulting in predicted stiffer responses (smaller displacements) in numerical analyses compared to the experimental data. VCCT also requires a pre-defined flaw at the

beginning of the crack surface and cannot model the crack initiation from a surface that is not cracked.

The maximum loads obtained by the cohesive surface method are less than the experimental data. The reason is that the cohesive surface does not consider the thickness of the interface. Therefore, it is suitable for situations where the thickness of the interface is close to zero. Based on the test observations, the debonding occurs in the concrete side of the interface and FRP debonding failure propagates in a band along the FRP/concrete interface with variable thickness of attached concrete. Therefore the assumption of zero for the thickness of the interface is not correct. On the other hand, since XFEM applies a damage domain for the crack propagation, its load predictions are more compatible with the experimental results. The mean percentage errors of the peak loads in cohesive surface and XFEM methods are 16.9% and 7.4%, respectively.

XFEM uses the enrichment of degrees of freedom for the elements that the crack propagates through. Therefore, XFEM needs a finer mesh and as a result, the computational time is the longest.

Figure 4.19 presents the crack propagation in the models using cohesive surface and XFEM, respectively. In the former method, the debonding arises between the epoxy layer and the concrete, whereas in the latter method the debonding propagates in the concrete layer near the interface which is closer to the reality. Therefore, XFEM is a more objective method to predict the FRP debonding failure compared to the other two methods.

(a)

(b)
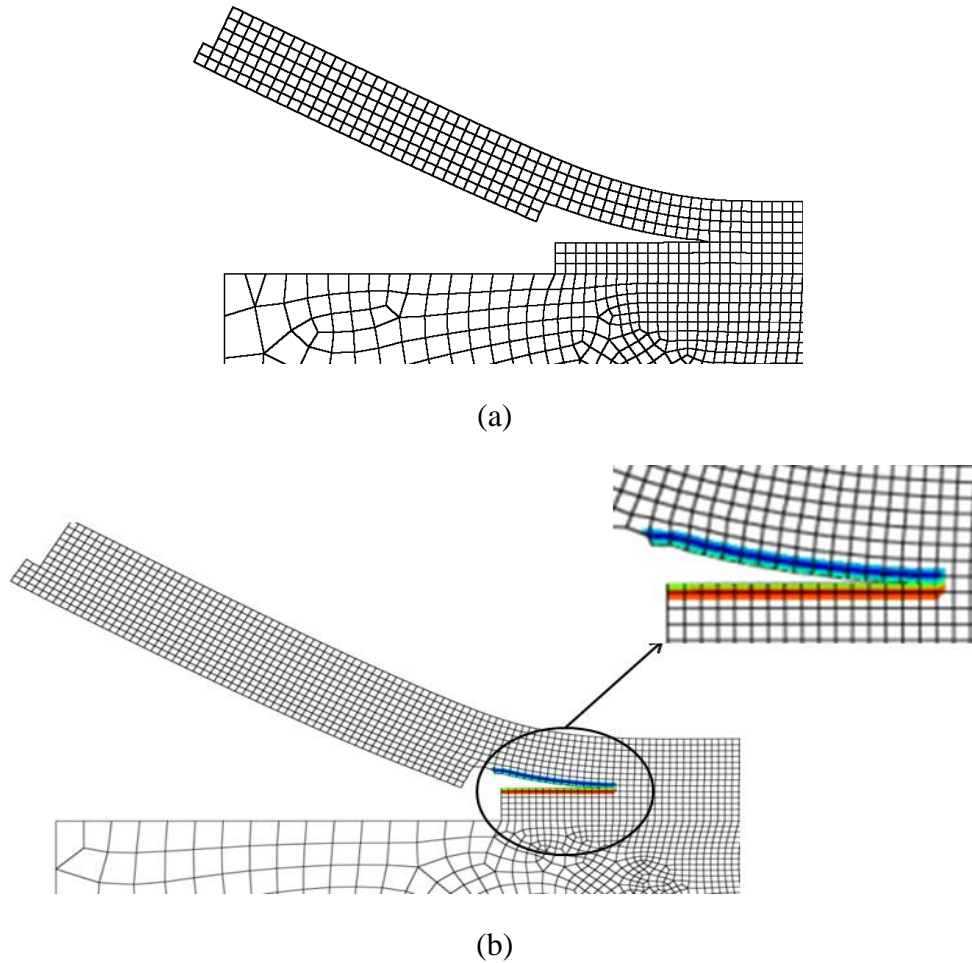
Figure 4.19 Debonding failure: (a) cohesive surface method, (b) XFEM

4.3. IC Debonding Modeling in FRP-strengthened Concrete Beams Using XFEM

According to Figure 4.18, the numerical results from traction-separation law-based methods are stiffer than the experimental ones. Although this is typical when modeling concrete structures, the difference between the stiffness of the numerical and experimental results increases when the loading angle is increased. On the other hand, as the contribution of mode II increases, the accuracy of the stiffness in the numerical model

decreases. In the modeling in Section 4.2, the Young's and shear moduli of concrete are assigned to the domain area of cracking. This is acceptable when the interface is under pure mode I loading. However, when the interface is subjected to mode II loading, the initial stiffness of the interface, k in Figure 4.7, is less than $\frac{G_c}{t_c}$ of the plain concrete according to Equation 4.10 (Toutanji et al. 2012):

$$k = \frac{G}{t} = \frac{1}{\frac{t_a}{G_a} + \frac{t_c}{G_c}} \tag{4.10}$$

where G_c, G_a, t_c, and t_a are shear moduli, and thicknesses of the concrete contribution and the adhesive, respectively. In order to obtain a better FE model for the interface subjected to Mode II loading, Equation 4.10 for the initial stiffness is used for the FE analysis of FRP-strengthened concrete beams. The experimental specimens and data from Harries et al. (2012) are used to verify the FE model using the XFEM for IC debonding failure analysis.

A practical standardized beam test method for assessing the FRP-to-concrete bond behavior in FRP-strengthened beams is proposed by Harries et al. (2012). The notched three-point bending beam specimen, shown in Figure 4.20, used for standardization is similar to that used to determine the modulus of rupture of concrete (ASTM C78 2010). To capture the IC debonding failure, the beam is notched at mid-span to one half of the beam depth to simulate the cracked concrete. Nine specimens reported by Harries et al. (2012) are considered in this study (three repetitions of three specimens). The details of specimens are presented in Table 4.4.
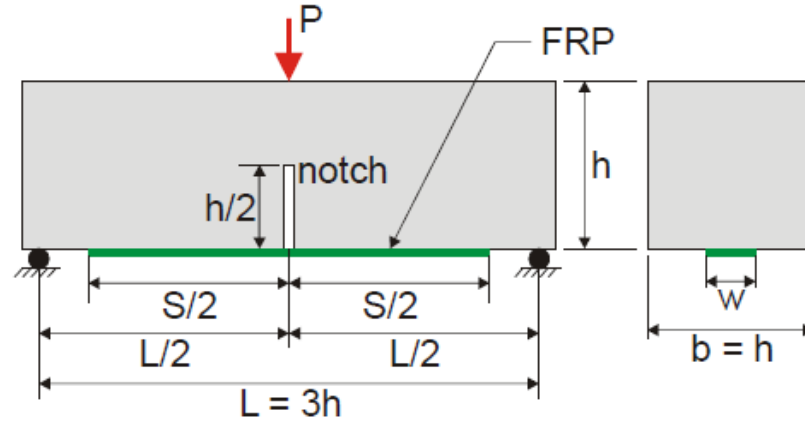
Figure 4.20 Beam test specimen using by Harries et al. (2012)

Table 4.4 Specimen details used by Harries et al. (2012)

Specimens	h=b=L/3 (*mm*)	w (*mm*)	t_f (*mm*)	S (*mm*)
G1-A, B and C	152	25	1.9	380
G2-A, B and C	152	50	1.9	380
G3-A, B and C	152	75	1.9	380

4.3.1 Finite Element Analysis Using XFEM-Based Cohesive Method

In order to find the appropriate element size for the FE models for the beam specimens, three meshes with different element sizes are formulated. The maximum bearing load obtained from the different mesh sizes are compared in Table 4.5. There is no significant difference between the results obtained from mesh b and mesh c, so mesh b is selected for the following FE models. In XFEM, it is required to define a domain region through which the crack probably propagates. The thickness of this area is assumed to be equal to 2 *mm*. Figure 4.21 shows the typical finite element mesh and the debonding crack domain (red rectangles).

Table 4.5 Mesh size study

Mesh	Elements Numbers	P_{max} (KN)
a	8564	30.85
b	16923	28.75
c	31845	28.54
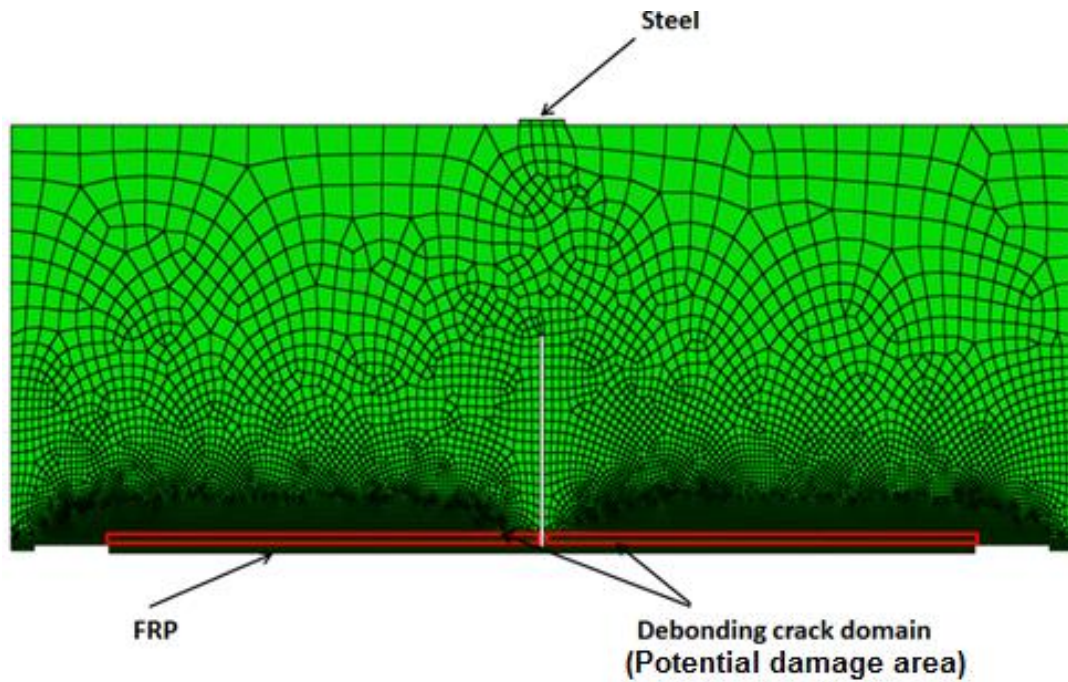
Figure 4.21 Typical mesh used for finite element analysis using XFEM-based cohesive method

The properties of material used in the finite element method are presented in Table 4.6. Concrete material is modeled using the concrete damaged plasticity model. The bilinear traction separation law for mode II loading is assigned to the damage area (debonding crack domain). The initial shear stiffness is calculated by Equation 4.10. Equations 4.8 and 4.9 are used as the debonding initiation and propagation criteria.

The maximum shear stress and interfacial mode II fracture energy calculated by proposed equations by Dai et al. (2005) (Equations 2.3a to c) and Lu et al. (2005) (Equations 2.4a to c) are shown in Table 4.7 for specimen G3.

Table 4.6 Material properties used in XFEM

Material Property	Concrete	GFRP	Adhesive
Young Modulus, E, (GPa)	26.1	41.37	1.2
Compressive Strength, f_c', (MPa)	32	-	-
Tensile Strength, f_t, (MPa)	3.5	-	-
Poison Ratio, v	0.25	0.2	0.3
Fracture Energy, G_F, (N/mm)	0.1	-	-

Table 4.7 Predicted values for bond-slip characteristics

Model	τ_s (MPa)	G_{IIC} (N/mm)	P_{max} (KN)
Dai et al. (2005)	4.29	1.565	37.2
Lu et al. (2005)	5.36	0.585	>42

The numerical analysis shows that application of the maximum shear stress and interfacial mode II fracture energy values from the equations proposed by Dai et al. (2005) and Lu et al. (2005) result in very high maximum bearing load compared to the results from experiments (the average value of the experimental maximum bearing load is 26.84 KN) as shown in Table 4.7 and Figure 4.22. Due to the high value of τ_s proposed by Lu et al. (2005), there is no crack initiation in the FE analysis used this value and the model exhibits a convergence problem. The values of τ_s =1.5 MPa and G_{IIC} = 0.6 N/mm result in the best agreement with the experimental results for specimen G3 (blue curve in Figure 4.22 with the mean percentage error of 5.6% of the maximum load). It is indicated in Harries et al. (2012) that the failure of the most of these specimens was characterized as an adhesive failure between the FRP and adhesive at lower loads than anticipated. This failure suggests improper preparation of the FRP strips prior to installation although it had no impact on the objective of this part of study.

The applied crack domain properties (debonding properties) in XFEM-based cohesive analysis are shown in Table 4.8.

Table 4.8 Debonding properties used in XFEM

Debonding property	G1	G2	G3
Young's Modulus, E, (*GPa*)	26.1	26.1	26.1
Normal Strength, σ_n, (*MPa*)	3.56	3.56	3.56
Shear Strength, τ_s, (*MPa*)	0.9	1	1.5
Fracture Energy Mode I, G_{IC}, (*N/mm*)	0.15	0.15	0.15
Fracture Energy Mode II, G_{IIC}, (*N/mm*)	0.49	0.56	0.6
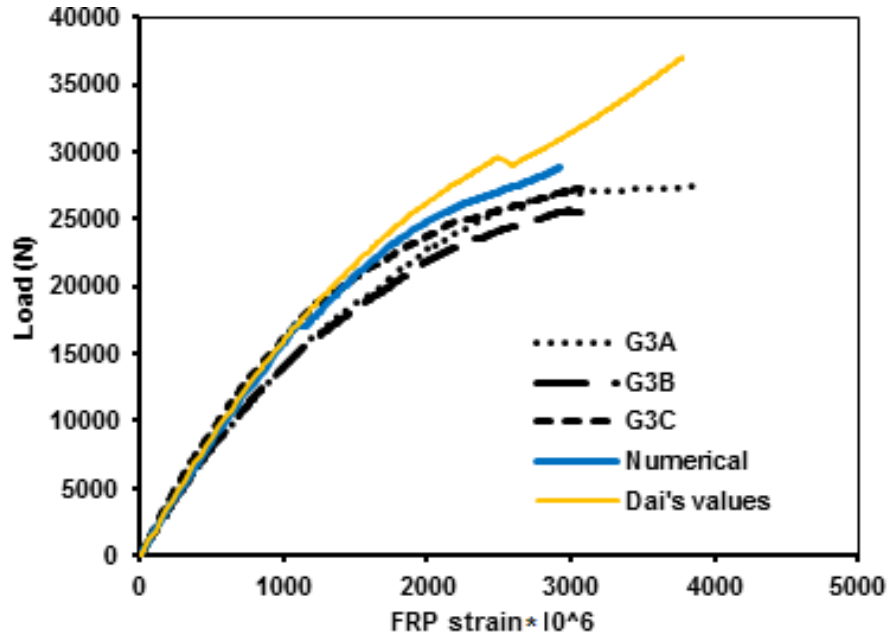
Figure 4.22 Load vs. FRP strain curves for specimen G3

Figure 4.23 shows the numerical and experimental load vs. FRP strain curves. XFEM method is able to predict the trends of specimen behaviors, and maximum loads with mean percentage errors within 5.6-12%. Figure 4.24 presents the crack initiation and the debonding failure propagation obtained from the numerical analysis for specimen G1. The debonding starts in the first element of the damaged band adjacent to the FRP/concrete interface at the tip of notch (Figure 4.24a). As element stresses meet the initiation criterion (Equation 4.9), the crack propagates toward the support (Figure 4.24b).

(a)

(b)

(c)
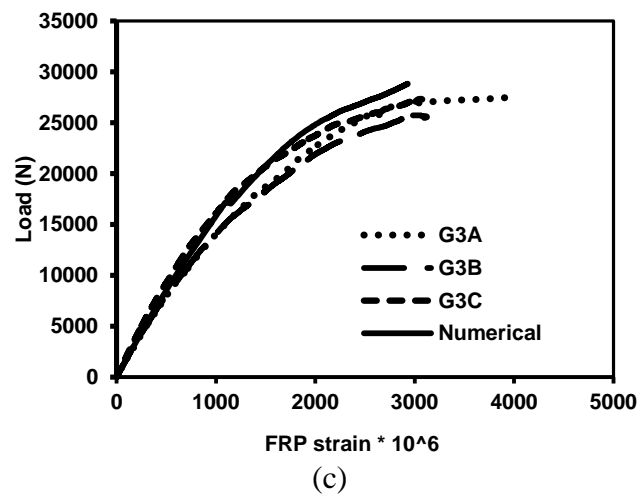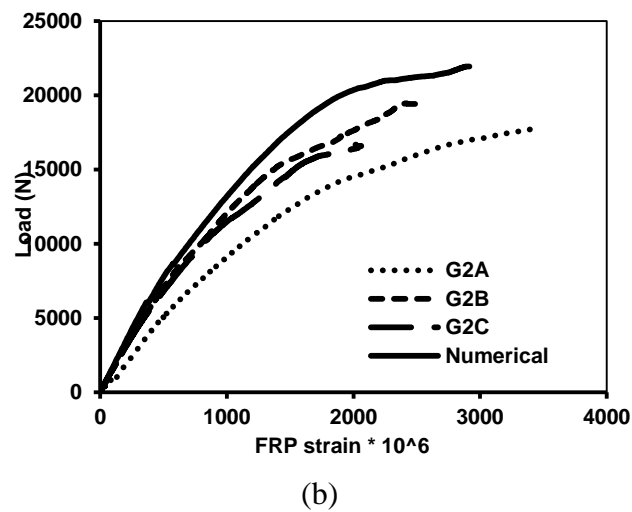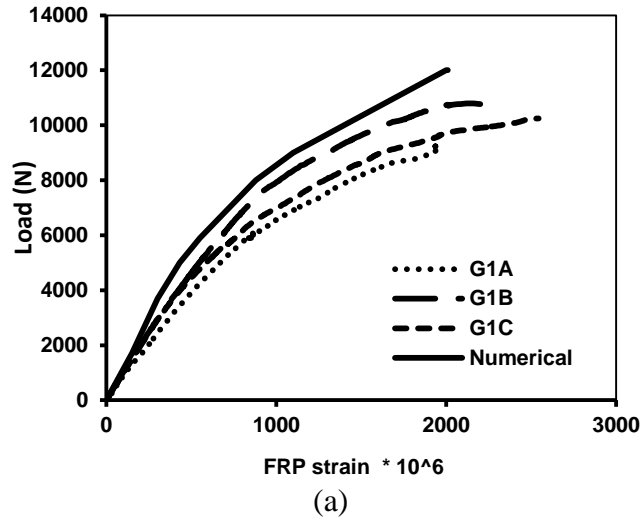
Figure 4.23 Experimental and numerical load vs. FRP strain curves for beam specimens tested by Harries et al. (2012)
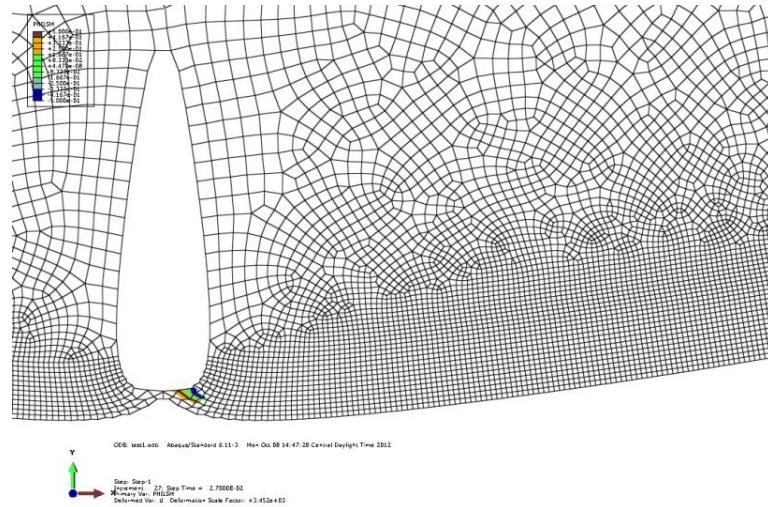
(a)
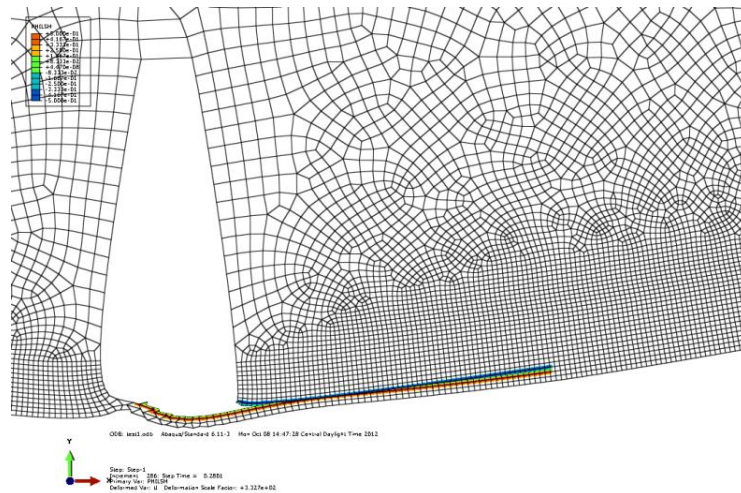
(b)

Figure 4.24 (a) Crack initiation, (b) Crack propagation

4.3.2 Sensitivity Analysis to the Damage Band Parameters

Since the debonding failure typically controls the behavior of FRP-strengthened specimens, the damage band geometry and properties play an important role in the predicted failure behavior. In this part of the study, the thickness and properties of the

damage band are varied to study their effects on the modeling of the FRP debonding from concrete in specimen G3.

The first sensitivity analysis investigates the effects of the mode I properties on the debonding failure of the beam specimens. Figure 4.25 presents the results of analyses with different normal bond strength, σ_n, and mode I critical fracture energy, G_{IC}. As it can be seen, the numerical models are insensitive to the mode I properties even when they are reduced 50%. It can be concluded that the mode I contribution does not have significant effect on the debonding failure initiated at the tip of the notch when the notch is placed at the middle of the beam span.
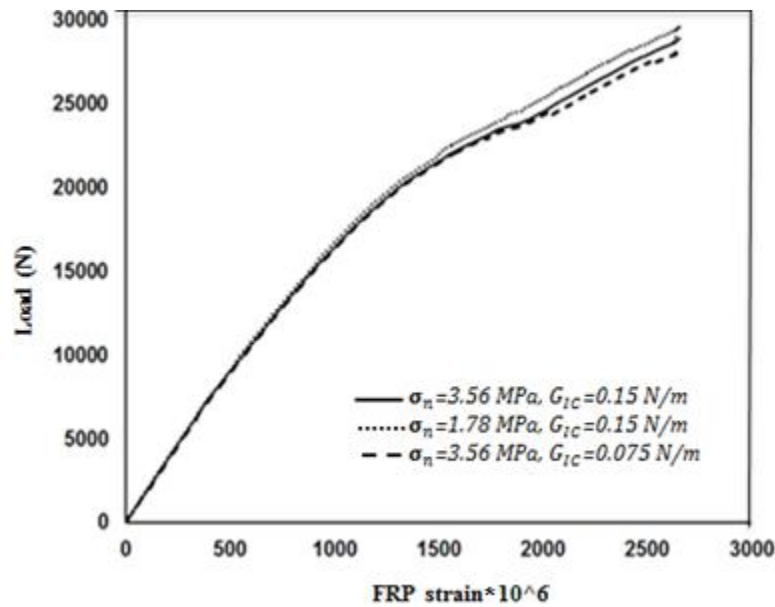
Figure 4.25 Sensitivity to the normal (mode I) properties

Figure 4.26 shows the sensitivity of the analyses to the mode II properties. The shear bond strength, τ_s, and the mode II critical fracture energy, G_{IIC}, are each changed 50%. As seen in the figure, mode II properties have a significant effect on the debonding behavior and the results are very sensitive to these parameters. The ultimate load changes

significantly (around 25%) when τ_s and G_{IIC} are changed. Therefore, the FRP debonding initiated at the tip of a mid-span flexural crack is primarily controlled by mode II or shear properties. This also validates the test method proposed by Harries et al. (2012), which intends to test the FRP debonding due to mode II (in-plane shear) loading.
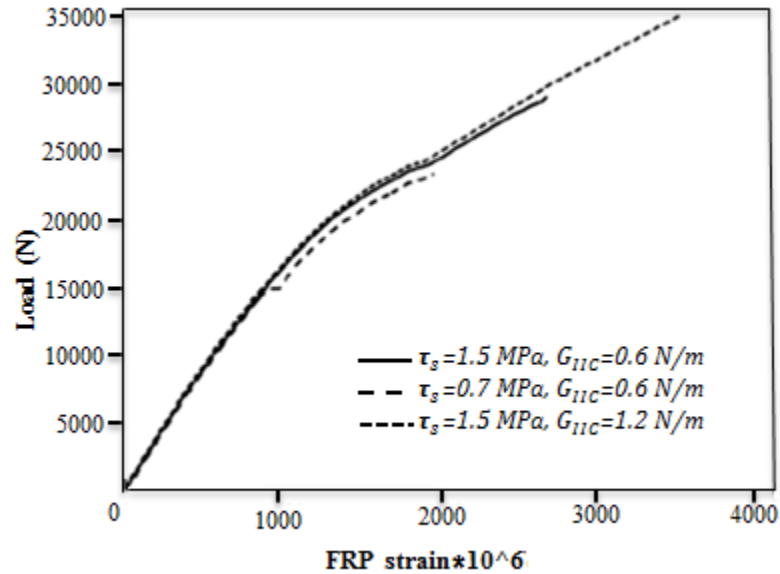
Figure 4.26 Sensitivity to the shear (mode II) properties

For the sensitivity analysis of the numerical results to the damage band thickness, the finite element analysis is conducted with damage band thicknesses of 2, 4, and 10 *mm*. Numerically obtained load versus mid-span FRP strain curves are shown in Figure 4.27. When the damage band thickness is increased from 2 to 10 *mm* (changed 500%), the decrease of the ultimate load is less than 10%. So the ultimate load is not very sensitive to the damage band thickness. However, a smaller damage band thickness results in stiffer behavior. The damage band thickness of 10 *mm* gives the poorest prediction in comparison with the stiffness of the experimental curves; the results for 2 and 4 *mm* thicknesses are close to each other. This observation is compatible with the

experimental observations that indicate the debonding and horizontal cracking generally occur within concrete at 1 to 5 *mm* from the FRP/concrete interface.
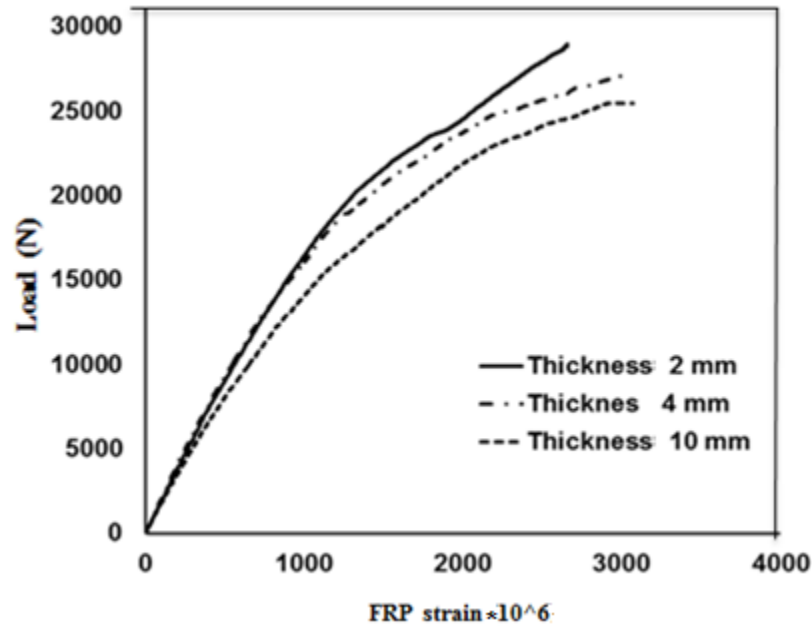
Figure 4.27 Sensitivity to the damage band thickness

4.3.3 Conclusion of Application XFEM-based Cohesive Method to Model IC Debonding Failure

XFEM-based cohesive method is successfully applied to model FRP debonding from a notched concrete beam. This method results in a good agreement between numerical prediction and experimental observations. According to the sensitivity analysis, the shear (mode II) properties of the damage band including shear strength and critical fracture energy controls the FRP debonding initiated at the mid-span notch.

As discussed in Section 4.3.1, the numerical analyses using smaller the bond strength and fracture energy values than those proposed by Dai et al. (2005) and Lu et al. (2005) give the good agreements with the experimental results. Since those proposed

values are obtained by equations that are found from single shear pullout tests, the

question raised is: ***Can the bond-slip behavior obtained from pullout tests be applied to***

beams to model IC debonding failure? To answer this question, both single shear pullout

and beam tests are performed following this study to investigate the bond–slip behaviors

of FRP bonded concrete specimens. These tests and related FE analyses are discussed in

detail in Chapters 5 and 6.

Chapter 5 Single Shear Pullout Test

The bond between the externally bonded FRP and the concrete substrate plays a key role in the performance of concrete structures after strengthening. In order to assess the bond mechanisms quantitatively, and to numerically simulate the FRP-strengthened concrete beams, defining an accurate bond-slip relationship is an important, but controversial issue. The conventional method of finding the bond-slip behavior of the interface is the single shear pullout test. In this method, a tensile force is applied to the FRP plate along the FRP/concrete interface. The bond-slip behavior is obtained by using the FRP axial strain distributions along the FRP plate.

In this chapter, six specimens are tested to find the bond-slip behavior of the FRP/concrete interface in the single shear pullout test. The test set-up, concrete mixture and its properties, and the FRP properties and bonding procedures are explained in detail. The numerical analysis using concrete damaged plasticity model in XFEM is performed for the FRP debonding modeling and verified by the experimental results. A sensitivity analysis of the boundary condition is also studied.

5.1 Single Shear Pullout Test Set-up

Since the main purpose of carrying out the pullout test in this part of this study is to compare the bond-slip behavior of pullout specimens to the bond-slip behavior of FRP-strengthened beam specimens, the pullout specimens are considered as half of the beam specimens both in dimensions and boundary conditions. The beam test specimens that will be explained in the next chapter and the pullout specimens are shown in Figure

5.1 for the comparison. As shown in the figure, the length of the concrete block and the FRP plate of the pullout specimen are half of the beam length and the bonded FRP plate length in the beam specimen, respectively. The cross section of the concrete substrate and FRP width are same in both specimens. In the beam specimens, a half-depth notch is located at mid-span to simulate the flexural crack. To mimic the same boundary conditions of beam specimens in the pullout specimens, the concrete block is positioned on a rigid frame with two steel reaction elements as shown in Figure 5.1b. Element A provides the horizontal reactions to simulate the uncracked part of the beam at the top of the notch, and element B provides the vertical reactions to simulate the support forces in the beam specimens. A 25 *mm* pre-crack between FRP and concrete is provided in both groups of specimens.

(a)   (b)
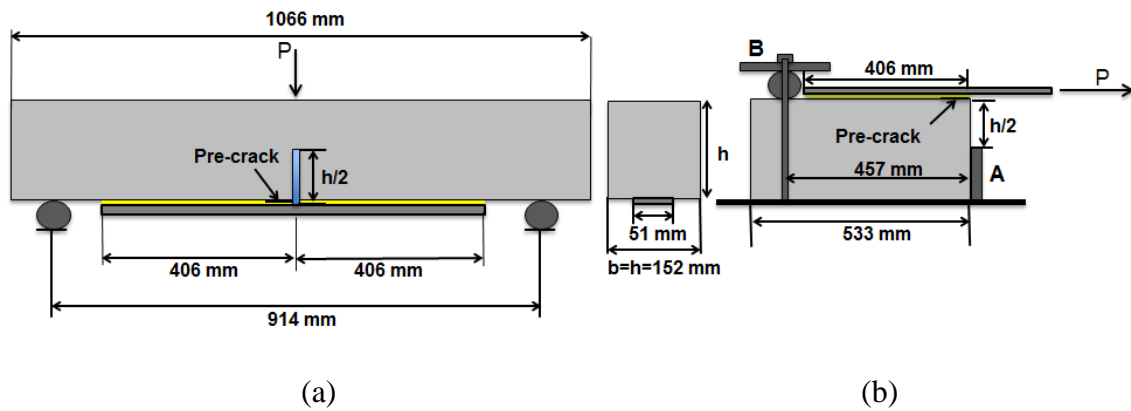
Figure 5.1 Experimental specimens: (a) beam specimens, (b) pullout specimens

The pullout test is conducted under displacement control with loading rate of 0.0127 *mm /s*. To impose the tensile stresses to the FRP plates, the hydraulic single ended actuator (model 201.20T) from Minnesota Testing Systems (MTS) Company is used.

Figure 5.2 shows the schematic of the test set-up (All dimensions are in

millimeter). In this figure, parts 1 and 2 are HSS $254 \times 203 \times 9.5$ (mm) and HSS

$203 \times 254 \times 9.5$ (mm), respectively. These two steel channels are fixed to the strong

floor by bolts. Part 3 is designed in a way to fill the room between the two channels to

prevent their movements relative to each other and also provides an adjustable height for

the FRP plate. It is inevitable to have some variations of concrete block height and

adhesive thickness among different specimens. Although these variations are very small,

they may cause the line of the action of applied tension force to not coincide with the

center of the FRP in horizontal direction. For this reason, two small wheels sitting on

thread bars are used to adjust the height of steel plates that hold the FRP plate in order to

have tension force direction as close as possible to the center of the horizontal FRP plate.

They also support the steel plates to reduce the bending in the FRP plate due to the

weight of the steel plates. The wheels are used in order to generate the least friction force

against steel plate's horizontal movement during testing. In order to impose uniform

tensile force to the FRP plate, same toque forces of 81 *KN-mm* are applied to four bolts to

bolt the two steel plates holding the FRP plate. To reduce the probability of uneven toque

on bolts, 27 *KN-mm* toque is applied to each bolt in the sequence of diagonal pattern (i.e.,

after one bolt is applied torque, the bolt diagonal to the first bolt is applied the torque)

and the torque on each bolt is increased to 81 *KN-mm* in the same sequence. The surfaces

of the steel plates are roughed to prevent the sliding of the FRP plate during the test as

shown in Figure 5.2. Figure 5.3 shows a picture of the whole set-up.
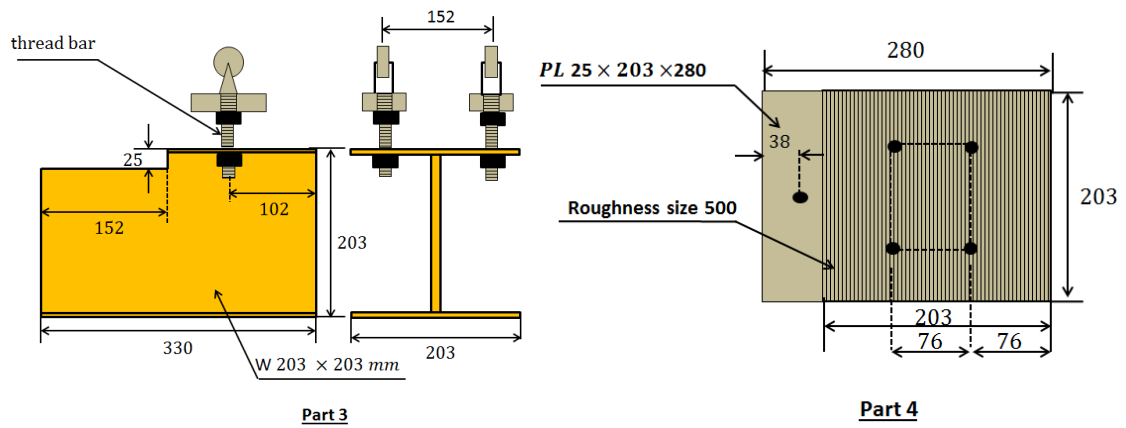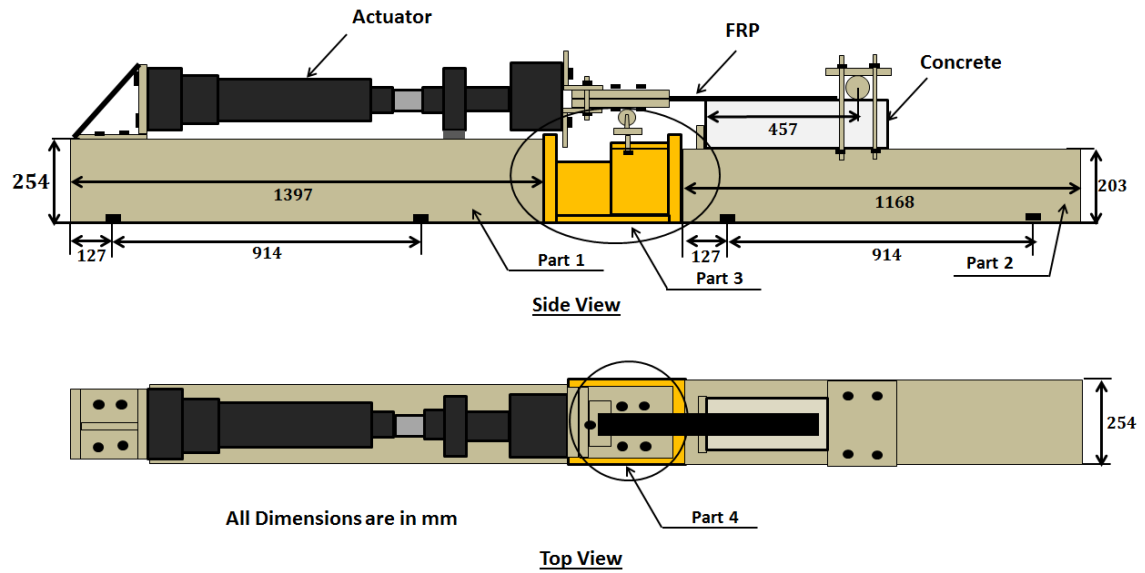
Figure 5.2 Schematics of pullout test set-up

Figure 5.3 Shear pullout test set-up

5.2 Concrete Mixture for Pullout Specimens

Concrete compressive strength at 28 days, f_c', of 31 *MPa* is the design target. The absolute volume method is used to find the mixture proportioning (Kosmatka et al. 2002). The proportions of water, cement, coarse and fine aggregates, and air content per cubic meter of concrete are presented in Table 5.1. The water to cement ratio is calculated based on the standard using compressive strength value and is equal to 0.44.

Table 5.1 Proportions of concrete mixture per cubic meter

Water (*kg*)	128
Cement (*kg*)	279
Coarse aggregate (*kg*)	887
Fine aggregate (*kg*)	478
Air-entraining admixture (*g*)	164

Two mix batches are used for concrete mixing regarding to applied mixer volume (Figure 5.4a). Plastic forms are used for concrete casting (Figure 5.4b). Also cylinder specimens are prepared to test the compressive strength (Figure 5.4c). For each batch of concrete, three cylinders are prepared and they are named as M1-1 to M1-3 and M2-1 to M2-3. Three cylinders are tested at the same time of the pullout specimens and the other three are cured in water for testing at 28 days. The slump tests are done during the mixing processes in order to obtain 100 ± 20 *mm* slump (Figure 5.4d). After removing the forms, the specimens are cured for one week in the lab environment while covered by plastics (Figure 5.4e)

(a)
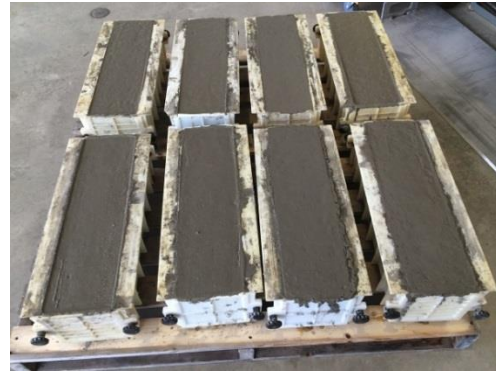
(b)

(c)

(d)

(e)

Figure 5.4 Preparation processes of concrete specimens for pullout test

5.3 Strengthening System

The surface of concrete to receive the FRP plate for strengthening must be sound and prepared for bonding by means of abrasive methods. Typically, light sandblasting,

grinding or other approved methods are acceptable. The surface should be free of protrusions or cavities. It is important to remove the laitance in the concrete and expose some of the concrete aggregate. This is achieved with mechanical grinders using a metal sander as shown in Figure 5.5a.

In this study, the strengthening system for shear pullout test is bonding of Tyfo® UC laminate strips by Tyfo® S (Saturate) epoxy as primer and Tyfo® TC (Tack Coat) epoxy as adhesive, from FYFE company, on the concrete substrate. The properties of the strengthening system components are presented in Table 5.2.

Table 5.2 Proportions of strengthening system components

Property	Tyfo® UC Laminate Strip	Tyfo® S	Tyfo® TC
Ultimate tensile strength (*MPa*)	2790	72.4	22.7
Elongation at break (%)	1.8	5	1.88
Tensile Modulus (*GPa*)	155	3.18	1.2
Layer Thickness (*mm*)	1.5	-	1

Tyfo® UC Laminate Strip is a high modulus, high tensile strength, pull-formed, epoxy-carbon composite. The Tyfo® S epoxy is a two-component epoxy matrix material used as primer in this study including component A and B. For bonding applications, 100 parts of component A should be mixed with 23.3 parts of component B by weight. Then it needs to be mixed thoroughly for five minutes with a low speed mixer at 400-600 *RPM* until uniformly blended (Figure 5.5b). Tyfo® TC epoxy is also a two-component material that is used as adhesive between CFRP and concrete. Mix ratio is 100 parts of component A to 34.5 parts of component B by weight. It is needed to be mixed in a way as Tyfo® S epoxy.

(a)

(b)
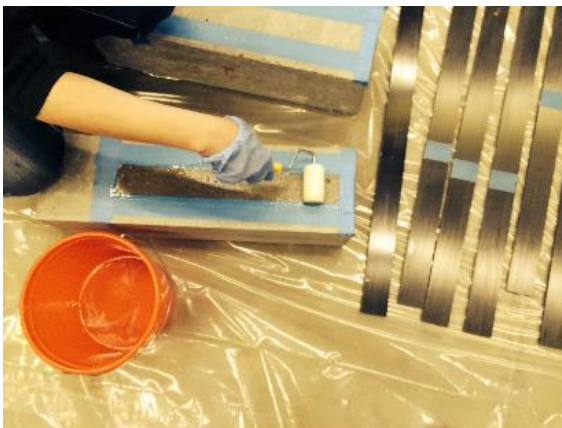
(c)

(d)

(e)

Figure 5.5 FRP application processes

A roller is used to apply a thin layer of primer to the concrete surface (Figure 5.5c). The strips should have the bonding face cleaned with acetone to remove any foreign debris. First, a thin prime coat of Tyfo S epoxy is applied to the CFRP strips and then, a thin layer of Tyfo® TC Epoxy adhesive is applied to the strip (Figure 5.5d). The FRP locations are marked by tapes on the concrete specimens. The tape is also used to provide 25 *mm* pre-cracks (unbonded areas between concrete and FRP). After placing the CFRP strips on the concrete surfaces (Figure 5.5e), the specimens are left to cure for a period of 7 days prior to testing.

5.4 Compressive Strength of Concrete Cylinders

The ASTM C39 (2010) standard method is used to find the compressive strength of concrete. This method consists of applying a compressive axial load to molded cylinders at a rate which is within a prescribed range until failure occurs. The compressive strength of the specimen is calculated by dividing the maximum load attained during the test by the cross-sectional area of the specimen.

The test machine used in this study is Forney compression testing machine as shown in Figure 5.6. The cylinders are 203 *mm* (8 *in*) in height and 102 mm (4 *in*) in diameter. The applied loading rate is 0.25 *MPa/s*. The recorded compressive strengths of cylinders (M1-1, M1-2, and M2-1) tested at the day of shear pullout tests, and the recorded strengths of cylinders (M1-3, M2-2, and M2-3) tested at 28 days after casting are presented in Table 5.3.

Figure 5.6 Forney compression testing machine

Table 5.3 Recorded compressive strengths for concrete cylinders

Cylinders	Age (days)	Compressive Strength (*MPa*)	Average Strength (*MPa*)	Standard Deviation (*MPa*)
M1-1		31.61		
M1-2	14	31.77	31.57	0.35
M2-1		31.27		
M1-3		32.41		
M2-2	28	32.23	32.93	0.87
M2-3		34.16		

5.5 Measurements in Shear Pullout Test

During the test, the applied load, FRP axial strains, and the slippage at the tip of pre-crack are recorded.

The objective of shear pullout test is to find the bond-slip relationship of the FRP/concrete interface. The conventional technique to find the bond-slip relation from shear pullout tests is using the FRP axial strains. However, it is difficult to apply this method because of the difficulty in arranging many gauges in a short effective load transfer length. The high scatter nature of local bond-slip relationships is another

difficulty that is faced. Principally, local bending of the FRP, whose bending stiffness is small, presents significant bending strains in FRP, and the coarse aggregates in the concrete surface layer are the causes of the scatter. Dai et al. (2005) proposed an indirect way to get the bond-slip behavior from shear pullout tests. In this method, there is no necessity to record the strain distribution along the FRP plate/sheet. The local interfacial bond-slip models can be obtained from the relationships between the FRP strain and slip at the tip of pre-crack as indicated in Equation 5.1:

$$\varepsilon_f = A \left(1 - e^{-B\delta}\right) \tag{5.1}$$

After determining the values of parameters A and B from experimental data, the interfacial fracture energy (G_f) and the bond strength (τ_{max}) can be calculated by:

$$G_f = 0.5 A^2 E_f t_f \tag{5.2}$$

$$\tau_{max} = 0.5 B G_f \tag{5.3}$$

where t_f and E_f are the thickness and Young's modulus of FRP plate, respectively.

In this study, both conventional method and Dai's method are used to find the bond-slip behavior of the FRP/concrete interface. The FRP strains are obtained by attaching strain gauges along the FRP plates. A digital dial gauge is used to measure the relative slip between the concrete and FRP at the pre-crack tip as shown in Figure 5.7.

Figure 5.7 Application of digital dial gauge to obtain the slip at the pre-crack tip

5.6 Experimental Observations of Shear Pullout Tests

Six concrete specimens are used for shear pullout test (CS1-CS6). The numbers of applied strain gauges, ultimate bearing load, and the failure type of specimens are presented in Table 5.4. All specimens have one strain gauge at the tip of pre-crack. Specimens CS2 and CS3 have one more strain gauge 51 *mm* from the pre-crack tip. Specimens CS4, CS5, and CS6 have three more strain gauges that are attached in 51 *mm* intervals from each other (Figure 5.7). After here, strain 1 presents the values obtained by strain gauge at the tip of pre-crack, and strain 2, 3 and 4 present the values obtained by other strain gauges attached on the FRP surface successively.

Table 5.4 Number of strain gauges, ultimate load, and the failure type of pullout specimens

Specimens	Number of strain gages	Ultimate load (*KN*)	Failure type
CS1	1	36.25	Flexural*
CS2	2	41.51	shear
CS3	2	26.92	shear
CS4	4	38.89	Flexural*
CS5	4	45.60	shear
CS6	4	47.65	shear

* "flexural" failure means its failure mode is similar to that in beam specimens. Detail explanation is presented on page 99.

As it can be seen in the table, CS3 has the lowest ultimate bearing load. During the test for CS3, it was seen that the FRP plate level is lower than holding steel plate's level as shown in Figure 5.8, schematically. It causes some peeling loads on the FRP that makes the debonding easier and faster, and in result the ultimate bearing load is less than the others. The second strain gauge that is attached 51 *mm* away from the pre-crack tip (strain2) shows some negative strains during the testing as shown in Figure 5.9. It confirms that the FRP plate is subjected to a peeling force that causes a positive moment and as a result, compressive stresses on the FRP surface. This specimen is not used for

the calculation of the bond-slip relationship.
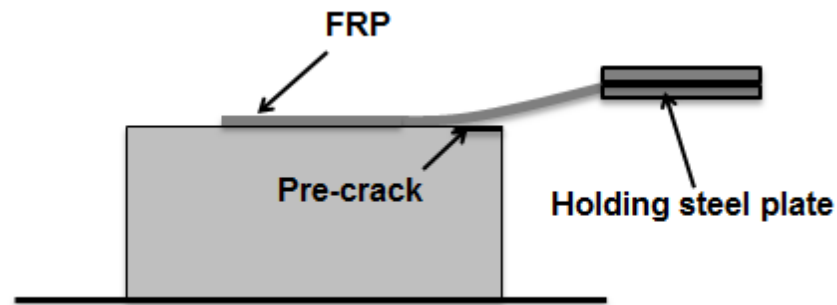
Figure 5.8 Schematic of specimen CS3 during pullout test
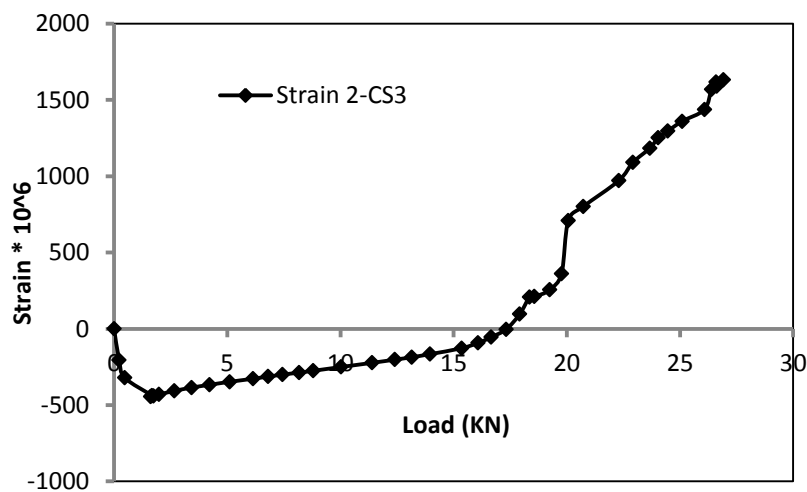
Figure 5.9 Strain 2 vs. load curve for specimen CS3

CS1 and CS4 have the similar failure types. The failures are shown in Figure 5.10. This failure is very similar to those happened in the beam specimens subjected to bending load which will be described and discussed in the next chapter. Therefore, this failure is called flexural failure in this study. For these specimens, the main failure cracks are diagonal cracks that occurred in concrete as shown in the figure. Therefore, the debonding does not start at the tip of pre-crack.

(a)   (b)

Figure 5.10 Flexural failures: (a) CS1, (b) CS4

Figure 5.11a compares the FRP strain at the tip of pre-crack (strain 1) for specimen CS4 with flexural failure to that for specimen CS5 with shear failure. As it can be seen, the strains and loads are almost identical at the beginning stage of the loading. However, strain 1 in CS5 increases much faster than that in CS4. Since in CS4 the debonding does not start at the tip of pre-crack, the maximum strain 1 value is very small compared to that in CS5. On the other hand, the strains 2 in CS4 are comparable with strains 2 in CS5 (Figure 5.11b). In beam specimens, the FRP plate at the tip of flexural/shear crack is subjected to local bending load (explained in Chapter 6) that causes a failure similar to the flexural failure in these specimens. Thus, it seems that the FRP plate in CS4 and CS5 is subjected to a certain level of bending load during testing. It means that the steel plate's level (loading level) is lower than the FRP plate's level during the tests for these two specimens. Because the debonding failures in specimens CS1 and CS4 do not follow the typical shear failure, they are not applied to calculate the bond-slip behavior from the pullout test.
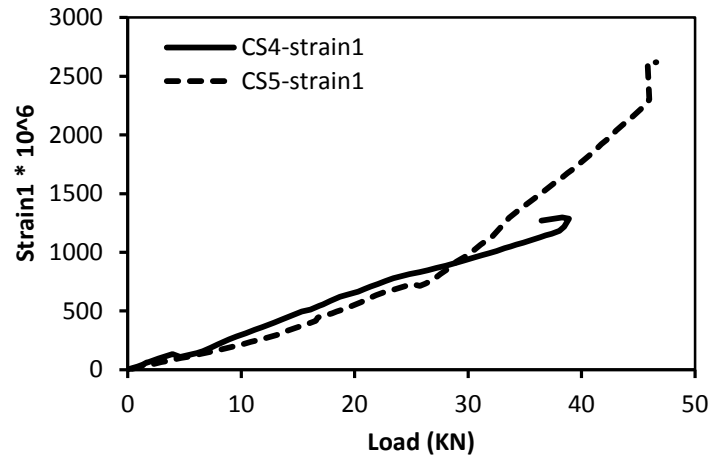
(a)
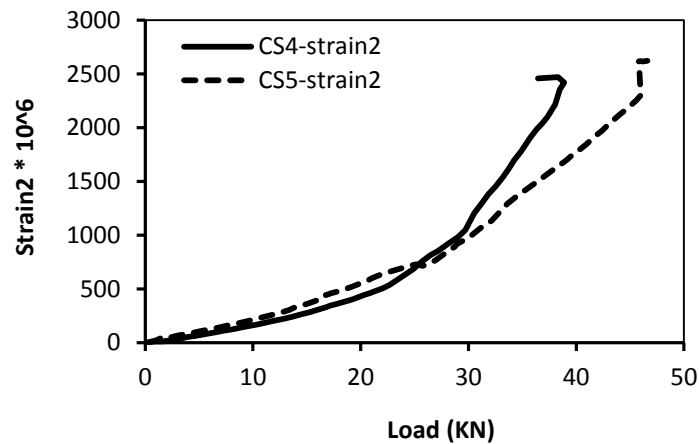
(b)

Figure 5.11 Comparison between CS4 and CS5: (a) strain 1, (b) strain 2

The failure type of Specimens CS2, CS5, and CS6 is shear failure as shown in Figure 5.12. However, for specimen CS2, a diagonal crack is seen on the concrete surface as shown in Figure 5.12a. Its shape is similar to those in CS1 and CS4. So there is some flexural effect in CS2. It also can be seen in Table 5.4 that the ultimate load of specimen CS2 is a little less than those of specimens CS5 and CS6.
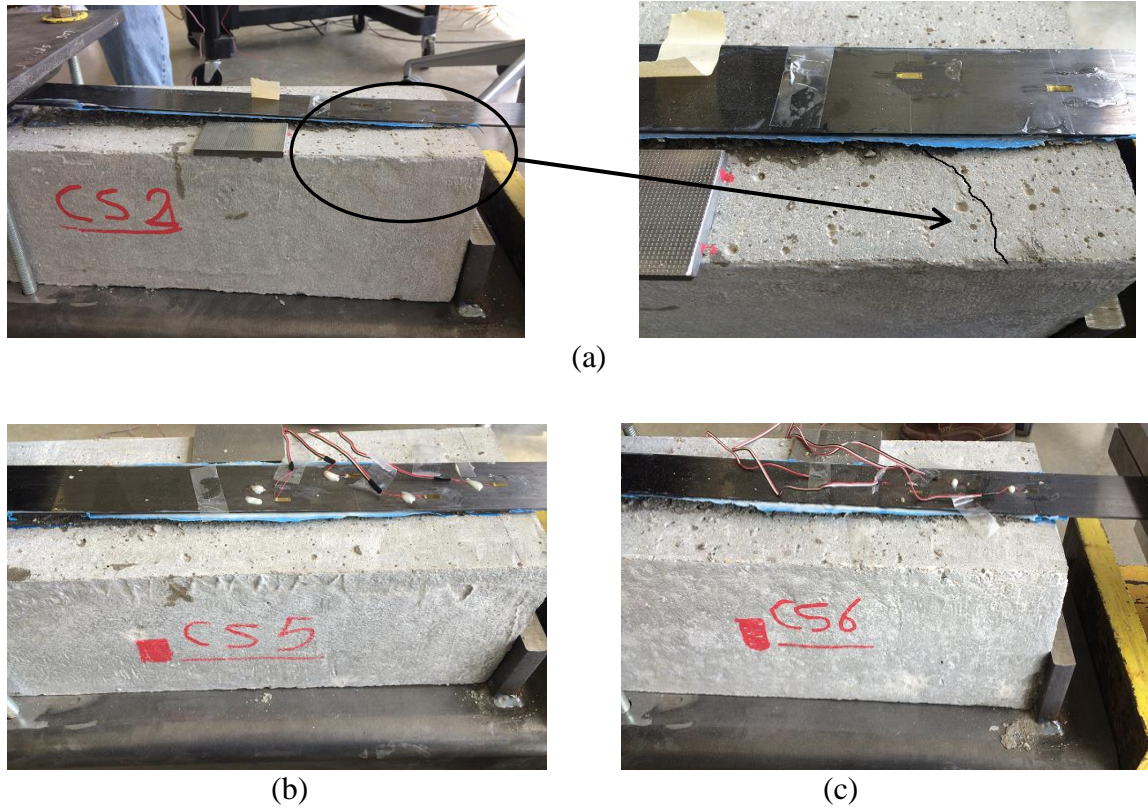
Figure 5.12 Shear failures: (a) CS2, (b) CS5, and (c) CS6

5.7 Bond-Slip Relationships of Pullout Specimens

Two methods are used to find the bond-slip relationships from pullout tests: conventional method, and Dai's method. In the conventional method, the bond-slip relationship can be calculated by Equations 2.1 and 2.2 using FRP axial strains along the FRP surface. Only four strain gages are attached on the FRP. Using recorded strains by these four strain gauges and Equations 2.1 and 2.2, the bond-slip curves are calculated and presented in Figure 5.13 for specimens CS2, CS5, and CS6.

In Dai's method, the FRP strain vs. slip curve at the tip of pre-crack is required to be attained by experiments. The obtained curves in this study are presented in Figure 5.14. The regression is done for function $\varepsilon_f = A(1 - e^{-B\delta})$ to find parameters A, and B

experimentally. The acquired values for A and B are presented in the Table 5.5. Then,

parameters A and B are used in Equations 5.2 and 5.3 to find the bond strength, τ_{max}, and

the interfacial fracture energy, G_f, that are shown in Table 5.5. The values of τ_{max} and G_f

gained by conventional method are also presented in the table for the comparison of two

methods. The values from both methods are similar while the results of conventional

method are less than those of Dai's method. However, since there are only four strain

records for each specimen, the values obtained by the conventional method are not

reliable. Therefore, values from Dai's method are used in the numerical analysis.
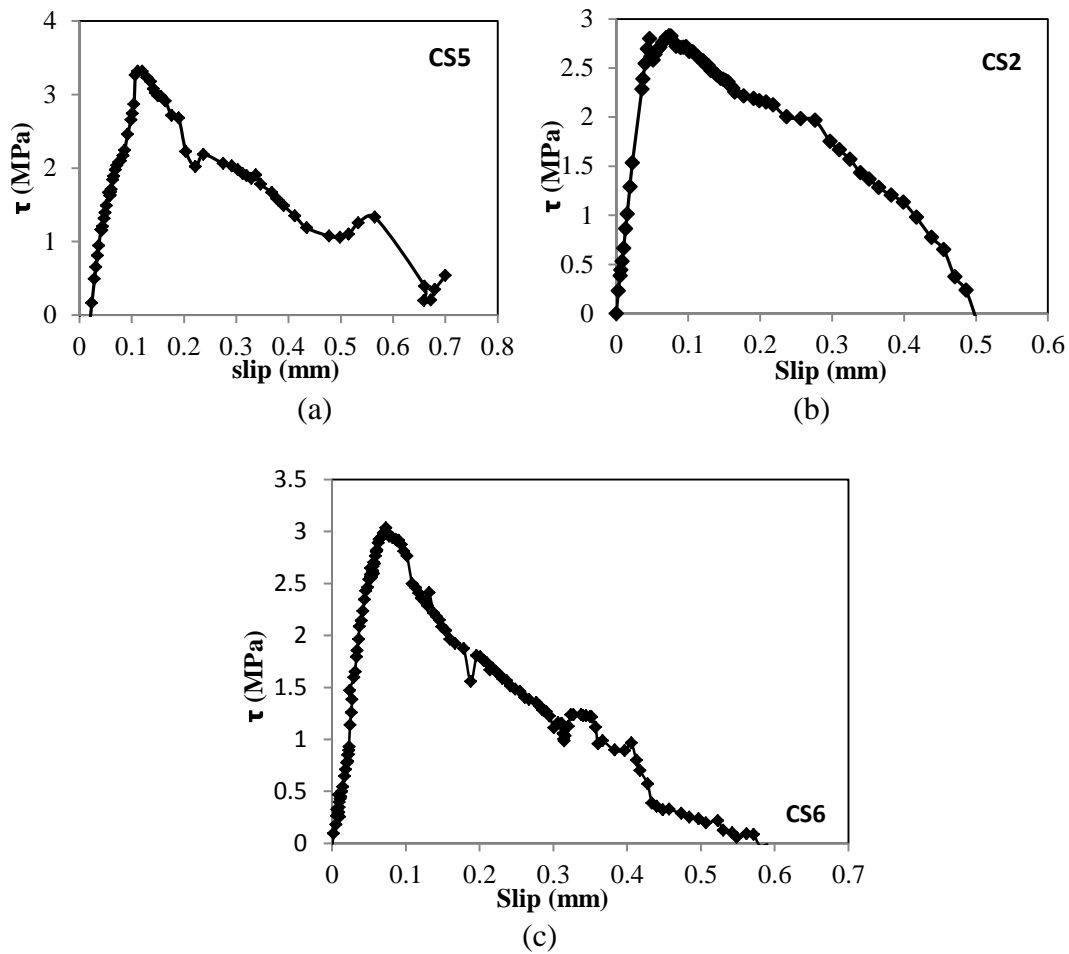
Figure 5.13 Bond-slip curves for specimens: (a) CS2, (b) CS5, and (c) CS6

(a)

(b)

(c)
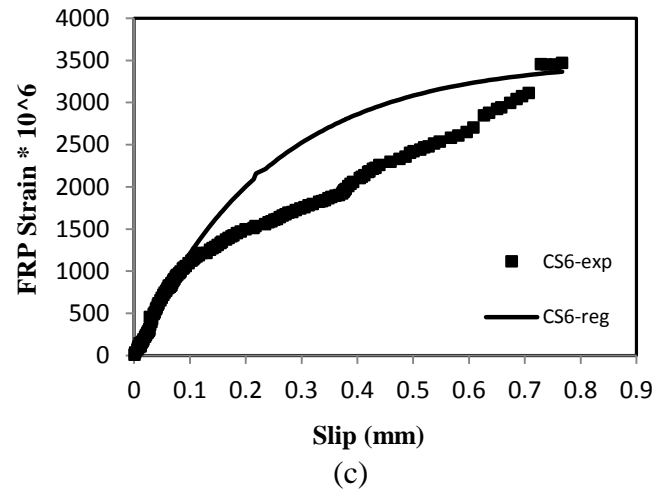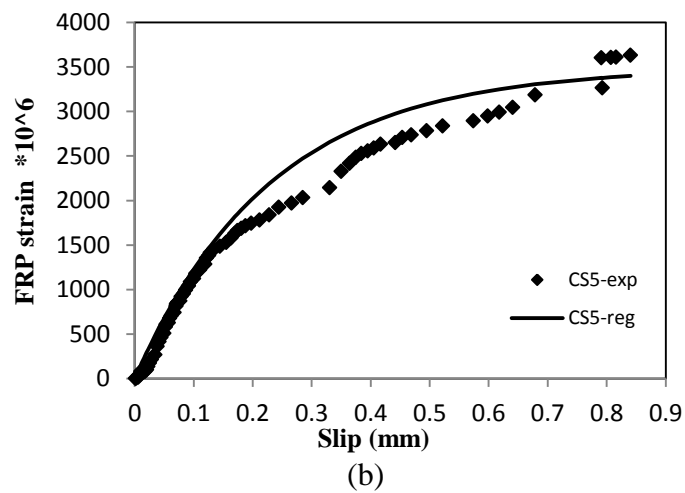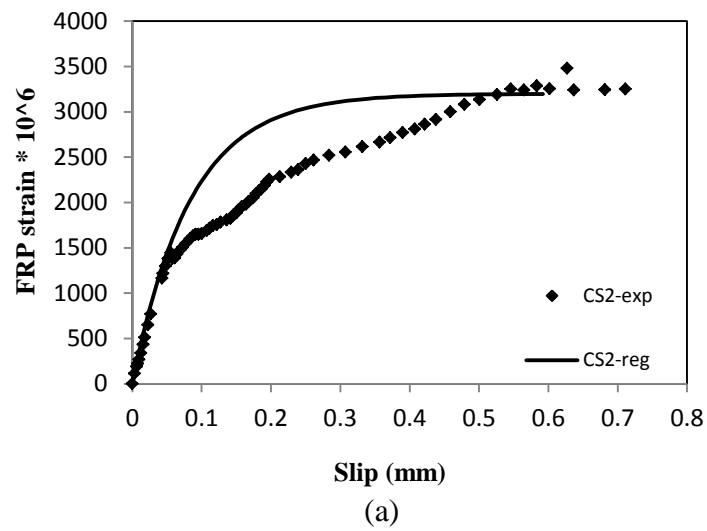
Figure 5.14 FRP strain vs. slip curve at the tip of pre-crack of specimens: (a) CS2, (b) CS5, and (c) CS6

Table 5.5 Values of τ_{max} and G_f obtained by Dai's method and conventional method

Specimen	A ε	B mm^{-1}	$\tau_{max}(MPa)$ Dai	G_f (N/mm) Dai	τ_{max} (MPa) conventional	G_f (N/mm) conventional
CS2	0.00320	5.1	3.03	1.19	2.81	0.70
CS5	0.00349	5.2	3.68	1.41	3.26	1.07
CS6	0.00350	5.1	3.63	1.42	2.95	0.84

CS2 has less bond strength and fracture energy compared to CS4, and CS5. The reason is the diagonal cracking in concrete discussed in previous section, which may cause less FRP strain at the tip of the pre-crack. Therefore, the average values of τ_{max} and G_f of CS5 and CS6 results obtained by Dai's method are used for the following numerical analysis.

5.8 Numerical Analysis of Single Shear Pullout Test

For the FE analysis, the commercial software ABAQUS 6.13 is used. Plane stress elements are applied for the model. Typical finite element mesh is shown in Figure 5.15. Concrete damaged plasticity model is applied in XFEM for the modeling of concrete. Concrete plasticity model is well known method to model the concrete, but it is not able to show the cracking. By application of this method in XFEM instead regular FE method, it is possible to take benefit from concrete damage plasticity and cracking modeling together. The crack initiation criterion is the maximum principal stress criterion, in which a crack is initiated if the maximum principal tensile stress reaches the concrete tensile strength. The crack propagates perpendicular to the direction of the maximum principal tensile stress. The evolution of the crack is governed by the fracture energy, which represents the tension-softening behavior of the concrete during cracking. A linear tension-softening curve is assumed for the concrete. FRP and epoxy is modeled using a

brittle cracking model. The thicknesses of FRP plate and epoxy are 1.5 mm and 1 mm, respectively.

A damage band is introduced at the tip of pre-crack with thickness 2 mm as shown in Figure 5.15. A bilinear traction-separation law is assigned to the damage band. Bond strength, $\tau_{max} = 3.655\ MPa$, and interfacial fracture energy, $G_f = 1.415\ N/mm$, are assumed according to the findings of experiments (average of CS5 and CS6 results obtained by Dai's method). The Young's modulus of the damage band is equal to the Young's modulus of concrete. However, the shear modulus of the damage band is calculated by Equations 4.10, which is much smaller than the shear modulus of concrete. A summary of applied material properties in the FE analysis is presented in Table 5.6.
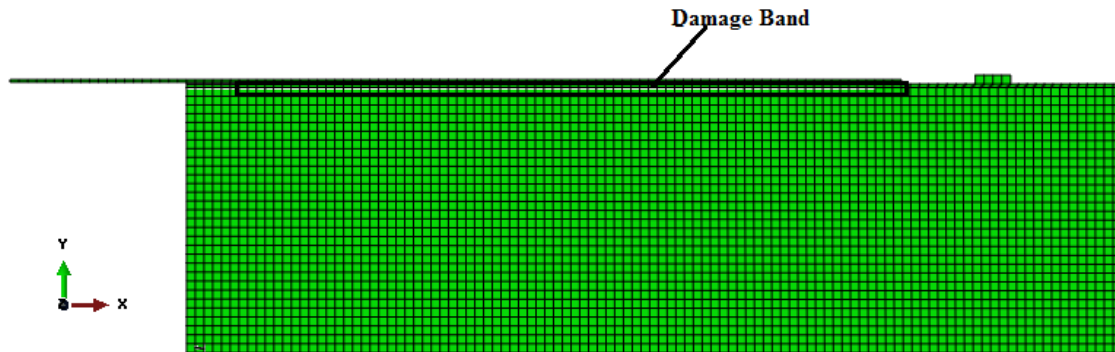
Figure 5.15 Typical FE mesh applied for analysis of shear pullout test specimens

Table 5.6 Material properties applied in FE analysis of shear pullout test specimens

Properties	Concrete	Damage Band	FRP	Epoxy
Modulus of Elasticity, E (GPa)	30.5	30.5	155	1.2
Tensile Strength, (MPa)	3.58	3.58	2790	22.7
Compressive Strength, $f_c^{'}$, (MPa)	33.09	-	-	-
Shear Modulus, G, (GPa)	12.71	1.29	-	-
Shear Strength, τ_{max}, (MPa)	-	3.655	-	-
Fracture Energy, G_f, (N/mm)	0.12	1.415	-	-
Poisson Ratio	0.2	0.2	0.25	0.3

5.8.1 Results of FE Analysis of Single Shear Pullout Test

The used FE analysis is able to predict the FRP debonding from concrete substrate. The red color in Figure 5.16 shows the debonding cracks in the model. There is a very good agreement between numerical and experimental results for FRP strain vs. slip curves at the tip of pre-crack as shown in Figure 5.17. The predicted ultimate load by numerical analysis is 45.59 *KN* that is compatible by experimental ultimate loads presented in Table 5.4 for specimens CS5 and CS6. The mean parentage error of the ultimate load is 2.17%.
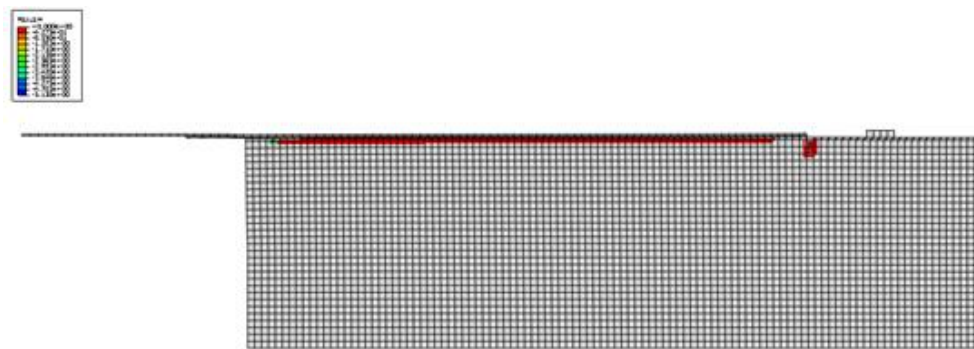
Figure 5.16 FRP debonding failure predicted by FE analysis
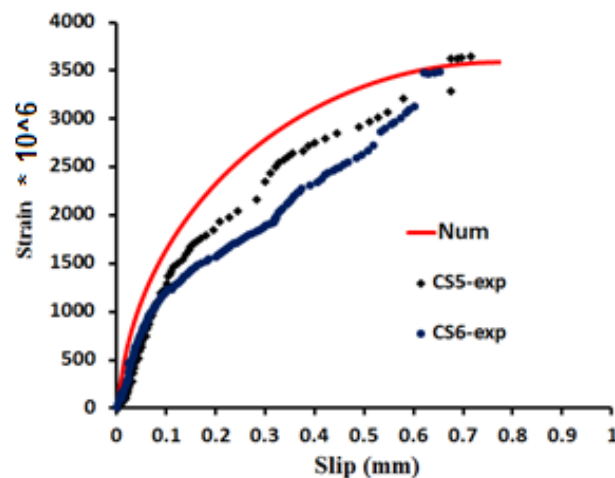
Figure 5.17 Numerical and experimental FRP strain vs. slip curves at the tip of pre-crack

5.8.2 Sensitivity Analysis to the Boundary Conditions

Table 5.7 presents the bond strength, τ_{max}, and the interfacial fracture energy, G_f, obtained using the analytical equations proposed by Dai et al. (2005) (Equations 2.3a to c) and Lu et al. (2005) (Equation 2.4a to c). By comparison between these values and experimental ones, it can be seen that the analytical equations predict much higher bond strength.

Table 5.7 Predicted values for bond-slip characteristics

Model	τ_{max} (MPa)	G_f (N/mm)
Dai et al. (2005)	6.47	1.58
Lu et al. (2005)	5.92	0.705
Experiments	3.655	1.415

As mentioned previously, the main objective of carrying out the shear pullout test in this study is to compare the obtained bond-slip relationship of shear specimens to the bond-slip relationship of the FRP-strengthened concrete beam specimens which will be discussed in the next chapter. Therefore, the boundary conditions of the shear test are set to simulate the boundary conditions in the half of a FRP-strengthened concrete beam with a mid-span half-height notch. In the following, the effect of the boundary condition of the pullout test on the bond-slip relationship is studied numerically.

It is observed in the literature that the FRP/concrete interface is not under pure shear stresses in single shear pullout tests (Lu et al. 2005, Baky et al. 2012, Toutanji et al. 2013). The normal stress components along the interface have a significant effect on the bond strength. The boundary conditions may cause different normal stresses in the concrete close to the interface. In order to study the sensitivity of the normal stress components of interface to the boundary conditions, four different boundary conditions

(Figure 5.18) are selected. Boundary condition *b* is the one used in experiments and numerical analysis in this research.

The normal stress, σ_x, which is in the longitudinal direction, of the element at the tip of pre-crack in concrete is presented in Figure 5.19 for four selected boundary conditions. The normal stresses in this figure are those in the model before the crack initiation criterion is met (starting of the debonding). The normal stress σ_x is sensitive to the boundary condition of concrete block at the load side. As the height of constraints are increasing at this side, the absolute values of σ_x are increasing as well. Normal stress along y direction, σ_y, which is perpendicular to the interface, is small compared to the normal stress along x direction, σ_x, and is negligible.
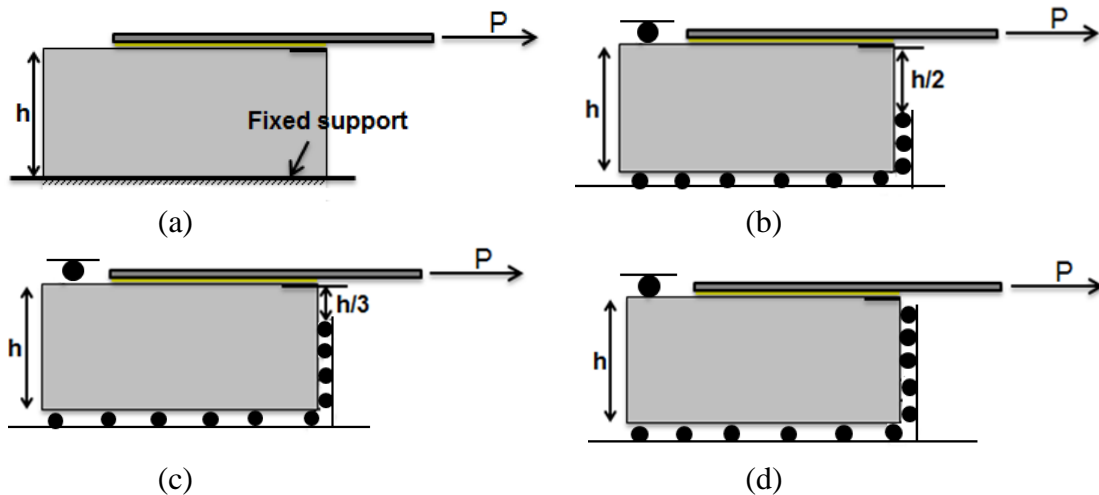
Figure 5.18 Sensitivity analysis to boundary conditions

Since the FRP debonding failure occurs in concrete close to the FRP/concrete interface, it is reasonable to express the bond strength as a function of concrete strength. The applied load at the end of the FRP plate is transmitted to the concrete substrate by shear stresses. Figure 5.20 shows the concrete substrate surface after FRP debonding. As

it can be seen, the debonding actually is initiated with concrete fracture. Thus, when the maximum principle stress in the element at the tip of pre-crack reaches to the concrete tensile strength, f_t, the crack initiates in the element. Based on this assumption and regarding that σ_y is negligible; the crack initiation criterion can be defined as:

$$f_t = \frac{\sigma_{x,max}}{2} \pm \sqrt{\left(\frac{\sigma_{x,max}}{2}\right)^2 + \tau_{max}^2} \tag{5.4}$$

Thus, the bond strength, τ_{max}, as a function of concrete tensile strength and the maximum normal stress component in the element can be expressed as:

$$\tau_{max} = \pm \sqrt{\left(f_t - \frac{\sigma_{x,max}}{2}\right)^2 - \left(\frac{\sigma_{x,max}}{2}\right)^2} \tag{5.5}$$
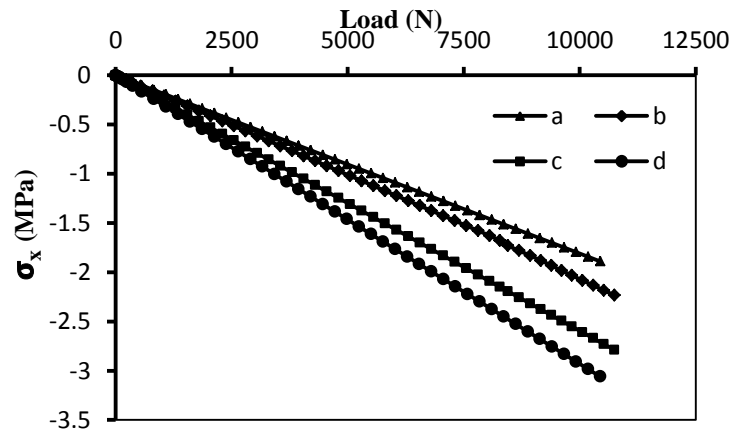
Figure 5.19 Normal stress σ_x vs. load of the element at the tip of pre-crack

Figure 5.20 Concrete substrate surface after FRP debonding in shear pullout test

Since $\sigma_{x,max}$ is compressive stress with negative sign (Figure 5.19), the bond strength, τ_{max}, increases with increasing of $\sigma_{x,max}$. In summary, changing the boundary conditions of concrete block results in changing the maximum normal stress of concrete, and therefore changing the measured bond strength. Because the beam specimens have a half height notch in the middle span, the boundary condition *b* in Figure 5.18 is appropriate for this study.

Chapter 6 Beam Test

One of the most common failure modes in FRP-strengthened concrete beams is caused by the opening of major flexural/shear cracks. In this type of failure, which is referred as intermediate crack (IC) debonding failure, the debonding initiates at the tip of the major flexural/shear crack and propagates toward the FRP plate end. In order to analyze the FRP debonding behavior of strengthened beams, the bond-slip relationship of the FRP/concrete interface is required. Although the conventional (direct) method to get the bond-slip relation is the single shear pullout test, the stress state of the concrete along the FRP/concrete interface in a beam may not be the same as that in a pull out test specimen. This is due to the difference of the loading types, boundary conditions, and deflections between the beam and the FRP/concrete joint specimens.

In order to study the bond behavior directly in FRP-strengthened beams, beam tests are carried out using FRP-strengthened concrete beam specimens with a mid-span notch. The notch represents a major flexural/shear crack that triggers IC debonding failure. To investigate the sensitivity of the bond-slip behavior to the location of the notch, the notch position in specimens is moved forward to the FRP plate end. Then, FE analysis is used to model IC debonding failure verified by the experimental results. Using numerical results, the stress state of the FRP/concrete interface is studied to compare the bond properties of strengthened beams and single shear pullout specimens.

The beam experiments were carried out by the collaboration of Marquette University and Watkins Haggert Structural Engineering Laboratory at the University of Pittsburgh under the supervision of Dr. Kent Harries.

6.1 Beam Test Set-up

The dimensions of beam test specimens with mid-span notch are shown in Figure 6.1a. The notch positions are changed every 51 *mm* from the mid-span to the support (Figure 6.1b). The notch serves as the major flexural/shear crack. The width of the notch is 5 *mm* and its height is half of the beam height (76 *mm*). A 25 *mm* pre-crack between FRP and concrete is provided to control the direction of the FRP debonding. The Instron® flexure fixture (model 600D) is used to apply flexural force in a mid-span three point bending test system. The test is conducted under displacement control. Figure 6.2 shows a picture of the whole set-up.

(a)

(b)
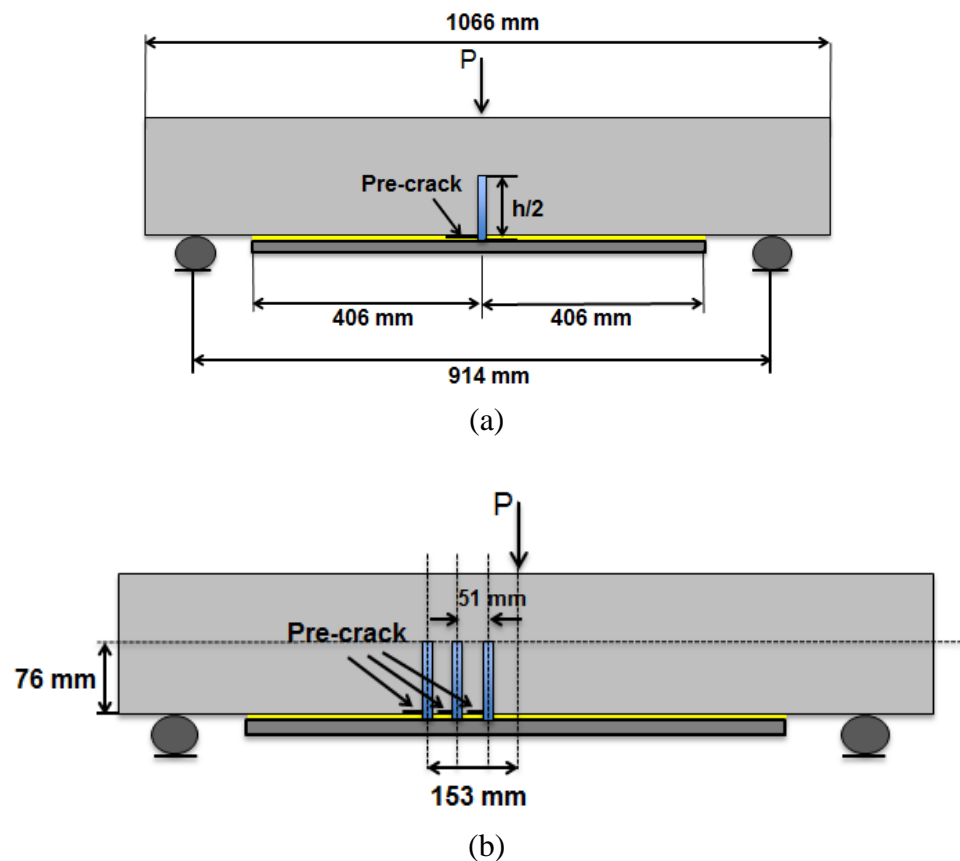
Figure 6.1 Beam specimen dimensions: (a) notch at mid-span, (b) notch at locations away from mid-span

Figure 6.2 Beam test set-up

6.2 FRP Application for Flexural Strengthening of Beam Specimens

The strengthening system for beam tests is bonding CFRP laminate strips by Sikadur ®-30 epoxy resin. The Young's modulus, ultimate tensile strength, thickness, and Poisson's ratio of the CFRP strips are 155 *GPa*, 2800 *MPa*, 1.5 *mm*, and 0.25, respectively. Sikadur ®-30 epoxy that is a two-component structural epoxy is used as the adhesive for the FRP bonding. The Young's modulus, ultimate tensile strength, thickness, and Poisson's ratio, of the epoxy are 4.48 *GPa*, 24.8 *MPa*, 1 *mm*, and 0.3, respectively.

Before FRP plates are bonded to the beams, notches are created by saw cutting (Figure 6.3a). The FRP application on the concrete surface is almost the same as that explained in Chapter 5 for the single shear pullout specimens. The surface roughness of concrete substrate is obtained by a grinder (Figure 6.3b). Then, water pressure is used to remove the loose particles (Figure 6.3c). The FRP layout locations are marked and a 25 *mm* wide tape is used to create the pre-crack at the tip of the notches (Figure 6.3d). The mix ratio of the two components of Sikadur ®-30 is 3:1 by weight. It is needed to be mixed thoroughly for three minutes with a low speed mixer at 400-600 *RPM* until

uniformly blended (Figure 6.3e). An approximately 1 *mm* coat of the epoxy is applied on the concrete surface and pre-cut strips of FRP (Figure 6.3f). After bonding the FRP strips, the specimens are left to cure for at least 14 days.

<table>
<tr><td>(a)</td><td>(b)</td></tr>
<tr><td>(c)</td><td>(d)</td></tr>
<tr><td>(e)</td><td>(f)</td></tr>
</table>

Figure 6.3 Beam specimen preparation

6.3 Concrete Properties of Beam Specimens

The concrete properties including compressive strength, Young's modulus, Poisson's ratio, and splitting tensile strength are obtained experimentally using cylinder specimens 203×102 *mm* (standard 8×4 *in*) by compression test (ASTM C39 2010) and splitting tensile test (ASTM C496 2010).

Six cylinder specimens (C1-C6) are used for the compression test. Sulphur capping is applied for the cylinder's top surfaces in order to have smooth, parallel, uniform bearing surfaces that are perpendicular to the applied axial load during compressive strength testing (Figure 6.4).

Figure 6.4 Sulphur capping for concrete cylinders

To experimentally calculate Poisson's ratio, ν, and Young's modulus, E, of the concrete, the cylinders are sited in a collar, which can measure the vertical and lateral displacement, before placing in the compression machine, in order to measure the lateral and longitudinal expansions during the loading (Figure 6.5). By having lateral and longitudinal expansions, the lateral and longitudinal strains can be calculated. The ratio of the lateral strains to the longitudinal strains is the Poisson's ratio. The ratio of

compressive stress to the longitudinal strain in linear range of the stress vs. strain curve is the Young's modulus. The experimentally obtained Poisson's ratio and Young's modulus of cylinders are presented in Table 6.1.

Table 6.1 Compression test results

Cylinders	Compressive Strength (*MPa*)	Poisson's Ratio (*v*)	Young's Modulus (*GPa*)
C1	30.81	0.195	24.270
C2	29.72	0.156	23.103
C3	27.75	0.251	23.294
C4	29.89	0.192	22.242
C5	34.37	0.266	25.144
C6	29.65	0.119	23.653
Average	30.37	0.197	23.618
Standard Deviation	2.01	0.051	0.914

Figure 6.5 Measurements of lateral and longitudinal expansions of cylinders

The splitting tensile strength of concrete, f_t, can be obtained experimentally by splitting test. The test consists of applying a compressive line load on a concrete cylinder placed with its axis horizontal between the compressive platens of the testing machine (Figure 6.6). Six cylinder specimens (S1-S6) are used for the splitting test. A summary of test results are presented in Table 6.2.

Figure 6.6 Splitting tensile strength test

Table 6.2 Splitting tensile strength test results

Cylinders	Tensile Strength (MPa)
S1	3.65
S2	3.57
S3	3.00
S4	3.12
S5	2.85
S6	2.81
Average	3.16
Standard Deviation	0.33

6.4 Measurements in Beam Test

During the beam test, flexural load, axial strains in FRP plate, and deflection at the top of the notch are recorded. FRP axial strains are obtained with electrical resistance strain gauges of 120 *ohm* resistance and 6 *mm* gauge length on the FRP surface.

A steel bar is attached to the beam by bolts in support points at half height of the beam, and a linear resistance transducer is used to measure the deflection of the beam centerline by attaching its one end to the beam and the other to the steel bar as shown in Figure 6.7.
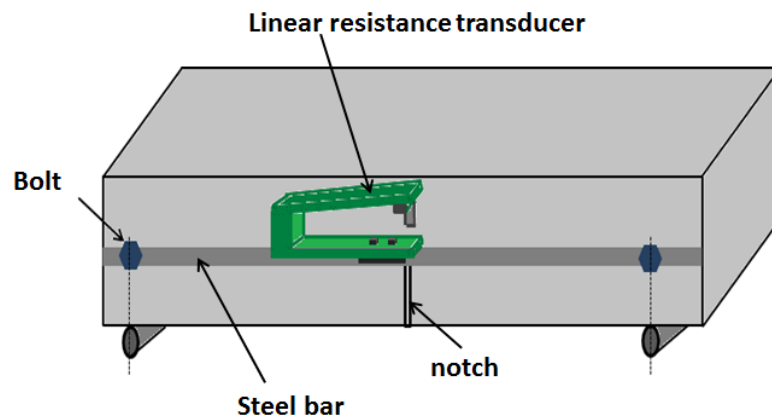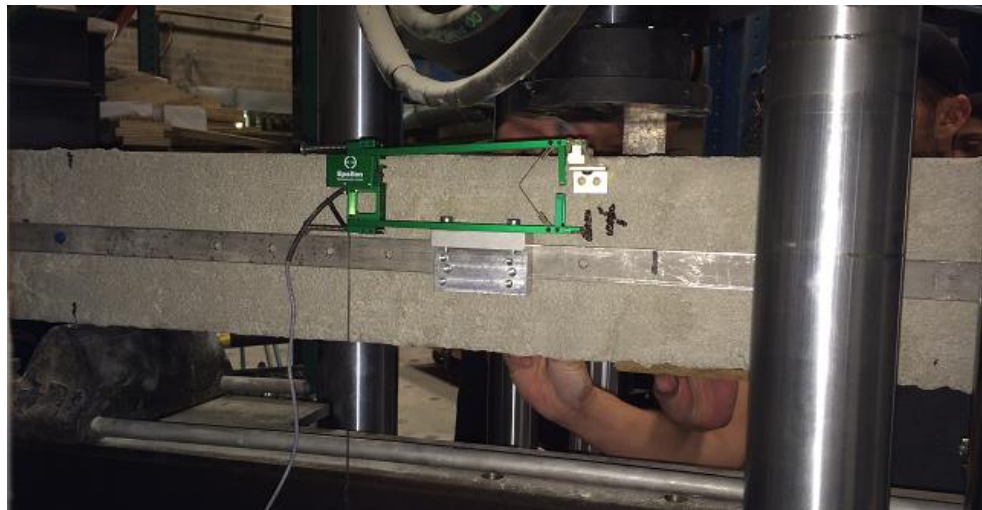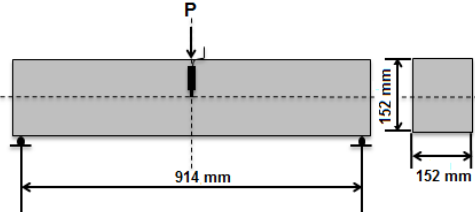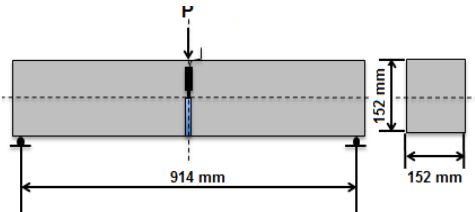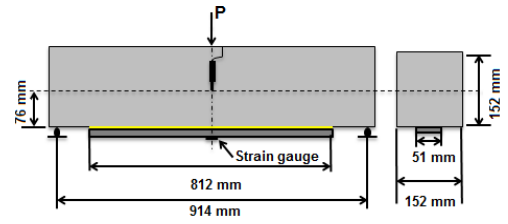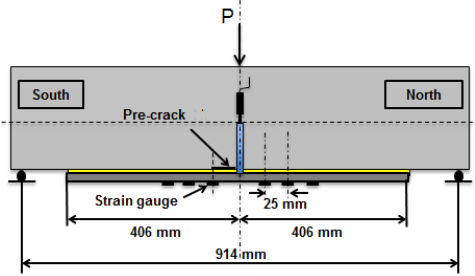
Figure 6.7 Application of resistance transducer for mid-span deflection measurement
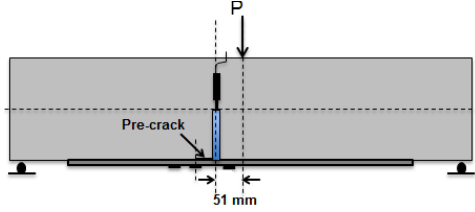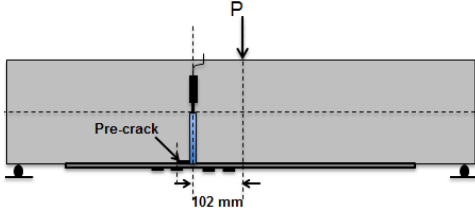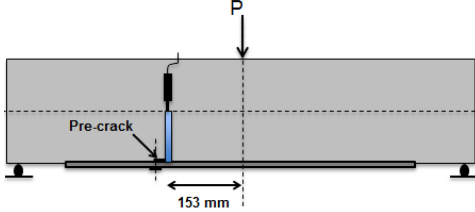
6.5 Beam Test Matrix

Twenty-four (24) specimens are tested in the beam test. Table 6.3 provides a summary of the specimen IDs, numbers of specimens, the notch locations, and number of strain gauges and their arrangements. South and north in this table serve as the indicators for parts of the beam in either sides of the notch. The pre-crack is provided in the south direction. The control specimens CC-1, CC-2, and CC-3 have one strain gage at mid-

span. The strain gauges arrangements in notched-strengthened specimens are different in each specimen as shown in the table. However, all of them have one strain gauge at the tip of the pre-crack in the south direction. The first strain gauge in the north direction is 25 *mm* away from the notch. The distance of strain gauges from each other is 25 *mm.*

Table 6.3 Beam test matrix

Specimen ID	Description	Dimensions	Number of Strain gages
C-1 C-2 C-3	Control No notch No FRP		0
C-4 C-5 C-6	Control No FRP		0
CC-1 CC-2 CC-3	Control No notch		1
CMC0-1 CMC0-2 CMC0-3 CMC0-4 CMC0-5 CMC0-6	Mid-span notch CFRP		2@south,1@north 2@south,2@north 3@south,0@north 1@south,0@north 11@south,3@north 11@south,3@north

CMC2-1 **CMC2-2** **CMC2-3**	Notch 51 *mm* (2 *in*) away from mid-span		2@south,0@north 2@south,1@north 2@south,1@north
CMC4-1 **CMC4-2** **CMC4-3**	Notch 102 *mm* (4 *in*) away from mid-span		2@south,0@north 2@south,0@north 2@south,2@north
CMC6-1 **CMC6-2** **CMC6-3**	Notch 153 *mm* (6 *in*) away from mid-span		1@south 1@south 1@south

6.6 Experimental Observations of Beam Tests

In the following, the experimental observations for each group of specimens that are shown in Table 6.3 are described in detail.

6.6.1 Control Specimens C-1, C-2, and C-3

This group of un-notched control specimens is carried out for checking set-up function and its calibration. They are also used for calculating the concrete's modulus of rupture.

The failure cracking starts at the bottom of the beam where is very close to the mid-span, and then propagates to the loading point as shown in Figure 6.8. Figure 6.9 presents the load vs. mid-span deflection curves. The average value of the maximum bearing load is 15.25 *KN* with a standard deviation of 0.52 *KN*. The specimens show deflections compatible with the theoretical maximum deflection. The theoretical maximum deflection is:

$$\frac{PL^3}{48EI} = \frac{15.25 \times (914)^3}{48 \times 23.618 \times (\frac{152 \times 152^3}{12})} = 0.23 \ mm \tag{6.1}$$

Figure 6.8 Failure of beam C-2
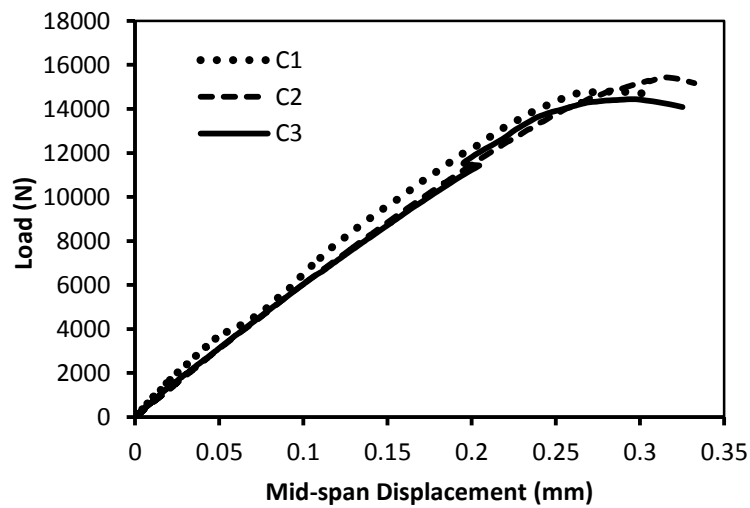
Figure 6.9 Load vs. mid- span deflection curves for specimens C-1, C-2 and C-3

The tensile strength of concrete subjected to flexural loading is named as the concrete's modulus of rupture. It has different value than the split tensile strength of concrete, f_t, and can be calculated by:

$$f_r = 1.5 \frac{PL}{bh^2}$$ (6.2)

where P is the maximum bending load in a rectangular concrete beam with length of L, width of b, and height of h. Using Equation 6.2 and the experimental maximum loads, the average value of rupture modules of specimens C-1, C-2, and C-3 is 5.67 MPa with a standard deviation of 0.09 MPa. This value is very high compared to the value from the empirical equation for calculation of the concrete's modulus of rupture in ACI 318:

$$f_r = 0.62 \sqrt{f_c'}$$ (6.3)

Equation 6.3 results in the magnitude of 3.42 MPa for the concrete's modulus of rupture. It should be noted that concrete properties have large variations, and the ACI equation is an empirical equation for design purpose, which is not necessary to be accurate for each individual specimen.

6.6.2 Control Specimens C-4, C-5, and C-6

This group of control specimens is used to study the behavior of concrete cracking at the top of the notch. The failure cracking starts at the top of the notch in mid-span and propagates to the loading point. The average value of maximum bearing loads of these three specimens is 3.06 KN (standard deviation of 0.21 KN) that is about 20% of the maximum loads in the beams without notch (C-1, C-2, and C-3). Based on Equation 6.2, the maximum load of the beam with 1/2 depth due to the notch should be 25% of those beams without notch. The saw cut may introduce some micro-cracks in concrete at the

top of the notch, which will reduce the load capacity. The self-weight of the part below

the half height of the beam is an additional load needed to be resisted by the part at the

top of the notch. This additional load is not shown in the measured results. Also, the

variations of concrete and errors of measurements may also contribute this 5% difference

between the theoretical prediction and measured results. The results of C-4, C-5, and C-6

are used to find the fracture energy of plain concrete in numerical analysis that will be

explained later in this chapter.

6.6.3 Control Specimens CC-1, CC-2, and CC-3

The specimens CC-1, CC-2, and CC-3 are CFRP-strengthened beams without

notch. They are used to investigate the behavior of strengthened beams in reality. Failure

types of all three specimens are IC debonding failure. According to the experimental

observations and pictures that are taken in each step of loading to follow the debonding

behavior, the failure processes are:

1. A major vertical flexural crack starts very close to the mid-span of the concrete

    beam (Figure 6.10a);

2. A diagonal flexural/shear crack starts close to the first flexural crack, about 25 to

    40 *mm* from the first one (Figure 6.10b);

3. FRP debonding along the FRP/concrete interface initiates at the tip of the

    diagonal crack (Figure 6.10c), progressing toward the closer support;

4. Sudden final failure step includes: the diagonal crack merging to the first flexural

    crack, the merged crack reaching the loading point, and the FRP debonding

    continuing to the end of the FRP plate (Figure 6.10d).

The average of maximum loads is 20.25 *KN,* with a standard deviation of 0.36

KN, which is about 33% more than the average of maximum loads of un-strengthened

beams (C-1, C-2, and C-3). It means that the application of CFRP strengthening system

increases the flexural loading capacity of concrete beams.

(a)   (b)

(c)   (d)
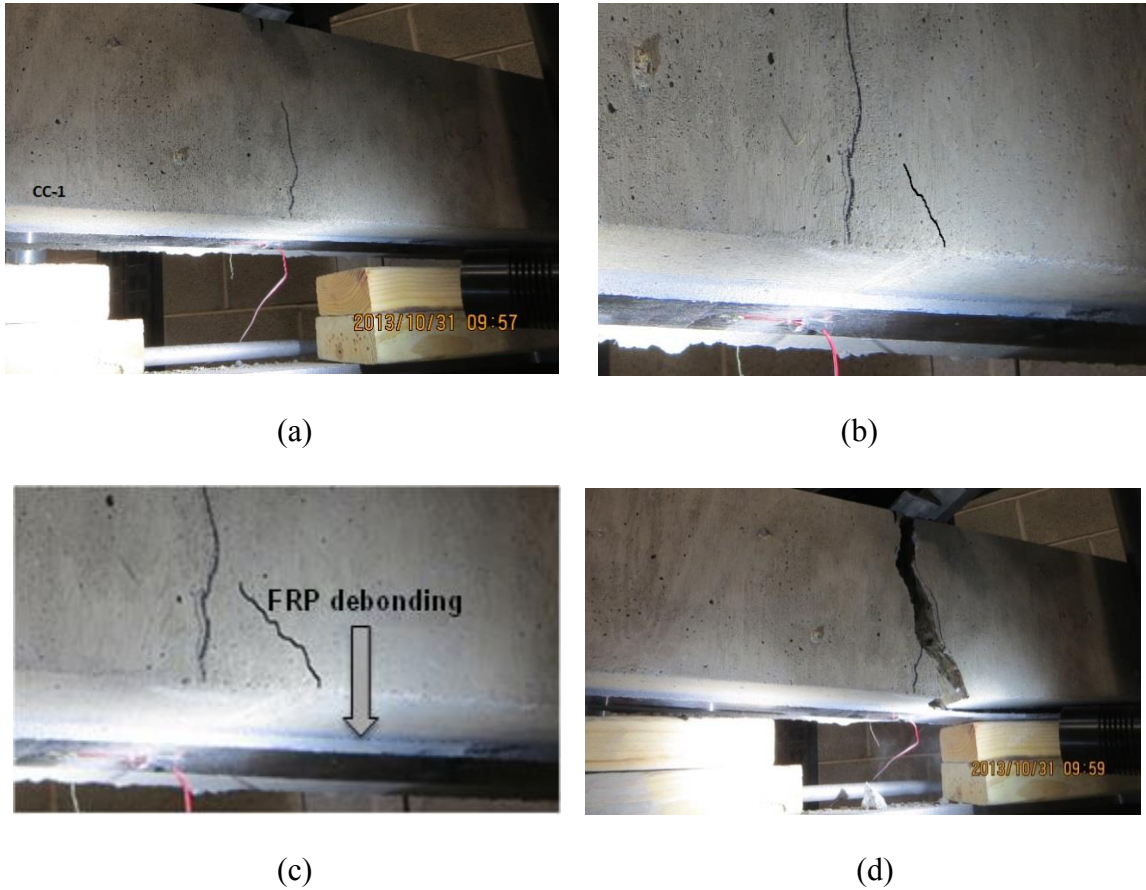
Figure 6.10 IC debonding failure processes of beam CC-1

6.6.4 CFRP-Strengthened Beams with Mid-span Notch (CMC0-1 to CMC0-6)

Six beam specimens (CMC0-1 to CMC0-6) are used to study the behavior of IC

debonding failure when the major flexural/shear crack is at mid-span. The IC debonding

failure processes in this group of specimens are:

1. Cracking starts at the top of the notch (Figure 6.11a);

2. A diagonal flexural/shear crack starts close to the notch, about 25 *mm* from the notch (Figure 6.11b) randomly in the south or north direction, or even in both directions;

3. FRP debonding along the FRP/concrete interface initiates at the tip of the diagonal crack and propagates toward the closer support (Figure 6.11c);

4. Sudden final failure step includes: the diagonal crack merging to the notch, the crack at the top of the notch reaching the loading point, and FRP debonding continuing to the end of the FRP plate (Figure 6.11d).
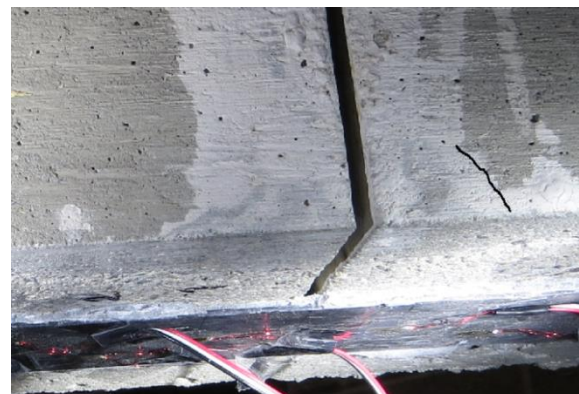
(a)   (b)
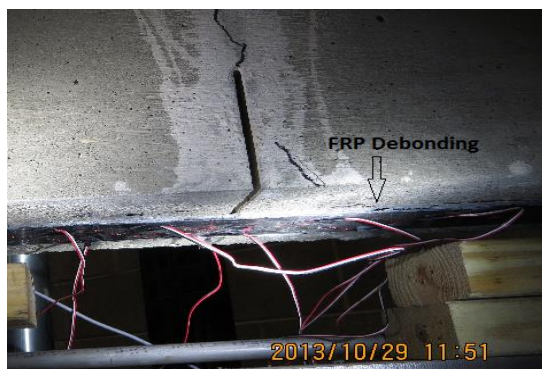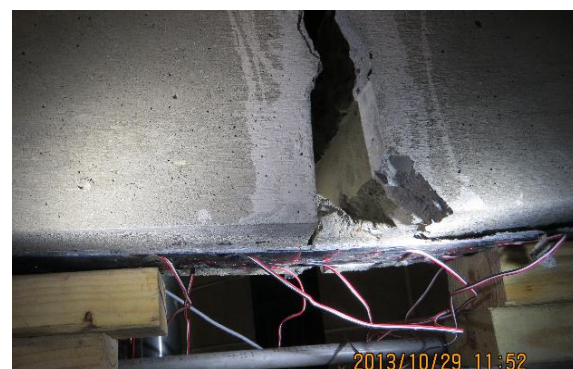
(c)   (d)

Figure 6.11 IC debonding failure processes of beam CMC0-5

There is a wedge of concrete attached to the FRP plate (Figure 6.11d) that shows diagonal cracking inside the concrete. Actually, the debonding cracking does not start at the tip of the pre-crack. Instead, it starts at the tip of the diagonal crack in either side of the notch, or even in both sides. Therefore, the applied pre-crack does not work as the initiation point of the FRP debonding and it does not control which side of the notch to start the FRP debonding.

By comparing Figures 6.10 to 6.11, it can be seen that the failure processes are compatible. The notched-strengthened beams follow the debonding behavior of the un-notched-strengthened beams.

6.6.5 CFRP-Strengthened Beams with Notches Away from Mid-span

In order to study the sensitivity of IC debonding failure to the location of the major flexural/shear crack, the notch location is moved away from the mid-span in intervals of 51 *mm*. In specimens CMC2 and CMC4 (51 and 102 *mm* away from the mid-span), the notch triggers the IC debonding failure. The debonding starts close to the tip of the notch and propagates in the south direction (Figure 6.12a and b). However, in specimens CMC6 (153 *mm* away from the mid-span), the debonding starts close to the flexural crack at the mid-span and propagates in the north direction, which is the part without the notch (Figure 6.12c). The failure processes of beams CMC2 and CMC4 are:

1. Diagonal cracking starts at the top of the notch;
2. Mid-span flexural crack initiates;
3. Second diagonal crack starts 25 to 40 *mm* from the notch in the south direction;

4. FRP debonding initiates at the tip of the second diagonal crack along the FRP/concrete interface and propagates toward the closer support;

5. Sudden final failure step includes: the diagonal crack merging to the notch, the crack at the top of the notch reaching the loading point, and FRP debonding continuing to the end of the FRP plate.
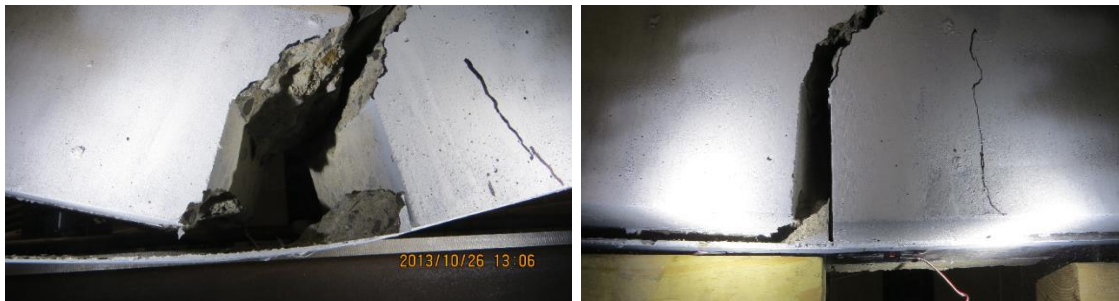
(a)   (b)

(c)

Figure 6.12 Failure of beams: (a) CMC2-1, (b) CMC4-2, and (c) CMC6-3

The failure processes of beam CMC6 are:

1. Mid-span flexural crack starts;

2. Diagonal crack initiates 25 to 40 *mm* from the mid-span crack in the north direction;

3. FRP debonding starts at the tip of the diagonal crack and propagates along the FRP/concrete interface;

4. Sudden final failure step includes: the diagonal crack merging to the mid-span crack, the mid-span crack reaching the loading point, and FRP debonding continuing to the end of the FRP plate. There is also a diagonal crack at the top of the notch, but it never reaches the loading point, and the FRP under the notch is not debonded.

It is worth mentioning that the concrete wedge attached to the FRP plate is seen in all specimens due to the diagonal crack that forms close to the major flexural/shear crack or notch. The Comparison of debonding processes of specimens CMC6 and CMC0 shows that the FRP debonding in both groups of specimens follows the same behavior. Therefore, the specimens with the notch 153 mm away from the mid-span essentially behave exactly as the specimens without any notch.

6.6.6 Comparison of Experimental Maximum Flexural Loads

Figure 6.13 compares the load vs. mid-span displacement curves for specimens CC and CMC0. Specimens CMC0 are shown by dashed lines and specimens CC are shown by solid lines. As it can be seen, specimens CC behave stiffer before the mid-span cracking and then behave like specimens CMC0. It is reasonable because specimens CC do not have a notch. Once the mid-span crack initiates in specimens CC, their behavior becomes very close to the behavior of specimens CMC0, where a notch is cut at the mid-span. Therefore, specimens CMC0 can simulate the real behavior of FRP-strengthened concrete beams (specimens CC) in their ultimate stage. This also verifies the original idea

to evaluate the FRP/concrete bond in real beams when this type of specimen was designed by Harries et al. (2012).
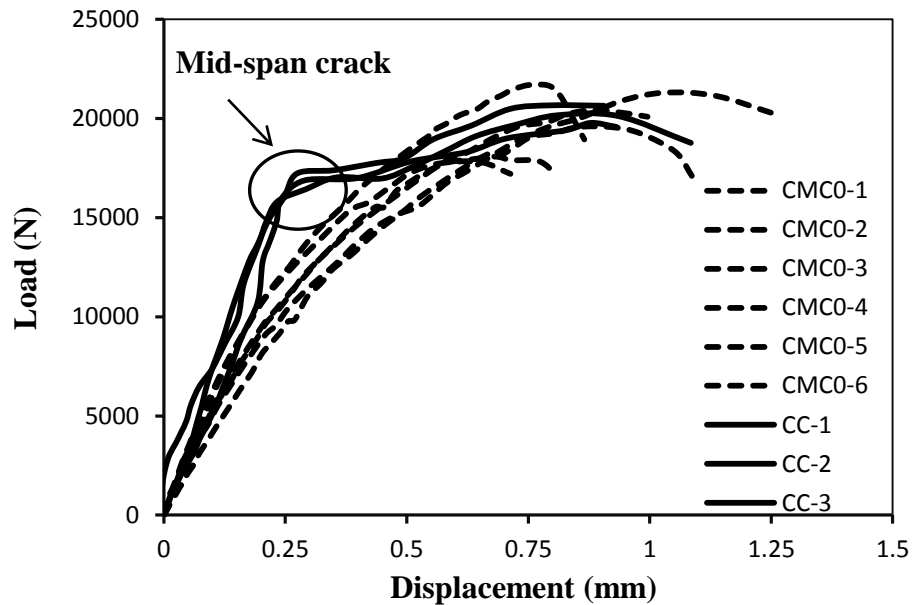
Figure 6.13 Load vs. mid-span displacement curves of specimens CMC0 and CC

The average and the standard deviation of the maximum applied loads of each group of the specimens are presented in Table 6.4. The maximum loads of CC, CMC0 and CMC6 are almost the same. It is worth mentioning that the failure processes of these specimens (CC, CMC0, and CMC6) follow the same behavior as described in the previous sections. The FRP debonding failure of CMC6 initiates at the tip of the diagonal crack close to the mid-span flexural crack as specimens CC and CMC0 (in specimens CMC0, the notch at the mid-span presents the flexural/shear crack at the mid-span).

The maximum loads of CMC2 and CMC4 are slightly higher (about 1.7 and 5.4 % higher than that of CMC0) and CMC4 has a maximum load 3.6% larger than that of CMC2. It seems that as the major flexural/shear crack is moved away from the mid-span, but not too far (less than 153 *mm* in this test), the maximum flexural loading

capacity increases slightly. Although the numbers of specimens in each group are too

small to make a conclusion, this apparent toughening may be explained through the

findings by numerical analysis that will be discussed in the next section.

Table 6.4 Average of maximum bearing loads of beam specimens

Specimens	Number of specimens	Average maximum load (KN)	Standard Deviation (KN)
C	3	15.25	0.52
CC	3	20.25	0.36
CMC0	6	20.22	0.95
CMC2	3	20.57	1.54
CMC4	3	21.31	0.35
CMC6	3	20.23	0.42

6.6.7 Bond-Slip Relationships of Beam Specimens

Specimens CMC0-5 and CMC0-6 have strain gauges along the entire FRP plate in

the south direction. Using the measured FRP strains and Equations 2.1 and 2.2, the bond-

slip relationships are calculated and presented in Figure 6.14. Since the debonding starts

beyond the location of the first strain gauge, the second and third strain gauge values are

applied for the bond stress calculations. The average of the maximum bond strength is

$\tau_{max} = 3.23\ MPa$, and the average of the interfacial fracture energy is $G_f = 0.65 N/mm$.

By comparing these values to the bond strength and fracture energy values of the single

shear pullout test ($\tau_{max} = 3.65\ MPa, G_f = 1.41\ N/mm$), it can be seen that both bond

strength and fracture energy are smaller in beams. Numerical analysis is performed in the

following to find the explanation for the smaller values of the bond-slip behavior of the

FRP/concrete interface in beam specimens than that in the shear specimens.
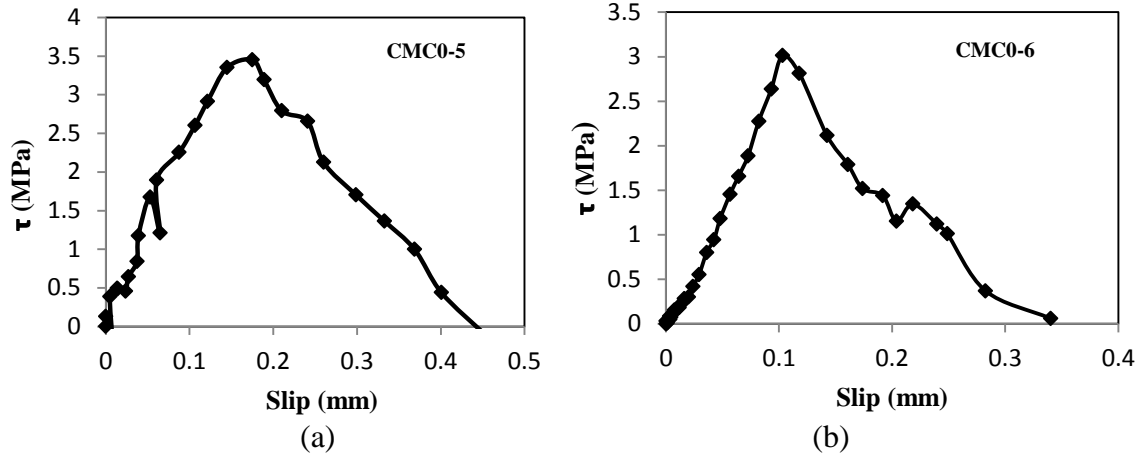
Figure 6.14 Bond-slip curves of specimens: (a) CMC0-5, (b) CMC0-6

6.7 Numerical Analysis of Beam Test

ABAQUS 6.13 is used for the FE analysis of the beam test. The concrete damaged plasticity model is applied in XFEM for the modeling of concrete. The crack initiation criterion is the maximum principal stress criterion, in which a crack initiates if the maximum principal tensile stress reaches the tensile strength of the concrete. The crack propagates perpendicular to the direction of the maximum principal tensile stress. A linear concrete tension-softening curve is assumed for the crack propagation evolution. The results of control specimens C-4, C-5, and C-6 are used to find the fracture energy of plain concrete numerically. Figure 6.15 presents the load vs. mid-span deflection of the experimental results and the numerical results by using $G_F = 0.12 \ N/mm$ in the analysis. The average error of the maximum load between numerical and experimental results is 6.8%. Since there is a good agreement between numerical and experimental results, $G_F = 0.12 \ N/mm$ is assumed as the fracture energy of the plain concrete for the beam specimens in this study. This value is same as the one used for the concrete fracture

energy in the single shear pullout specimen analysis. Therefore, the concrete properties of

these two types of specimens are similar although they are prepared in different labs with

different constitutive materials (e.g., cement, sand and aggregate).
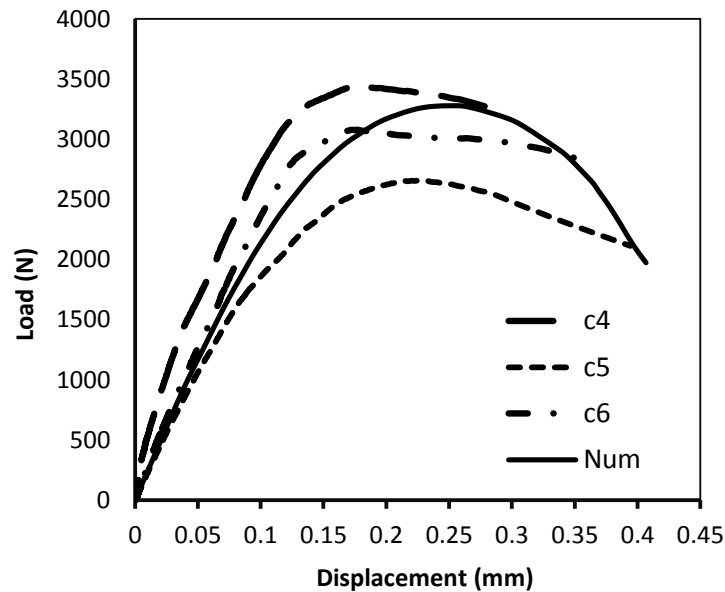
**Figure 6.15 Experimental and numerical load vs. mid-span deflections of control
beams C-4, C-5, and C-6**

6.7.1 FE Analysis of Beams CMC0

Plane stress elements are applied for the modeling. Figure 6.16 shows the typical

FE mesh. The concrete damaged plasticity model is applied in XFEM for the modeling of

concrete as described above. FRP and epoxy are modeled using a brittle cracking model.

The thicknesses of FRP plate and epoxy are 1.5 *mm* and 1 *mm*, respectively.

According to the experimental observations, the tip of the pre-crack does not

work as the debonding initiation point. Therefore, the pre-crack is not modeled in the

numerical analysis. The applied method is able to predict the cracking at the top of the

notch and also the diagonal crack about 25 *mm* from the notch. The diagonal crack

merges to the notch before ultimate failure that is in a very good agreement with the

experimental observation. Because of the symmetry, the diagonal crack is also seen in the

other side of the notch in the FE model as shown in Figure 6.16.
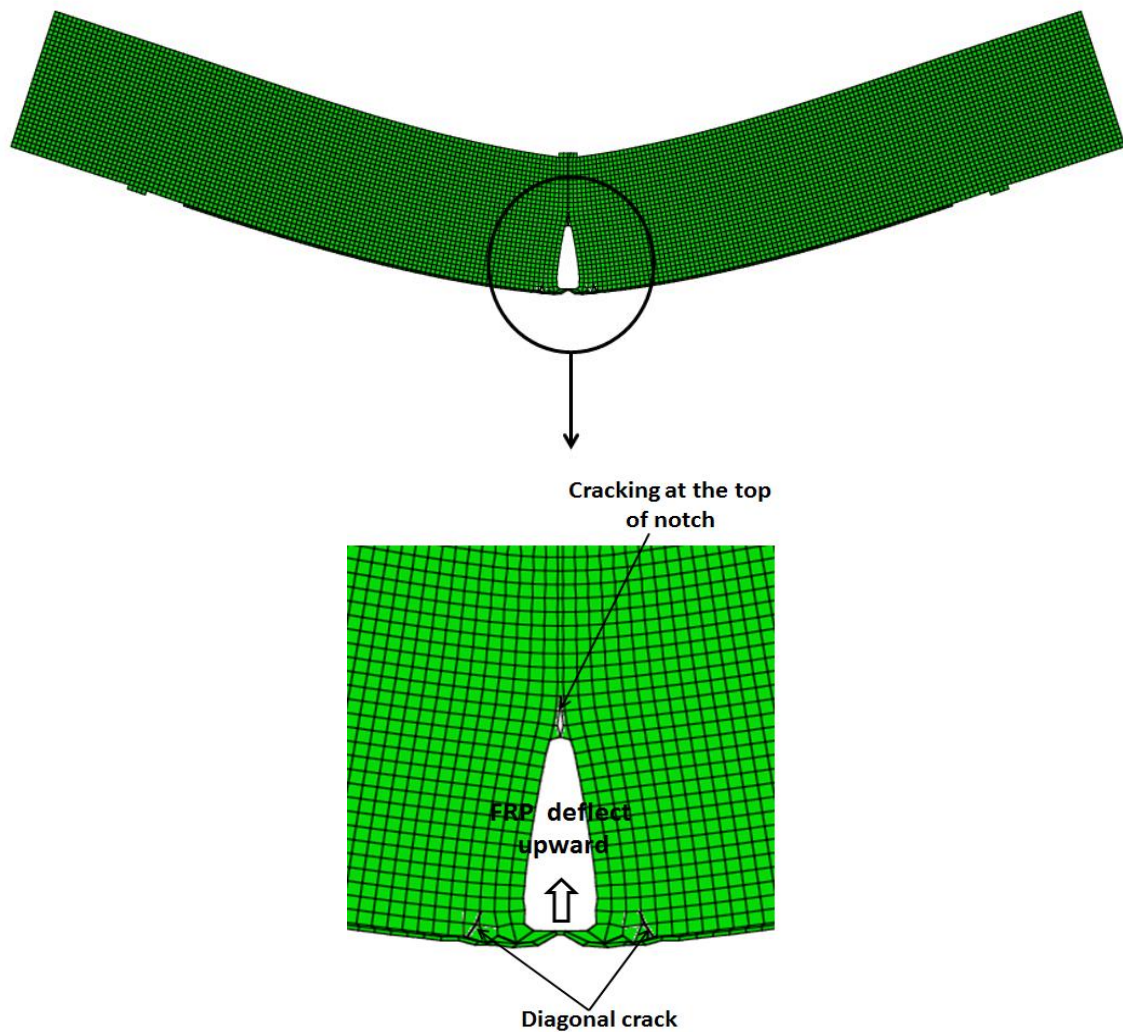
Figure 6.16 Cracking prediction of specimens CMC0 by FE analysis before debonding initiation

It can be seen in Figure 6.16 that the FRP below the notch deflects upward

relative to the FRP/concrete interface, meaning that the behavior of the beam specimens

is different than that of the single shear pullout specimens. In the shear specimens, the FRP plate is totally horizontal during the whole test procedure if the experimental error is eliminated. However, in the beam specimens, the FRP plate rotates upward when the flexural load of the beam is increased. The rotation of the FRP plate at the tip of the notch is due to the local moment created by the tension force in the FRP plate and the downward movement of the concrete as shown in Figure 6.17. This moment causes a different stress state at the FRP/concrete interface in the beam specimens than that in the shear specimens. In the shear specimens, there are constraints for the FRP plate to hold it horizontal and prevent the local moment effect on the concrete block. Also, there is no concrete block movement.
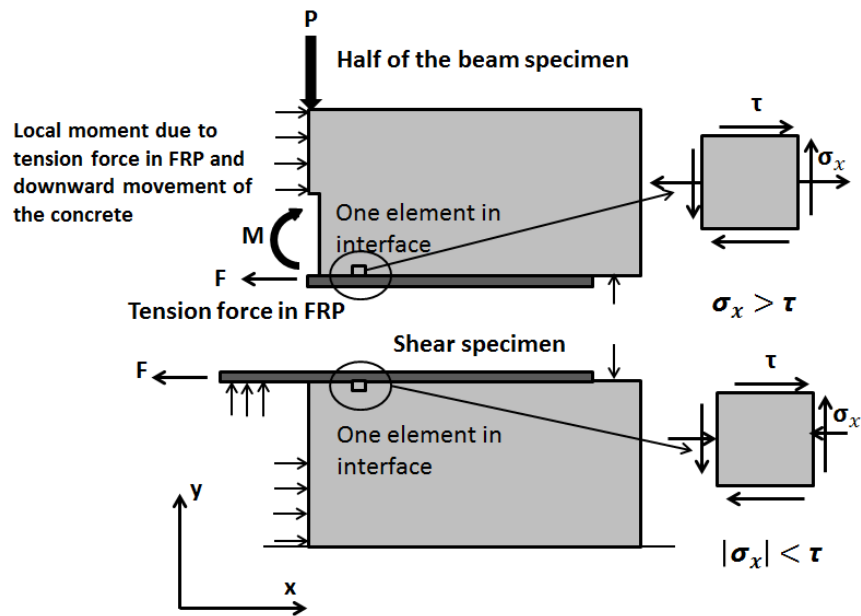
Figure 6.17 Comparison of stress state at the interface between pullout and beam specimens

As described in Chapter 5, in the single shear pullout specimens, the concrete element at the tip of the pre-crack is under shear stress, τ, and longitudinal compression

stress, $\sigma_x < 0$, while the absolute value of σ_x is smaller than shear stress, $|\sigma_x| < |\tau|$. In beam specimens, the concrete element attached to the FRP/concrete interface is under shear stress, τ, and longitudinal tension stress, $\sigma_x > 0$. The longitudinal tension stress is larger than shear stress, $\sigma_x > \tau$ (Figure 6.17).

After the diagonal crack initiation in an element at about 25 *mm* away from the tip of the notch, σ_x disappears in that element, while τ continues to increase as shown in Figure 6.18. Therefore, the FRP debonding along the FRP/concrete interface in the beam specimens initiates at the tip of the diagonal crack in the concrete side.
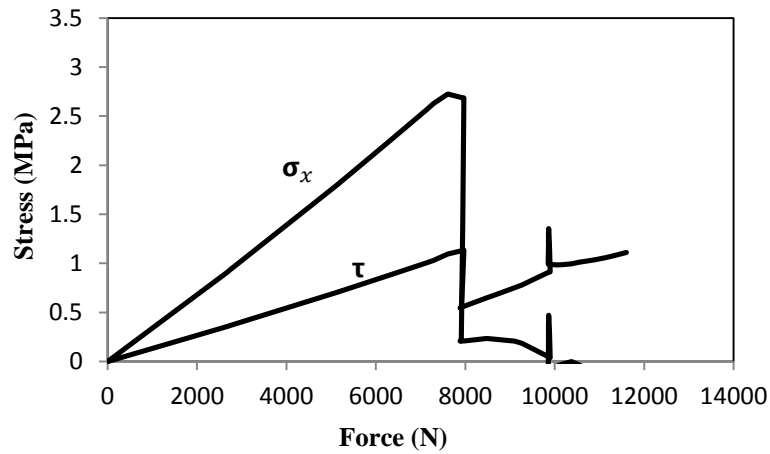
Figure 6.18 Shear and normal stresses vs. applied force for the element cracked by the diagonal crack

In order to model the horizontal FRP debonding, a damage band with a thickness of 5 *mm* is defined starting at the tip of the diagonal crack along the FRP/concrete interface as shown in Figure 6.19. A bilinear traction-separation law is assigned to the damage band. Bond strength, $\tau_{max} = 3.23\ MPa$, and fracture energy, $G_f = 0.65\ N/mm,$ are assumed according to the findings of the experimental results as discussed in section

6.6.7. A summary of the applied material properties in the FE analysis is presented in Table 6.5.
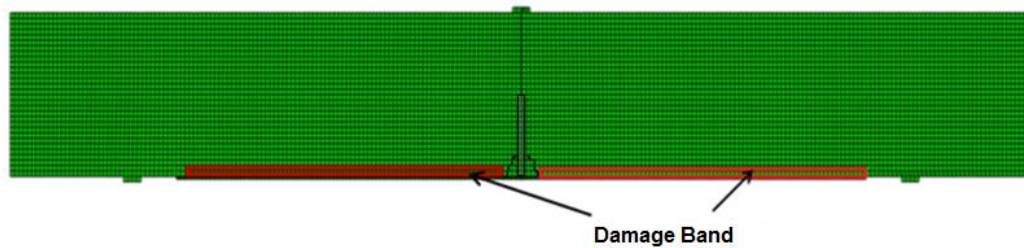
Figure 6.19 Damage band in beam specimens CMC0

Table 6.5 Material properties applied in FE analysis of beam specimens

Properties	Concrete	Damage Band	FRP	Epoxy
Modulus of Elasticity, E (GPa)	23.62	23.62	155	4.48
Tensile Strength, f_t (MPa)	3.16	3.16	2800	24.8
Compressive Strength, f_c', (MPa)	30.37	-	-	-
Shear Modulus, G, (GPa)	9.84	2.24	-	-
Shear Strength, τ_{max}, (MPa)	-	3.23	-	-
Fracture Energy, G_f, (N/mm)	0.12	0.65	-	-
Poisson's Ratio	0.2	0.2	0.25	0.3

6.7.2 Results of FE Analysis of Beam Specimens CMC0

In the FE analysis, when the element at the top of the notch (Figure 6.20) reaches the critical fracture energy of concrete, this element is not able to transfer stress anymore. At this stage, the behavior of concrete and the whole model become very unstable. Therefore, the analysis is terminated and this stage is considered to be the final failure step of the FE analysis. The cracking and deflection of the model around the notch at the final step of the numerical analysis are shown in Figure 6.20. The diagonal cracks and FRP/concrete interface cracks are also shown in this figure.
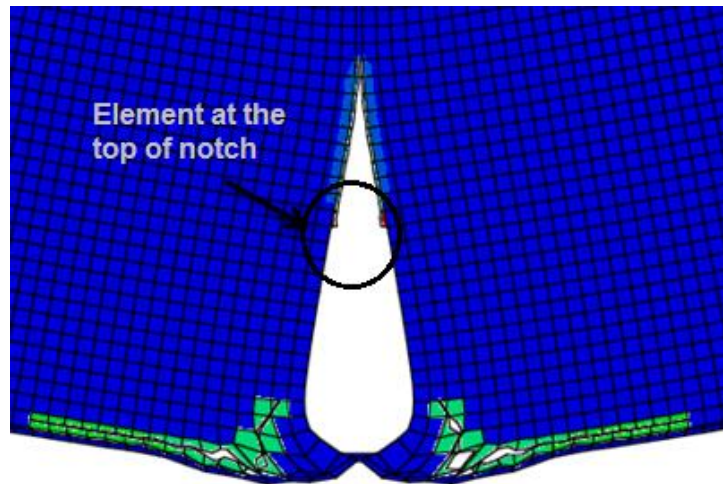
Figure 6.20 Final step of FE analysis of beams CMC0

The pictures of CMC0-1 to 6 that are taken in each step of the loading in the experimental tests show that there are diagonal cracks and also partial FRP debonding in both sides of the notch in CMC0-1, CMC0-2, and CMC0-3 before final failure as shown in Figure 6.21 for CMC0-2.
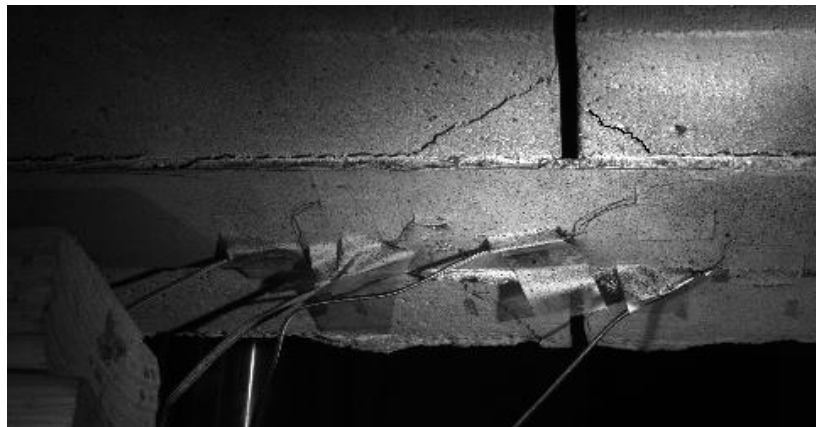
Figure 6.21 Diagonal cracks and FRP debonding in both sides of notch in CMC0-2

It is notable that it is not possible to see the diagonal cracks at both sides of the beam in all specimens through the experiments because it originates inside the concrete.

For example, no diagonal cracks are seen in CMC0-6 before the final failure during the test. However, the concrete wedge attached on the debonded FRP after failure (Figure 6.22a) indicates that there are also diagonal cracks formed during the test in this specimen. The partial FRP debonding is seen in both directions in this specimen before the final failure (Figure 6.22b). Therefore, it can be concluded that the diagonal cracks and partial debonding occur in both sides of the notch before the final failure although the final debonding happens randomly in the north or south directions.

The FE analysis catches the same failure procedure observed in the experiments. There is also a very good agreement for the load vs. mid-span deflection curves between the experimental and numerical results as shown in Figure 6.23 (the mean percentage error of the maximum load is 2.48%). The comparison of numerical results and experimental observations shows that the applied FE method is able to predict the behavior of the FRP-strengthened concrete beams.
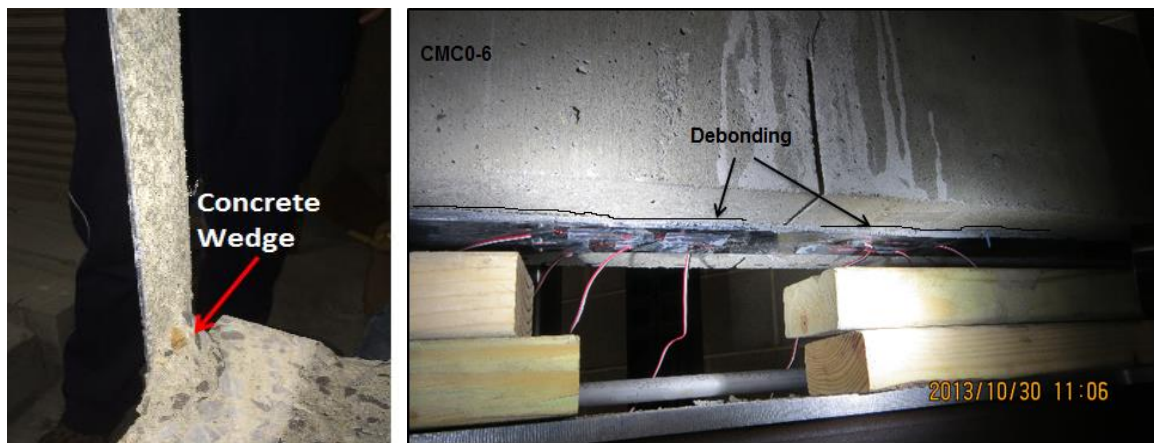
(a)   (b)

Figure 6.22 Failure of specimen CMC0-6: (a) concrete wedge, (b) FRP debonding in both sides before final failure
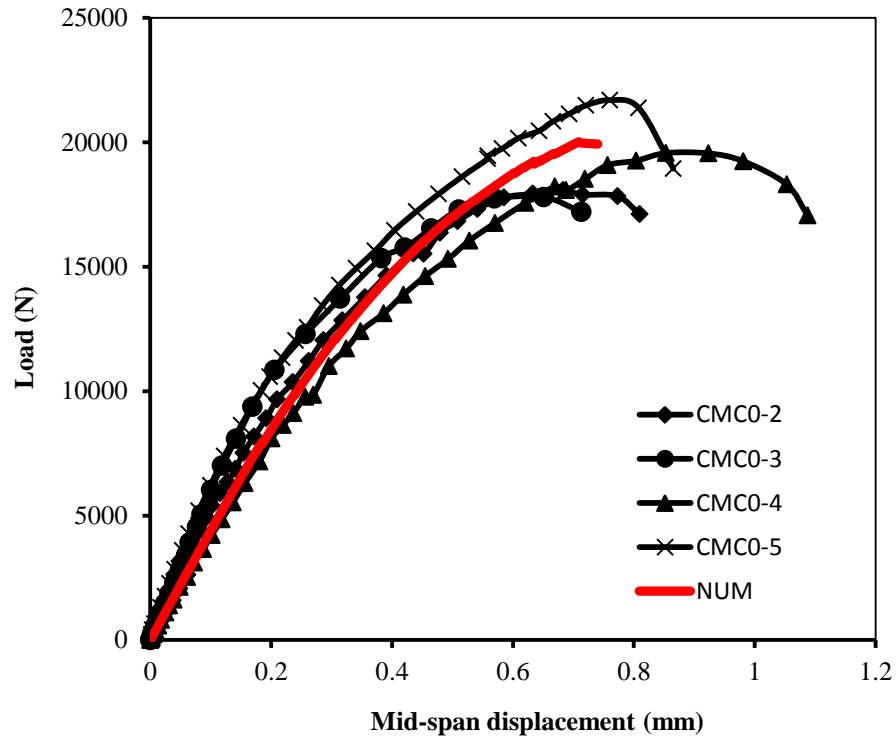
Figure 6.23 Load vs. mid-span deflection curves obtained by experiments and numerical analysis of specimen CMC0

6.7.3 FE Analysis of Beams CMC2, CMC4, and CMC6

The same material models and material properties used for the modeling of CMC0 are applied for CMC2, CMC4, and CMC6, too.

In specimens CMC2 and CMC4, the finite element analysis shows a diagonal cracking at the top of the notch, a mid-span flexural crack, and a diagonal crack at 25 *mm* from the notch in the south direction (the side closer to the support) as presented in Figure 6.24. The shear stress, τ, and the normal stress, σ_x, of the element cracked by the diagonal crack (shown in Figure 6.24) are presented in Figure 6.25. The normal stress, σ_x, drops to zero after the diagonal crack formation while the shear stress, τ, continues to increase after a small drop. This behavior happens in specimen CMC0, too (Figure 6.18).

The maximum shear stresses, τ , the maximum normal stresses, σ_x, and the corresponding load of specimens CMC0, CMC2, and CMC4, when the principal stress of the cracked element by the diagonal crack reaches to the tensile strength of concrete, are presented in Table 6.6 for the comparison. As can be seen in the table, the maximum shear stresses of specimens CMC2 and CMC4 are larger while the maximum normal stresses are smaller than those of specimen CMC0. The maximum shear stress and the maximum normal stress of specimen CMC4 are also larger than those of specimen CMC2. The reason for this phenomenon is that as the notch is moved away from the mid-span, the tension force in the FRP plate below the notch decreases due to the smaller moment at that beam section. As a result, the local moment created by the tension force in FRP (described in Figure 6.17) decreases, too. It causes less normal stress, σ_x; therefore, the maximum principal stress reaches the criterion at smaller normal stress but larger shear stress, τ. The increasing of the corresponding load when the cracked element by the diagonal crack reaches the tensile strength of the concrete may be the explanation for the slight increase of the maximum bearing flexural load as the notch is moved away from the mid-span in the experiments (section 6.6.6).

Table 6.6 Maximum shear stress and normal stress

Specimen	Maximum shear stress τ (MPa)	Maximum normal stress σ_x (MPa)	Corresponding load (N)
CMC0	1.32	2.72	7911
CMC2	1.38	2.62	8188
CMC4	1.50	2.50	8552

(a)

(b)
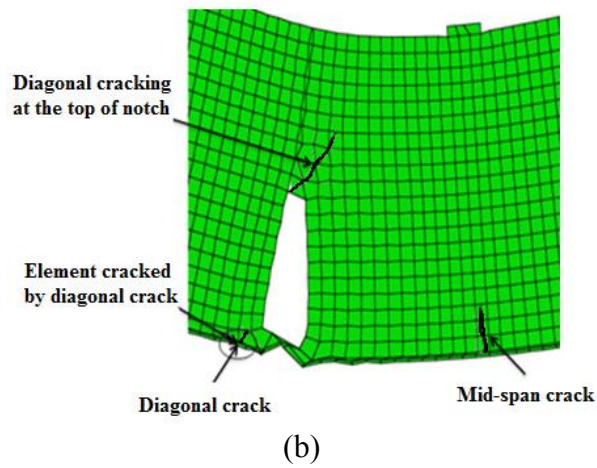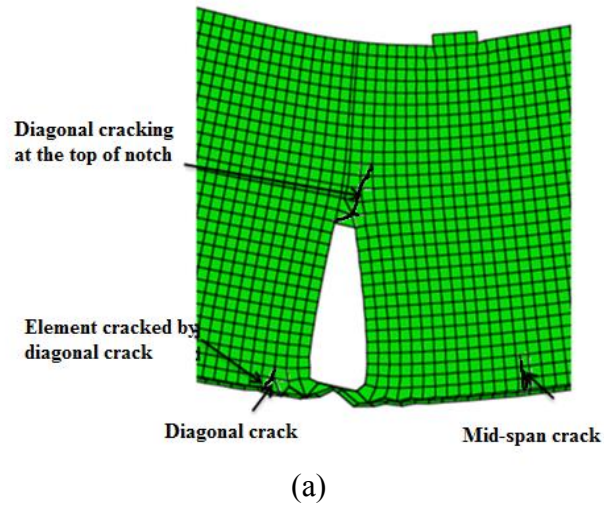
Figure 6.24 Cracking prediction of specimens: (a) CMC2, (b) CMC4, by FE analysis before debonding initiation
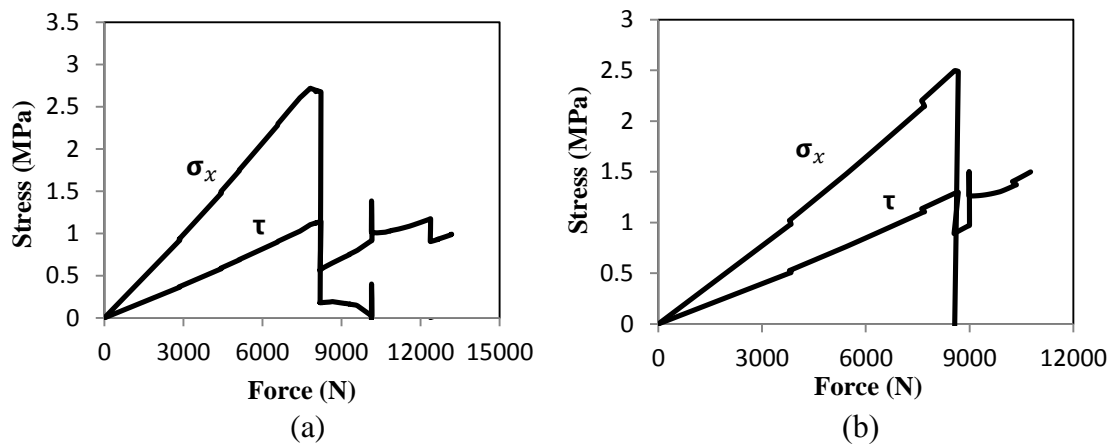
Figure 6.25 Stress state of the cracked element: (a) CMC2, (b) CMC4

In specimen CMC6, the finite element analysis does not show noticeable diagonal cracking at the top of the notch. It predicts a mid-span flexural crack and a diagonal flexural crack at 25 *mm* from the mid-span crack tip in the north direction (the side of the beam without the notch) as shown in Figure 6.26. It means that the notch does not work as a major flexural shear crack that triggers the IC debonding in this specimen. The reason is that the local moment created by the tension force in FRP at the notch is smaller than the local moment created at the tip of the mid-span crack. Thus, the diagonal crack forms close to the mid-span crack.
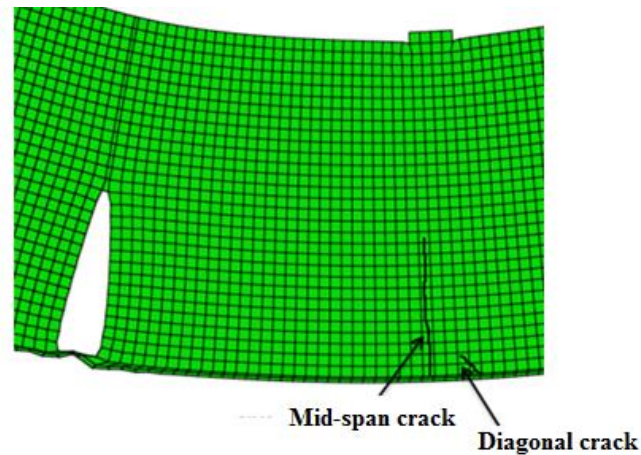
Figure 6.26 Cracking prediction of specimens CMC6 by FE analysis before debonding initiation

6.7.4 Results of FE Analysis of Beam Specimens CMC2, CMC4, and CMC6

In order to model the horizontal FRP debonding, a damage band with a thickness of 5 *mm* is defined at the tip of the diagonal crack along the FRP/concrete interface in the models of CMC2, CMC4 and CMC6. A bilinear traction-separation law is assigned to the damage band. The same values used in the FE analysis of CMC0, i.e., bond strength,

$\tau_{max} = 3.23\ MPa$, and interfacial fracture energy, $G_f = 0.65\ N/mm$, are also assigned to the damage band in this part of the FE analysis.

According to the numerical analysis, the failure processes of specimens CMC2 and CMC4 are:

1. Diagonal cracking at the top of the notch

2. Mid-span flexural crack

3. Diagonal crack close to the notch (25 *mm*) in the south side

4. FRP debonding at the tip of the diagonal crack

5. Final failure when the element at the top of the notch reaches the critical fracture energy of concrete

The failure processes of CMC6 are:

1. Mid-span flexural crack

2. Diagonal crack close to the mid-span crack (25 *mm*) in the north side

3. FRP debonding at the tip of the diagonal crack

4. Final failure when the elements at the tip of the mid-span flexural crack reach the critical fracture energy of concrete

Figure 6.27 shows the final step of the FE analyses. By comparing this figure to the pictures taken during the experimental test (Figure 6.12), it can be seen that the FE analysis predicts the IC debonding failure process very well. The curves of load vs. displacement at the top of the notch obtained numerically and experimentally are presented in Figure 6.28. The mean percentage error of the maximum flexural loads is within 1.5- 4.7 %. Therefore, the FE models successfully predict the behavior of these specimens with notches at different locations.

(a) (b)
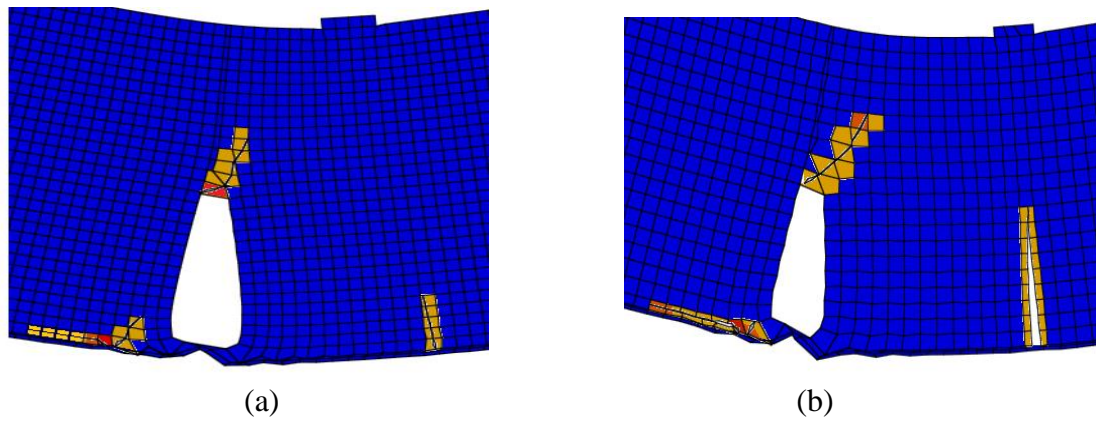
Figure 6.27 Final step of FE analysis of beams: (a) CMC2, (b) CMC4

(a) (b)

(c)
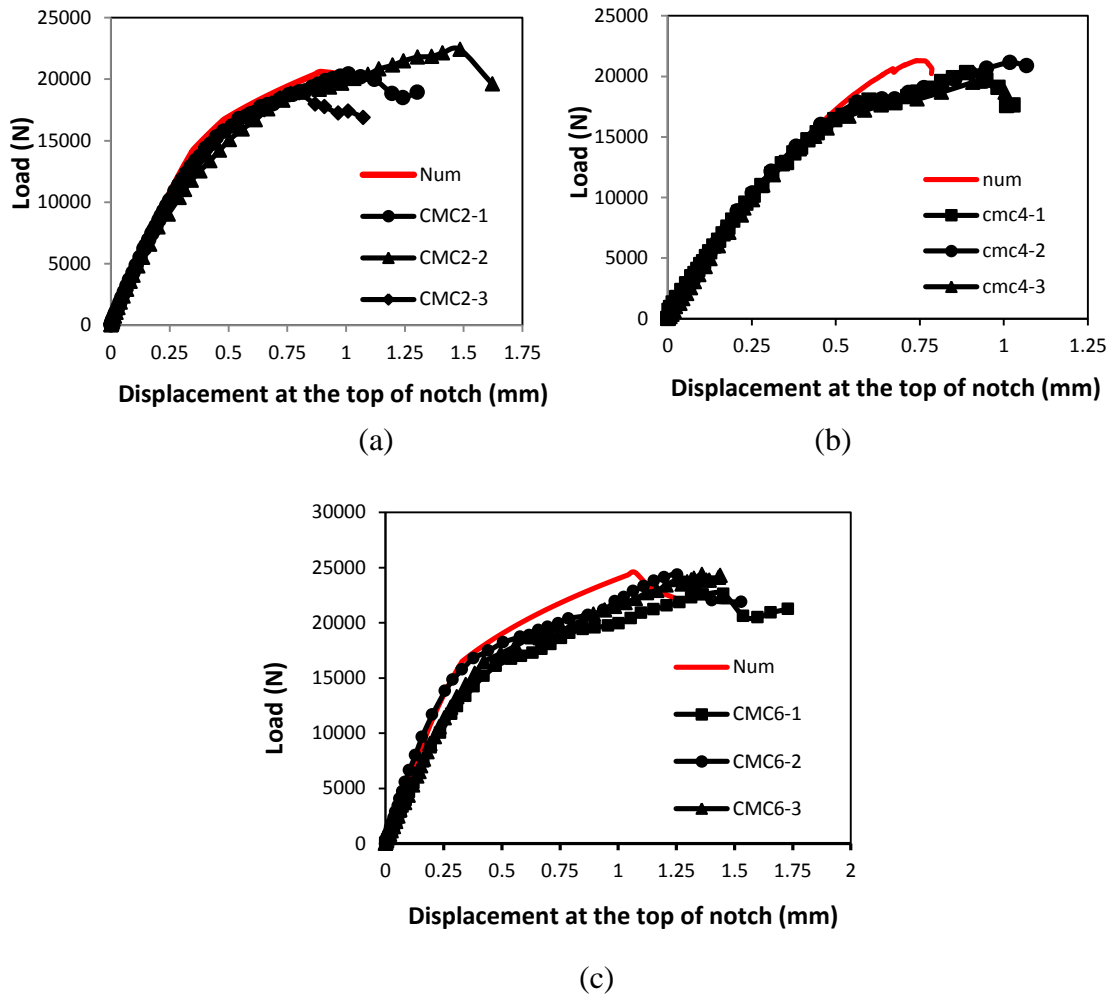
Figure 28 Experimental and numerical Load vs. displacement at the top of notch curves: (a) CMC2, (b) CMC4, and (c) CMC6

6.8 Discussion on the Numerical and Experimental Results of Beam Test

In summary, the followings are the findings of the experimental and numerical studies of the FRP-strengthened concrete beams:

1. The local moment at the tip of the notch due to the tension force in the FRP plate and the downward displacement of the concrete beam causes a diagonal crack in concrete at about 25 *mm* away from the tip of the notch. This behavior does not allow the pre-crack to control the initiation and direction of the FRP debonding.

2. The element at the tip of the diagonal crack is under shear stress and tensile stress. This stress state is different than the stress state in the element at the tip of the pre-crack in the single shear pullout specimens (shear stress and compression stress). Equation 5.5 shows that the bond strength is larger in the presence of compression stress ($\sigma_x < 0$) than the bond strength in the presence of tensile stress ($\sigma_x > 0$). Therefore, the bond strength in the FRP-strengthened beams is less than the bond strength in single shear pullout specimens. The bond-slip obtained from the pullout test does not represent the bond-slip relation of the FRP/concrete interface in the FRP-strengthened concrete beams.

3. By comparing the experimental bond-slip curves, it can be seen that the slips at the tip of the diagonal crack close to the notch (i.e., the mid-span flexural/shear crack) in the beams are smaller than the slips of the FRP plate at the tip of the pre-crack in the pullout specimens. Since the bond strength of the beam specimens is smaller too, the interfacial fracture energy of the bond

(the area under the bond-slip curve) in the beams is less than that in the pullout specimens. However, the FE analyses show that the fracture energy value does not control the final failure of the beam specimens. The plain concrete fracture energy plays the key role for the beam failure.

4. As the notch is moved away from the mid-span, the diagonal crack close to the notch forms at smaller tensile stress and larger shear stress. When the notch reaches 153 *mm* away from the mid-span where the flexural moment is much smaller than that in the mid-span, the notch does not trigger the IC debonding failure. It can be concluded that the IC debonding failure is triggered by the major flexural/shear crack in the zone with the larger moment/shear ratio (in this test setup, shear force is constant along the span) in a FRP-strengthened concrete beam.

5. As described in the literature review, there is a group of research on the IC debonding failure in the FRP-strengthened concrete beam following the idea that the FRP/concrete at the tip of the flexural/shear crack is subjected to mixed-mode loading. It is assumed that the relative vertical displacement prior to a critical diagonal crack forming between the two faces of the crack produces peeling stresses (mode I) on the interface in addition to the shear stress (mode II) due to the flexural loading on the beam as shown in Figure 6.29a. In this study, the FE analysis shows that the local moment at the tip of the notch/flexural-shear crack (Figure 6.29b) does not allow the FRP to be peeled by the relative vertical displacement. Therefore, mode I stress (σ_y) at the tip of the diagonal crack is negligible compared to the normal stress, σ_x, in

longitudinal direction and the shear stress, τ. Because of that, the bond-slip

relationship obtained by CMC0 works well for CMC2 and CMC4.

Mode I force

Mode II force

Vertical displacement

Horizontal displacement

Local moment at the tip of notch

(a)   (b)
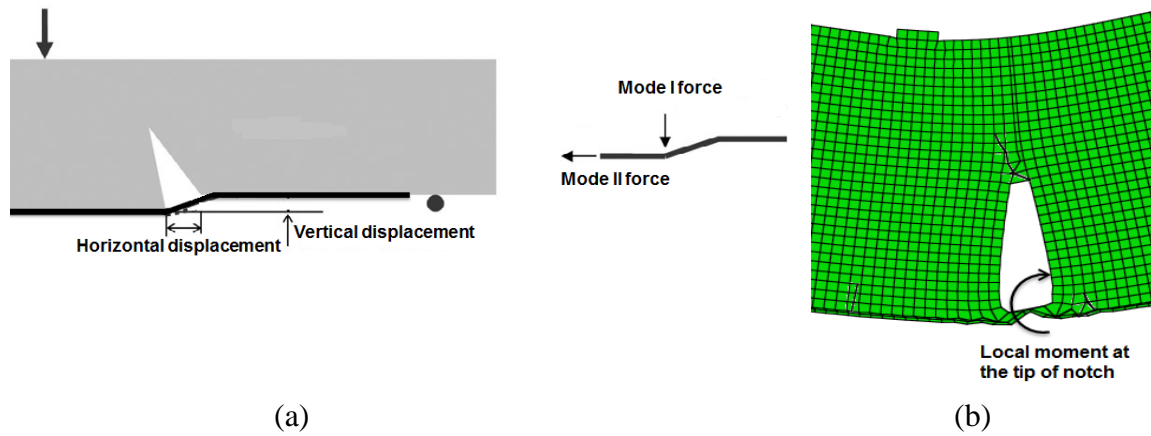
Figure 6.29 Comparison between mixed-mode assumption and the local moment at the flexural/shear crack: (a) typical mixed-mode debonding of FRP /concrete interface, (b) local moment at the tip of notch

Chapter 7 Prediction of Load Capacity Variation in FRP Bonded Concrete Specimens Using Brownian Motion

Two key parameters affecting the load carrying capacity of a bonded FRP/ concrete joint are FRP stiffness and concrete strength. In this study, pre-cured FRP plates are used in the experiments. Pre-cured plates are manufactured in a factory and the manufacturing process is normally controlled by computers. Therefore, the variation of their stiffness is relatively small. However, there is another common method to apply FRP in field, called "wet lay-up". In wet lay-up process, dry fiber sheets are saturated with a polymer and applied to the concrete surface by hand. This causes relatively large variation in properties of the cured FRP composite material. It is hard to know the exact mechanical properties of the FRP constructed by wet lay-up process. In addition, the stiffness of FRP changes during debonding process due to different amount of concrete attached to the debonded FRP at different locations. It is also inevitable to have considerable variations in the strength of concrete. Therefore, the behaviour of FRP bonded concrete members varies among specimens even when the same materials are used. The variation of localized FRP stiffness and concrete strength can be combined in a single parameter as variation of the localized interfacial fracture energy. In an effort to effectively model the effects of the variation of interfacial fracture energy on the load versus deflection responses of FRP bonded concrete specimens subjected to Mode I and Mode II loading, a random white noise using a one-dimensional standard Brownian motion is added to the governing equations, yielding a stochastic differential equation. By solving this stochastic equation, the bounds of load carrying capacity variation with 95% probability are found for different experimental tests.

7.1 Interfacial Fracture Energy Variation Sources

The stiffness of FRP and compressive concrete strength are the most effective parameters on the responses and behaviours of strengthened concrete members (Yuan et al. 2004, Lu et al. 2005, Dai et al. 2005). However, there are some variations in FRP stiffness (bending stiffness and tension stiffness, hereafter called "stiffness" only unless the tension or bending stiffness needs to be emphasized) and concrete strength, particularly the localized strength. In the following, the sources of the FRP stiffness and concrete strength are briefly explained, respectively.

One of the common methods to use FRP to strengthen existing concrete structures is wet lay-up bonding that consists of installation by hand using unidirectional dry fiber sheets or fabrics impregnated with a saturating resin on-site (ACI 440.2R 2008). Since it is hard to accurately determine the Young's modulus of the cured FRP constructed by wet lay-up process and there is variation of the cured FRP thickness, it is almost impossible to obtain the accurate magnitude of the FRP stiffness. Generally, the manufacturers provide the properties of the fibre sheets, such as Young's modulus and design sheet thickness, based on the tests in laboratories. When it is used in field, the properties of the cured FRP are affected by the skills of the workers who apply the FRP, and also by the curing process and environment in the field. Typically it is difficult to get the same level of quality control for wet lay-up FRP as for the FRP plates or strips precured in the factory. Therefore, this operation may cause differences between what is in the manufacturer's reports and the actual FRP stiffness achieved *in-situ*. The FRP properties may also be dissimilar at different locations even in the same specimen because the fibers may be curved to different extents at different locations.

Existing experimental studies have shown that in the vast majority of cases, except when a weak adhesive or a high strength concrete is used, debonding failure of an FRP-concrete bonded joint is due to the fracture within the concrete at a small distance from the concrete-adhesive interface (Chen and Teng 2001). During the debonding failure, the concrete crack path continuously changes direction and the thickness of substrate concrete layer attached to the FRP varies at different location (Coronado and Lopez 2008). This phenomenon causes the stiffness variation during debonding propagation.

Concrete is a mixture of water, cement, aggregate, and air. Variations in the properties or proportions of these constituents, as well as variations in the transporting, placing, compaction, and curing of the concrete, lead to variations in the strength of the finished concrete. In addition, discrepancies in the tests will cause to apparent differences in strength (Wight and MacGregor 2012). The concrete near the top of concrete members tends to be weaker than the concrete lower down, probably because of increased water to cement ratio at the top due to upward water migration after the concrete is placed and by greater compaction of concrete near the bottom due to the sinking of aggregates in the form during variation (MacGregor and Bartlett 1999). Therefore, there is variation of concrete strength at different spots even in same member.

Since FRP stiffness and concrete strength play important roles in predicting the load carrying capacity and failure modes in FRP-strengthened concrete members, it is useful to find a way to determine the range of actual values of FRP stiffness and concrete strength without testing each of them. The FRP stiffness and concrete strength variations can combine together as the interfacial fracture energy variation. Fracture energy is a

function of concrete strength and FRP stiffness in FRP concrete bonds (Dai et al. 2005). In this study, the concepts of Brownian motion and white noise from probability theory are used to find the fracture energy range instead of variations of the FRP stiffness and concrete strength separately. Then the calculated fracture energy range is applied to predict the load carrying capacity variation of the FRP bonded concrete specimens.

7.2 Brownian Motion and White Noise

Brownian motion is the macroscopic picture emerging from a particle moving randomly in d-dimensional space. The term "Brownian motion" can also refer to the mathematical model used to define such random movements. If it is assumed just one direction for the movements in an instant of time, then it is named one-dimensional Brownian motion.

In 1828, the Scottish botanist Robert Brown observed irregular movement of pollen suspended in water. As explained in Einstein (1905), this random movement is caused by the buffeting of the pollen by water molecules and results in dispersal or diffusion of the pollen in the water. The first mathematically rigorous construction of Brownian motion is credited to Wiener (1923), and Brownian motion is sometimes called the Wiener process. Deep studies of Brownian motion and related topics can be found in Øksendal (2003).

A real-valued stochastic process $W = \{W(t): t \geq 0\}$ defined on some probability space (Ω, F, P) is called a standard Brownian motion, if:

(i) $W(0) = 0$;

(ii) $W(t)$ has continuous sample paths almost surely

(iii) for all $0 \leq s < t$, the increment $W(t)$-$W(s)$ is independent of $F_s := \sigma\{W(u): 0 \leq u <$

$s\}$ and has Gaussian distribution with: $E[W(t)$-$W(s)]=0$, and $E[/W(t)$-$W(s)/^2]=t$-s

In the above, E is the mathematical expectation with respect to the probability

measure P, and $F_s := \sigma\{W(u): 0 \leq u < s\}$ is a σ-algebra. One can think F_s as all the

information available to the observer by time s. Note that $F_s \subset F_t$ for all $0 \leq s < t$. The

collection of σ-algebra $\{F_s\}_{s \geq 0}$ is the natural filtration generated by W. Also, each $w \in \Omega$,

the function $t \rightarrow W(t,w)$ can be regarded as a sample path or a realization of the Brownian

motion.

In a random experiment, for example infinite number of coin tossing, the outcome

determines the sample path of the Brownian motion. Then $W(t)$ is the value of this path

at time t, and this value of course depends on which path resulted from the random

experiment.

Figure 7.1 presents five different sample paths of a 1-dimensional standard

Brownian motion obtained by using MATLAB. Generally, MATLAB is an ideal

environment for this type of treatment because of high level random number generation

(Higham 2001).

Even though the Brownian motion W has continuous sample paths, it can be

shown that W is nowhere differentiable with probability 1, a mathematical fact explaining

the high irregularity of Brownian motion. This means that the derivative of the function t

$\rightarrow W(t,w)$ does not exist in the ordinary sense for almost all $w \in \Omega$. Still, we may

interpret their time derivative in a distributional sense to get a generalized stochastic

process called the white noise (Øksendal 2003). White noise generally is a random signal

that can be applied to model a totally unpredictable process. It can be considered as the

derivative of a Brownian motion existing in the stationary sense. Figure 7.2 plots a

numerical realization of a white noise.
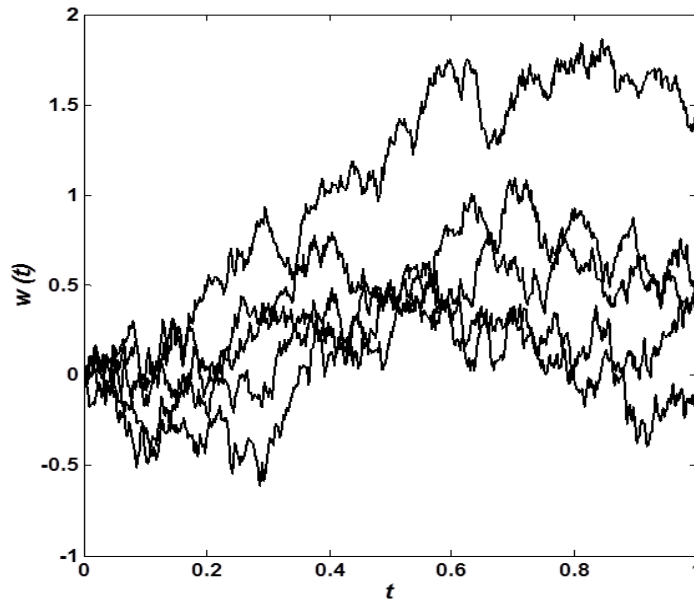
Figure 7.1 Five sample paths of a 1-dimensional standard Brownian motion
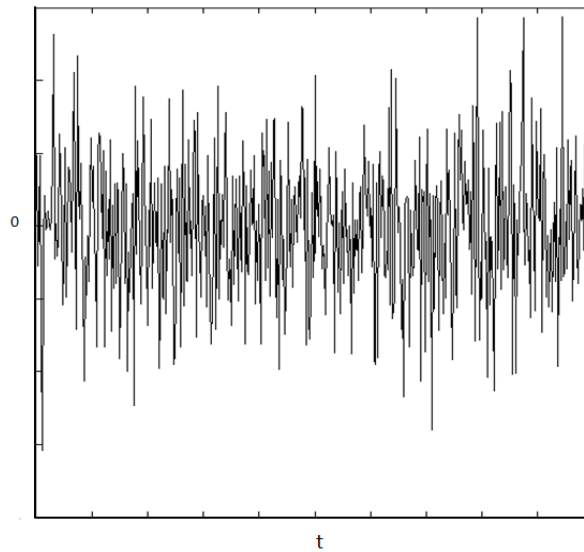
Figure 7.2 Numerical realization of a white noise

In this study, a random white noise is added to the fracture energy parameter in

the governing equations to represent the differences between actual and theoretical values

of FRP stiffness and concrete strength. The governing equations for FRP debonding from concrete subjected to Mode I and Mode II loading become stochastic differential equations, where the driven noise is a one-dimensional standard Brownian motion. By solving these equations and comparing the results with the experimental data, the ranges of load carrying capacity with 95% probability are determined for the experimental tests found in the literature.

7.3 FRP/ Concrete Interface under Mode II Loading Condition

Figure 7.3 shows an FRP/concrete interface under a pullout action, i.e., the specimen is subjected to Mode II loading (single shear pullout test). In this figure, a_0 is the initial crack length between the FRP sheet/plate and the concrete substrate, and a is the crack length during debonding propagation. As it is already mentioned, experimental studies suggest that the failure of FRP/concrete joints generally occur in concrete at a few millimetres from the FRP/concrete interface. The ultimate load of the joint therefore depends strongly on concrete failure behaviour.
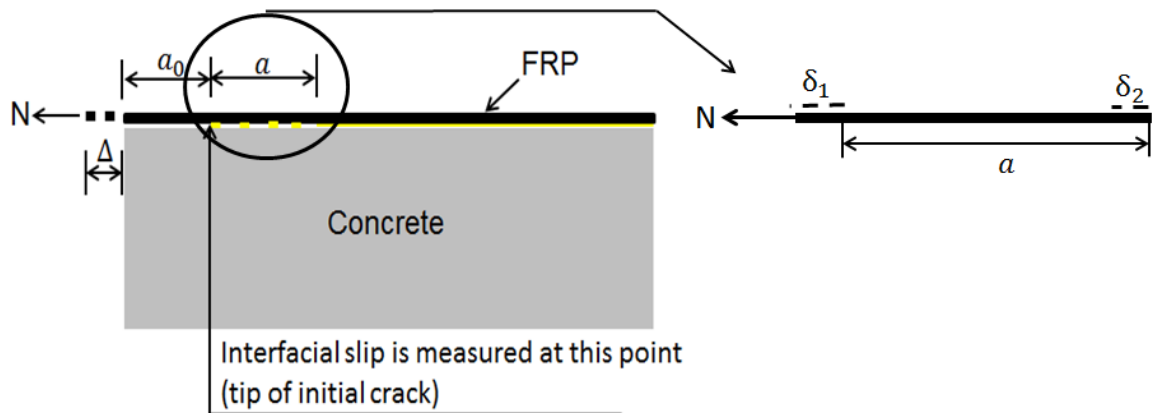
Figure 7.3 FRP-bonded concrete joint under pullout (Mode II) force

For a brittle material, the debonding region does not transfer any stresses. Theoretically, there should not be further increasing in load carrying after debonding initiation (Yuan et al. 2004). For a quasi-brittle material like concrete, the new crack surfaces formed by debonding may be in contact and are tortuous in nature. This leads to toughening mechanisms at the tip of the crack that is taken into account by a conceptual fracture process zone (FPZ). As a result of FPZ, the newly formed crack surfaces may continue to sustain more stresses after debonding initiation, which is characterized by traction-separation relationship (Shah et al. 1995). The traction-separation relationship in FRP bonded concrete joints in shear test is known as bond-slip behaviour. Figure 7.4 shows typical bond-slip behaviour of a single shear pullout test specimen. Many existing studies indicate that the interfacial fracture energy of FRP/concrete joint is a function of concrete strength and FRP stiffness. Therefore, it is assumed that variation of the interfacial fracture energy can present the variation of the concrete strength and FRP stiffness together.
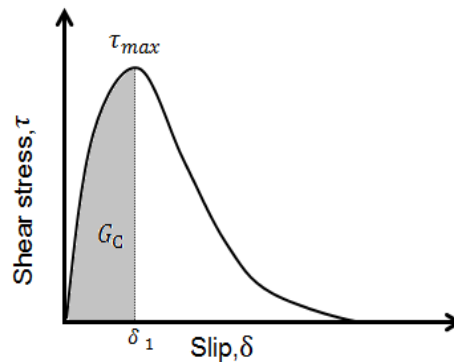
Figure 7.4 Typical bond-slip behaviour in shear test

The theoretical ultimate interfacial pull-out force in the FRP sheet, N_u, which is equal to the axial force in FRP, can be expressed as:

$$N_u = E_f t_f b_f \varepsilon_{max} \tag{7.1}$$

where E_f is elastic modulus of FRP; t_f is thickness of FRP; b_f is width of FRP sheet; and

ε_{max} is maximum strain of FRP sheets corresponding to the maximum pullout force. On

the other hand, he interfacial fracture energy can be calculated by (Dai et al. 2005):

$$G_{fII} = \frac{1}{2} E_f t_f \varepsilon_{max}^2 \tag{7.2}$$

By substituting Equation 7.2 into Equation 7.1, the maximum bearing load is a function

of the interfacial fracture energy as shown in Equation 7.3:

$$N_u = 2 G_{fII} b_f \frac{1}{\varepsilon_{max}} \tag{7.3}$$

Regarding to Figure 7.3, FRP strain at the tip of the initial crack is equal to $\varepsilon =$

$\frac{\delta_1 - \delta_2}{a}$, Where δ_1 is the interfacial slip at the tip of the initial crack and δ_2 is the interfacial

slip at the end of the debonding length. In this study, it is assumed that δ_2 is equal to zero

since it is very small compared to δ_1. This assumption is based on Hillerborg fictitious

crack model (Hillerborg et al. 1976) for concrete cracking modeling. The fictitious crack

approach assumes that the energy to initiate debonding is small compared to that required

to propagate debonding in concrete. Therefore, the energy rate term required to create

new crack, G_C (Figure 7.4), vanishes in the fictitious crack model. Using this assumption,

the FRP strain at the tip of the initial crack is equal to $\varepsilon = \frac{\delta_1}{a}$.

By substituting $\varepsilon_{max} = \frac{\delta_{max}}{a_{max}}$ into Equation 7.3, it can be rewritten as:

$$N_u = 2 G_{fII} b_f a_{max} \frac{1}{\delta_{max}} \tag{7.4}$$

where δ_{max} is the maximum interfacial slip at the tip of the initial crack and a_{max} is the

maximum crack length in front of the initial crack corresponding to the ultimate pullout

force, N_u, during the interface crack propagation (i.e. macro interface debonding). By setting $X = \frac{1}{\delta_{max}}$ and $K_0 = 2G_f b_f a_{max}$, Equation 7.4 in differential equation form is:

$$\frac{dN_u}{dX} = K_0 \qquad (7.5)$$

where K_0 is a parameter including interfacial fracture energy which is a function of the FRP stiffness and concrete strength. As discussed in the previous section, the actual FRP tension stiffness achieved *in-situ* is not the same as this calculated value. It is inevitably subjected to random fluctuations, resulting from the wet lay-up process and different amount of concrete attached to the debonded FRP at different locations. Also there are some sources for concrete compressive strength variation. In order to find the effect of the FRP tension stiffness and concrete strength variations on the ultimate load-carrying capacity (i.e. the maximum pullout load) of the specimens, a white noise is added to the parameter K_0 as in Equation 7.6:

$$K = K_0 + \alpha \dot{w} \qquad (7.6)$$

where α is a constant positive value ($\alpha > 0$) that presents the distribution or variation of experimental data, and $\dot{w}$ is a one-dimensional white noise. Since the measured value of δ is a parameter which varies due to the construction process and different amount of concrete attached to the debonded FRP at different locations, $\dot{w}$ is a function of δ (X here). By substituting Equation 7.6 into Equation 7.5, the ultimate axial force can be written as:

$$dN_u = K_0 dX + \alpha \dot{w} dX \qquad (7.7)$$

Since white noise can be formally considered as the derivative of a Brownian motion, Equation 7.7 can be rewritten as:

$$dN_u = K_0 dX + \alpha dw(X) \qquad (7.8)$$

where $w(X)$ is a one-dimensional standard Brownian motion. In this application, a Brownian motion is introduced to present the effect of totally unpredictable interfacial fracture energy variation on the load vs. deflection responses of the specimens. Equation 7.8 is a stochastic differential equation and the solution is

$$N_u = K_0 X + \alpha\, w(X) \tag{7.9}$$

It is well known that if an arbitrary random variable X has Gaussian distribution with mean μ and variance σ^2, then $\left(\frac{X-\mu}{\sigma}\right)$ has a standard normal distribution with mean 0 and variance 1 (Billingsley 1986). Recall that the stochastic process, w, is a Brownian motion having independent and stationary increments (Øksendal 2003), and for each X, $w(X)$ is a Gaussian random variable with mean 0 and variance X. Therefore, $\frac{w(X)}{\sqrt{X}}$ has a standard normal distribution. According to the probability density function, 95% of the observations fall between -1.96 and 1.96 for a variable with the standard normal distribution (Billingsley 1986) as shown in Figure 7.5. Therefore, with probability of 95%, the range of $\frac{w(X)}{\sqrt{X}}$ can be expressed as,

$$-1.96 < \frac{w(X)}{\sqrt{X}} < 1.96 \tag{7.10}$$

By substituting Equation 7.9 into Equation 7.10, the upper and lower bounds can be found for the ultimate axial force, N_u, as

$$-1.96 < \frac{N_u - K_0 X}{\alpha\sqrt{X}} < 1.96$$

$$\begin{cases} N_{lower} = K_0 X - 1.96\,\alpha\sqrt{X} \\ N_{upper} = K_0 X + 1.96\,\alpha\sqrt{X} \end{cases} \tag{7.11}$$

In Equation 7.11, the value of constant α, which represents the distribution of experimental data, is needed to determine the lower and upper bounds of the ultimate

load. This value has been obtained in this study by using the experimental data from Dai et al. (2005).
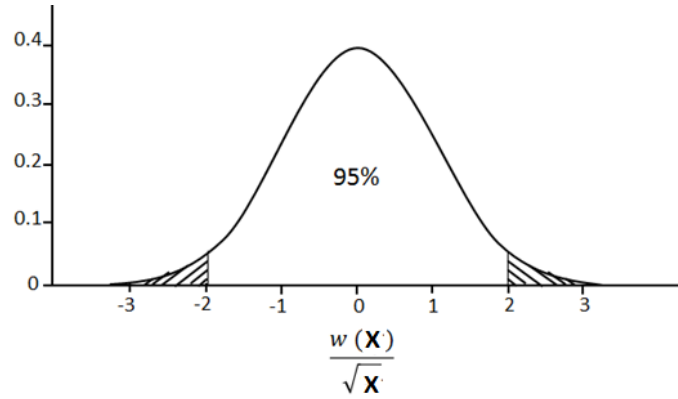
Figure 7.5 Probability density function for standard Brownian motion

Table 7.1 includes the material properties and experimental results of the pullout tests conducted by Dai et al. (2005). The width of the FRP sheets, b_f, is 100 mm. In order to use data from different tests with different materials, normalized $K_0 N_u$ against $K_0 \sqrt{X}$ curves are drawn in Figure 7.6. In this figure, the thin line represents the theoretical response calculated from Equation 7.4, the thick lines are the results from Equation 7.11, and * points are the experimental data. By adjusting the value of α in Equation 7.11, the band between the lower and upper N_u values can be changed to involve all experimental data. For these test results, $\alpha = 1200$ is a good estimation to cover the experimental data.

Because N_u is between N_{upper} and N_{lower}, and $\varepsilon_{max} = \frac{\Delta_{max}}{a_{max}}$, using Equations 7.4 and 7.11, the bounds of interfacial mode II fracture energy, $(G_{fII})_{exp}$, with 95% probability can be expressed as:

$$\left(G_{fII} - \frac{1.96\alpha\sqrt{1/\delta_{max}}}{2b_f a_{max}}\right) < (G_{fII})_{exp} < \left(G_{fII} + \frac{1.96\alpha\sqrt{1/\delta_{max}}}{2b_f a_{max}}\right) \qquad (7.12)$$

Table 7.1 Specimens of Dai et al. (2005) and their fracture energy boundaries

specimen	ε_{max}	δ_{max} (mm)	N_u (KN)	(G_{fII}) (N/mm)	(G_{fII}) lower (N/mm)	(G_{fII}) upper (N/mm)	%
CR1L1	0.00904	0.064	23.4	1.034	0.614	1.454	40.62
CR1L1	0.01046	0.066	23.1	1.384	0.905	1.863	34.70
CR1L1	0.00908	0.053	24.9	1.043	0.579	1.507	44.45
CR1L2	0.00664	0.069	33.5	1.115	0.818	1.412	26.63
CR1L2	0.00682	0.061	39.3	1.177	0.852	1.502	27.61
CR1L2	0.00732	0.077	39.3	1.356	1.046	1.667	22.86
CR1L3	0.00509	0.064	42.9	0.983	0.746	1.212	23.29
CR1L3	0.00554	0.057	38.4	1.165	0.892	1.438	23.43
CR1L3	0.00525	0.062	38.4	1.042	0.794	1.290	23.80
CR1L3	0.00496	0.059	36.9	0.930	0.690	1.170	25.81
AR1L1	0.01260	0.070	25.5	1.476	0.916	2.036	37.94
AR1L2	0.00955	0.073	833.6	1.450	1.034	1.856	28.00
AR1L3	0.00606	0.068	39.9	1.351	1.078	1.624	21.54
GR1L5	0.00732	0.062	33.4	1.171	0.825	1.517	29.54
CR2L1	0.01124	0.111	28.1	1.598	1.201	1.995	24.84
CR2L2	0.00809	0.123	43.2	1.656	1.385	1.927	32.73
CR2L3	0.00596	0.103	47.4	1.343	1.125	1.561	16.23
AR2L3	0.00668	0.111	47.1	1.642	1.406	1.878	14.37
GR2L3	0.00869	0.090	31.0	1.208	0.867	1.548	28.14
CR3L2	0.00980	0.290	47.7	2.430	2.216	2.644	8.80
CR3L3	0.00732	0.227	57.6	2.205	2.024	2.386	8.20
AR3L3	0.00923	0.309	60.9	3.135	2.940	3.330	6.22
						Average (%)	25.4
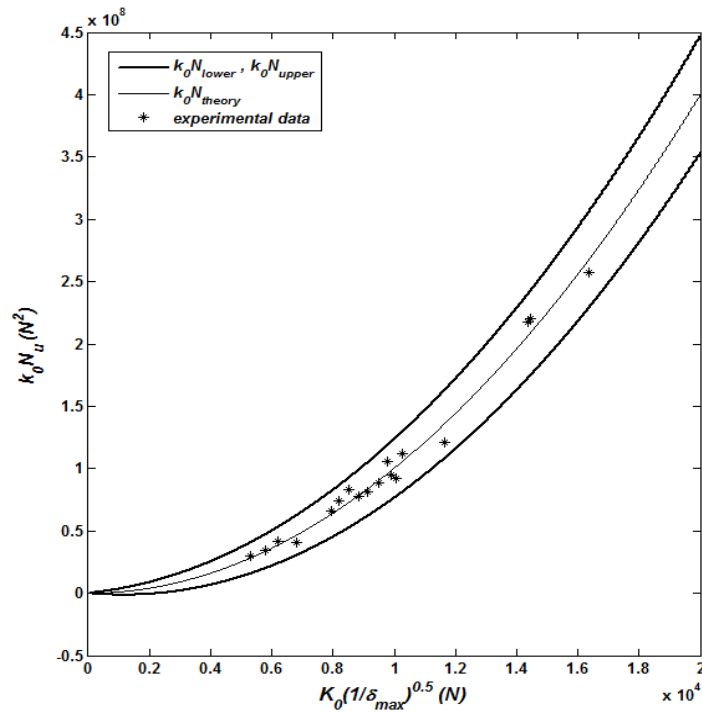
Figure 7.6 Application of experimental data from Dai et al. (2005) to find α

Using $\alpha = 1200$ and Equation 7.12, the range of mode II fracture energy bounds has been determined. In average, mode II fracture energy for this group of specimens falls between 25.4% less or more than the theoretical fracture energy.

To give an instance, the ultimate load vs. maximum slip for the first specimen in Table 7.1 (CR1L1) is shown in Figure 7.7. The thin line is the theoretical one from Equation 7.4, and the thick lines are the upper and lower bands of ultimate load based on Equation 7.11 with $\alpha = 1200$. Due to the Brownian motion, Equation 7.9 represents a stochastic process, which has many different sample paths. The dashed line in Figure 7.7 plots one of such sample paths.
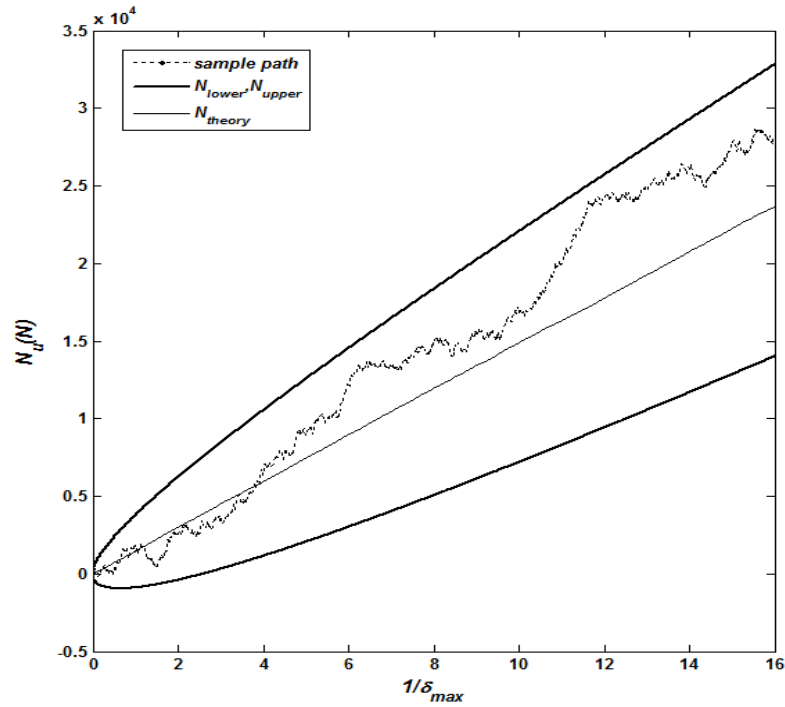
Figure 7.7 Ultimate load vs. maximum slip for specimen CR1L1

Figure 7.8 shows the experimental ultimate loads against the theoretical ones. Because the relationship between the ultimate load and mode II interfacial fracture

energy, G_{fII}, is linear (Equation 7.4), the ultimate bearing load changes 25.4% when the fracture energy changes 25.4%. In Figure 7.8, the thick lines are bands of experimental maximum load vs. theoretical one, i.e. $P_{ex} = (1 \pm 0.254)P_{th}$. This may explain why the debonding strength of FRP always exhibits quite large scatter (Mazzotti et al. 2008, Toutanji et al. 2012).

As can be seen in Figure 7.8, all experimental ultimate loads are in the bands. Therefore, it confirms that the proposed method is valid to predict the load capacity variation of the FRP bonded concrete specimens under mode II loading.
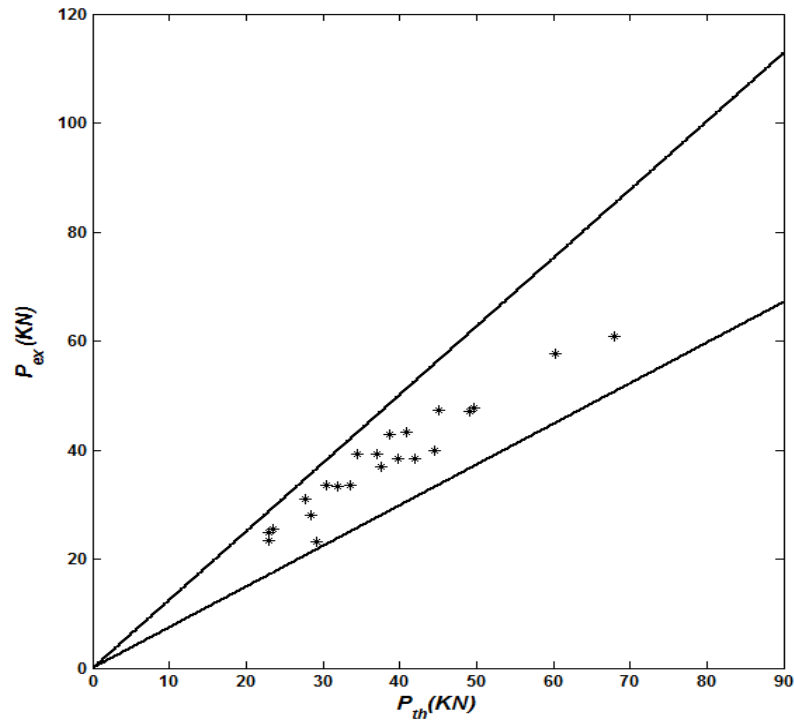
Figure 7.8 Experimental ultimate load vs. theoretical one for the tests by Dai et al. (2005)

7.4 FRP/Concrete Interface under Mode I Loading Condition

The relationship between the load and displacement in a Mode I loading condition can be obtained in a similar way of Mode II loading case. Figure 7.9 shows the schematic model around the crack tip subjected to a Mode I load, P. If the value of the crack (debonded) length, a, is small, the debonded FRP can be assumed as a cantilever beam subjected to load P, and the bonded parts of FRP can be assumed as an Euler-Bernoulli beam on an elastic Winkler foundation (Pan and Leung 2007, Dai et al 2009). However, in this study, the mode I displacement of the bonded parts of FRP, Δ_1 in Figure 7.9, is assumed equal to zero as it is done for mode II loading and discussed in the previous section. Therefore, the relationship between the ultimate Mode I load, P_u, and the corresponding mode I displacement, Δ_{max}, can be obtained as:

$$P_u = [\frac{3EI}{a_{max}^3}]\Delta_{max} \tag{7.13}$$

where EI is the bending stiffness of FRP and a_{max} is the crack length corresponding to the ultimate load.
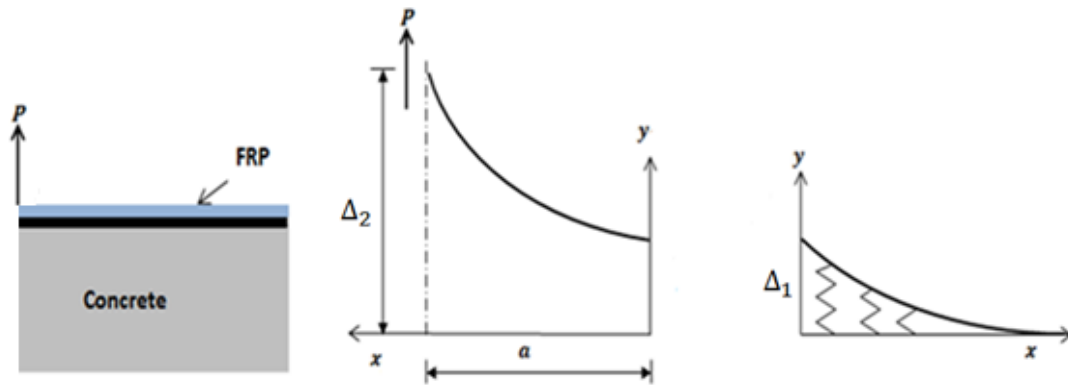
Figure 7.9 Simulation of FRP on the concrete substrate as a beam on elastic foundation for Mode I loading

Based on the compliance method, the mode I fracture energy can be expressed as (Wan et al. 2004, Dai et al. 2009):

$$G_{fI} = \frac{P^2}{2b_f} \frac{dC}{da} \tag{7.14}$$

where C is the compliance of the unbonded/debonded FRP and can be expressed by:

$$C = \frac{\Delta}{P} \tag{7.15}$$

By substituting Equations 7.14 and 7.15 into Equation 7.13, and setting $K_0 = 2b_f \, G_{fI} a$ and $X = \frac{1}{\Delta_{max}}$, the ultimate Mode I load, P_u, can be expressed as:

$$P_u = K_0 X \tag{7.16}$$

To model the unpredictable changes in the mode I interfacial fracture energy, G_{fI}, a white noise is added to the parameter K_0, where K_0 is calculated by manufacturer reported the FRP material properties and concrete strength. The process is similar to what has been done for the Mode II loading case. The upper and lower bounds for ultimate Mode I loading, P_u, with probability 95% are:

$$\begin{cases} P_{lower} = K_0 X - 1.96\alpha\sqrt{X} \\ P_{upper} = K_0 X + 1.96\alpha\sqrt{X} \end{cases} \tag{7.17}$$

To find the magnitude of α, experimental data from Wan et al. (2004) and Ouyang and Wan (2008) are used.

Wan et al. (2004) used modified double cantilever beam (MDCB) specimens to test the energy release rate of FRP debonding from concrete subjected to Mode I loading. CFRP sheets were applied to the concrete substrates by wet layup process. Ouyang and Wan (2008) used the MDCB test to measure the interfacial fracture energy of the CFRP plate debonding from concrete substrate under Mode I loading. The experimental results

of these tests are shown in Tables 7.2 and 7.3.

The normalized $K_0 P_u$ against $K_0\sqrt{X}$ curves are drawn in Figure 7.10 for the specimens in Table 7.2. The appropriate magnitude for α is equal to 200 to cover all experimental data in Wan et al. (2004). This value for experimental data in Ouyang and Wan (2008) is equal to 240 as shown in Figure 7.11.

Table 7.2 Specimens of Wan et al. (2004) and their fracture energy boundaries

Specimens	P_u (N)	Δ_{max} (mm)	(G_{fI}) (N/mm)	(G_{fI}) lower (N/mm)	(G_{fI}) upper (N/mm)	%
C4B1S1	515.86	0.58	0.545	0.467	0.622	14.13
C4B1S2	553.09	0.79	0.273	0.191	0.355	30.0
C4B1S3	518.63	0.87	0.417	0.347	0.467	12.0
C4B1S4	545.67	0.98	0.436	0.392	0.480	10.1
C4B1S5	380.97	0.68	0.391	0.342	0.440	12.5
					Average (%)	15.74
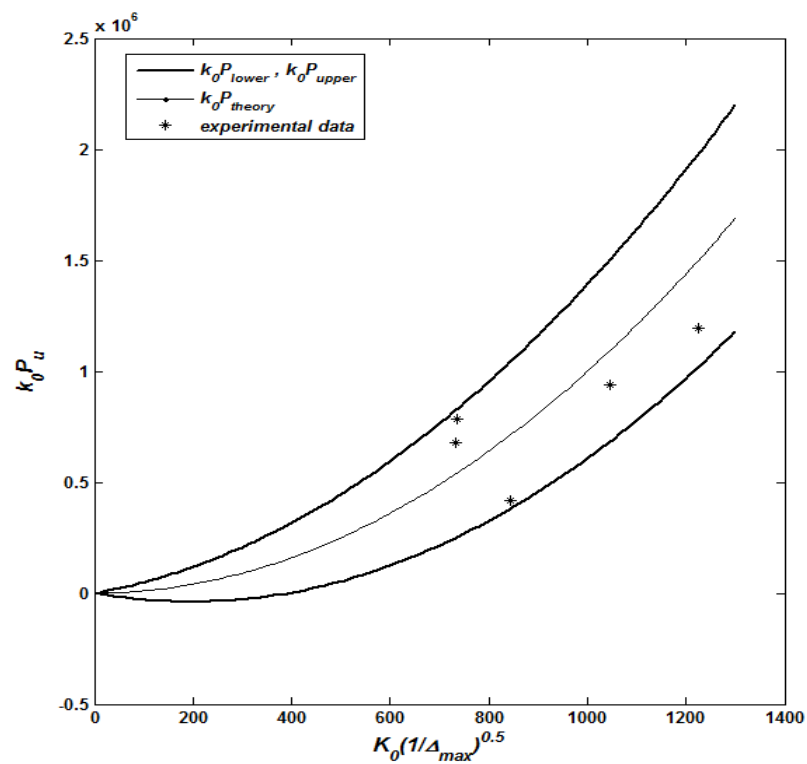
Figure 7.10 Application of experimental data from Wan et al. (2004) to find α

Table 7.3 **Specimens of Ouyang and Wan (2008) and their fracture energy boundaries**

Specimens	P_u (N)	Δ_{max} (mm)	(G_{fI}) (N/mm)	(G_{fI}) lower (N/mm)	(G_{fI}) upper (N/mm)	%
Control1	385.4	1.72	0.345	0.181	0.391	13.3
Control2	260.8	1.45	0.250	0.087	0.312	24.8
Control3	403.8	1.68	0.229	0.184	0.274	19.6
Control4	379.9	1.53	0.405	0.388	0.442	9.13
Control5	420.6	2.06	0.477	0.402	0.552	15.7
Control6	323.4	1.64	0.422	0.331	0.513	21.5
Control7	309.8	2.04	0.374	0.306	0.442	18.2
Control8	411.1	2.15	0.400	0.332	0.468	17.0
					Average (%)	17.4
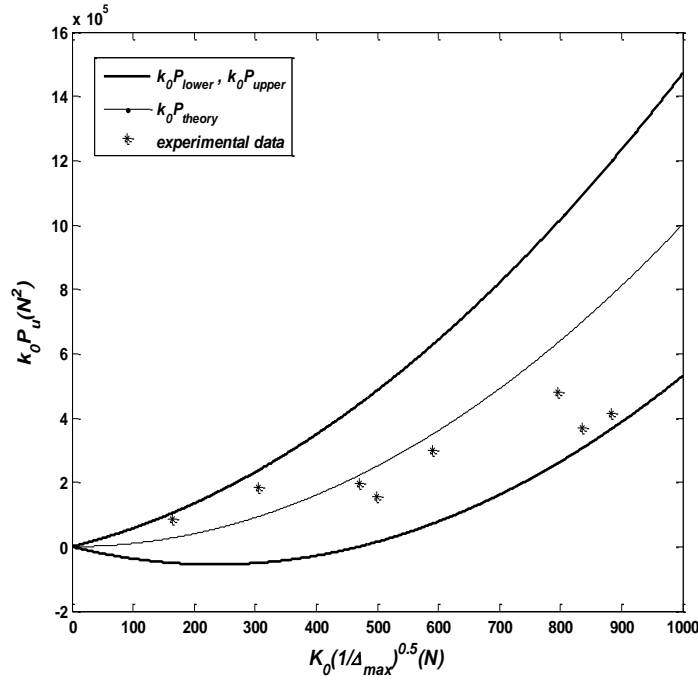
Figure 7.11 Application of experimental data from Ouyang and Wan (2008) to find α

Because P_u (peak load) is between P_{upper} and P_{lower} at Δ_{max}, using Equations 7.16 and 7.17, the bounds of interfacial mode I fracture energy, $(G_{fI})_{exp}$, with 95% probability can be expressed as:

$$\left(G_{fI} - \frac{1.96\alpha\sqrt{1/\Delta_{max}}}{2b_f a_{max}} \right) < (G_{fI})_{exp} < \left(G_{fI} - \frac{1.96\alpha\sqrt{1/\Delta_{max}}}{2b_f a_{max}} \right) \tag{7.18}$$

By using Equation 7.18 and the obtained values of α, the range of the bounds of

the mode I interfacial fracture energy has been determined for the applied experimental data. They are presented in Tables 7.2 and 7.3. It can be seen that on average, the actual fracture energy for test conducted by Wan et al. (2004) falls between 15.7% less or more than the theoretical value, while it is 17.4 % for tests conducted by Ouyang and Wan (2008).

According to Equation 7.16, the relationship between ultimate bearing load and interfacial mode I fracture energy is linear. Figure 7.12 shows the experimental ultimate load against analytical ones for specimens in Wan et al. (2004) and Ouyang and Wan (2008). In this figure, the thick lines are bounds of experimental maximum load vs. theoretical one, i.e., $P_{ex} = (1 \pm 0.174)P_{th}$. As it can be seen, all experimental ultimate loads are within the bounds. Therefore, it confirms that the proposed method can predict the load capacity variation of the specimens subjected to Mode I loading.
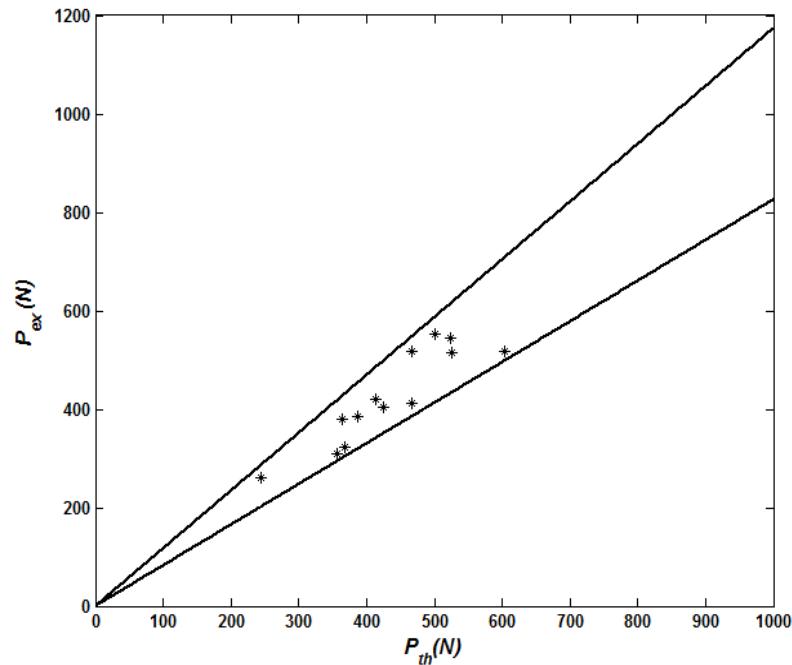
Figure 7.12 Experimental ultimate load vs. theoretical ones for the tests by Wan et al. (2004) and Ouyang and Wan (2008)

7.5 Conclusion of Brownian Motion Application

In this chapter, a systematic method is established to determine the range of interfacial fracture energy and load carrying capacity. Experimental data from literatures are used to demonstrate the validity of this method. For the experimental data used in this research, mode I and mode II interfacial fracture energy and load carrying capacity vary ± 17.4 % and $\pm 25.4\%$, respectively, away from their theoretical values.

Chapter 8 Conclusions and Future Research

The experimental, numerical and analytical studies are performed in this dissertation to model IC debonding failure in FRP-strengthened concrete beams. The summary, conclusions and future research are discussed in detail in this chapter.

8.1 Summary

The works completed in this dissertation include the following:

1. Proposed the application of the concrete damaged plasticity model in XFEM instead of regular FE technique to model the cracking behavior of concrete more efficiently;

2. Compared different FE methods to model FRP debonding failure of the FRP/concrete joints to find the most precise one using concepts of fracture mechanics;

3. Validated the numerical analysis by experimental data to determine the key parameters affecting IC debonding failure;

4. Experimentally studied FRP debonding from concrete substrate using the single shear pullout test to obtain the bond-slip relationship for the FRP/concrete interface;

5. Numerically investigated the behavior of the FRP/concrete interface to find failure mechanisms and critical stress state of the interface in the single shear pullout test;

6. Experimentally studied IC debonding failure in FRP-strengthened concrete beams

to obtain the bond-slip relationships;

7. Numerically investigated FRP-strengthened concrete beams to find failure mechanisms and critical stress state of the FRP/concrete interface;

8. Experimentally and numerically investigated the sensitivity of the IC debonding failure to the location of a major flexural/shear crack that triggers the initiation of the FRP debonding;

9. Numerically studied mixed-mode behavior of the FRP/concrete interface at the tip of the major/flexural crack;

10. And used concepts of Brownian motion and white noise to analytically find the load-carrying capacity variation due to the interfacial fracture energy variation in FRP/concrete joints.

Based on the experimental results and the corresponding numerical analyses, several fundamental conclusions can be made from this research and they will help in advancing the current understanding of failure mechanisms and key parameters of FRP debonding from cracked concrete beams.

8.2 Conclusions

Instead of using the concrete damaged plasticity model for the entire model in regular FE method, XFEM is also used for the concrete modeling to model its post-cracking behavior in this study. The concrete damaged plasticity model uses plastic theory and cannot model the discontinuities. The tension softening (post-cracking) behavior is modeled by enriching degrees of freedom of the elements in XFEM using concepts of fracture mechanics. Since the tensile cracking behavior of concrete controls

the behavior of concrete beams, using the combination of the concrete damaged plasticity model and XFEM helps to model the concrete cracking more efficiently.

The comparison of cohesive elements, VCCT, cohesive surface, and XFEM-based cohesive method for FRP debonding failure modeling shows that XFEM-based cohesive is the most practical and accurate method for the purpose of this study. In order to use this method, it is necessary to define a damage band as the crack domain and assign a traction-separation law to that. Numerical sensitivity analyses show that the FRP debonding behavior is sensitive to the FRP stiffness, the assigned traction-separation law to the damage band including bond strength, the interfacial fracture energy, and the ratio of shear modulus to damage band (FRP/concrete interface) thickness. According to the numerical analyses, thicknesses of 1 to 5 *mm* of damage band give the best agreement compared to the experimental results. It is confirmed in the literature, too.

The single shear pullout test is a common method to determine the bond-slip relationship (the traction-separation law in mode II direction) of the FRP/concrete interface. The conventional technique to get the bond-slip behavior from the pullout test results. However, this procedure results in a big scatter of bond-slip relationship and needs many strain gages bonded along the FRP sheet. Another applicable method to find the bond-slip from the pullout test results is Dai's approach that uses only the FRP strain and slip values at the tip of the pre-crack. Both of these two methods are applied in conducted the shear pullout tests in this study and the bond-slip relationship is obtained.

A numerical analysis using XFEM-cohesive based method is performed using the obtained bond-slip relation to model the single shear pullout test. The numerical results have a good agreement with the experimental results. The numerical sensitivity analysis

shows that the boundary condition of the concrete block at the force side plays a significant role in the bond-slip relationship and stress state of the FRP/concrete interface at the tip of the pre-crack in the single shear pullout tests. The single shear pullout test set-up in this study is designed in a way to have the closest boundary condition for the FRP/concrete interface to that in the beam specimens.

The main objective of this dissertation is to study failure mechanisms of IC debonding failure in FRP-strengthened concrete beams. Therefore, beam tests are carried out in order to reach the objective. In the beam specimens, a notch with half high of the beam cross section at the mid-span of the beam represents a main flexural/shear crack in the real beams in field. The comparison between strengthened control specimens and strengthened notched specimens shows that notched specimens can simulate the real beams. In all cases, there is a concrete wedge attached to the FRP after debonding failure that shows the initiation of debonding because of a diagonal crack formation close to the major flexural/shear crack inside the concrete. A 25 *mm* pre-crack is set at one side of the notch by hoping to control the FRP to debond at the pre-crack side. However, the debonding occurs randomly in either sides of the notch. This indicates that the pre-crack does not control the debonding initiation as assumed. The bond-slip relationship of the FRP/concrete interface in the beam specimens is obtained from FRP strain values recorded by strain gages.

FE analysis is performed for the FRP-strengthened concrete beam specimens by using the bond-slip relation obtained from the experimental tests. The applied numerical method is able to predict load vs. mid-span deflections and debonding processes, which are compatible with the experimental observations. According to the numerical analyses,

the diagonal crack in concrete is due to upward FRP vertical displacement at the tip of the notch. This phenomenon is the reason why the pre-crack does not control the FRP debonding initiation in the experimental tests.

The upward movement of the FRP plate at the tip of the notch is the different behavior of beam specimens than single shear pullout specimens. In shear specimens, the FRP plate is totally horizontal in the whole test process. However in beam specimens, the FRP plate rotates upward. The rotation of the FRP plate at the tip of the notch is due to the local moment created by the tension force in the FRP plate and the downward displacement of the concrete beam. The stress state at the FRP/concrete interface in beam specimens is different from that in shear specimens. Analysis shows that the bond strength in the beam specimens is smaller than that in pullout specimens even when the same boundary conditions are used.

In order to study IC debonding failure sensitivity to the location of the major flexural/shear crack, the notch is moved away from the mid-span to the supports of the beams in intervals of 51 *mm*. The concrete wedge is also observed after debonding due to the diagonal crack formation. When the notch reaches 153 *mm* away from the mid-span, it does not work as a major crack that initiates the FRP debonding. In this case, the debonding starts at the tip of a diagonal crack formed close to the mid-span flexural crack.

Numerical analysis shows that the diagonal crack forms in smaller longitudinal tensile stress and bigger shear stress as the notch is moved away from the mid-span. This is because of the decreasing of the moment/shear ratio when the notch is moved away from the mid-span. However, the longitudinal tensile stress drops to zero after the

diagonal crack initiation in all cases. Because of this reason, the obtained bond-slip relationship from beams with mid-span notch works in modeling IC debonding failure in beams with notches away from mid-span.

Although the FRP plate at the tip of the notch, which is not at the mid-span, has relative vertical displacement, the FE results show that FRP is not subjected to the assumed peeling stresses at the tip of the notch because of the local moment and upward moving of the FRP plate. Therefore, mode II loading still controls the FRP debonding in the mixed-mode loading cases.

According to the literature and numerical analysis in this study, two key parameters affecting the load carrying capacity of a bonded FRP/concrete joint are the FRP stiffness and concrete strength. In wet lay-up process, fiber sheets are soaked with polymer and applied to the concrete surface by hand. This causes relatively large variation in properties of the cured FRP composite material. In addition, the stiffness of FRP changes during debonding processes due to different amounts of concrete attached to the debonded FRP at different locations. It is also inevitable to have some variations in the strength of concrete. Therefore, the behavior of FRP-bonded concrete members varies among specimens even when the same materials are used. The variation of localized FRP stiffness and concrete strength is combined into a single parameter as the variation of localized interfacial fracture energy. In this study, the concepts of white noise and Brownian motion adopted from the probability theory are used to model the variation of interfacial fracture energy in FRP-bonded concrete specimens subjected to mode I and mode II loadings. A systematic method is established to determine the range of the interfacial fracture energy and load carrying capacity. Experimental data from literature

are used to demonstrate the validity of this method. For the experimental data used in this research, mode I and mode II interfacial fracture energy and load carrying capacity vary ±17.4 %and ±25.4%, respectively, away from their theoretical values.

8.3 Future Research

Since it is very difficult to match the line of the action of the applied tension force exactly with the center of the FRP in horizontal in single shear pullout tests in the lab, it causes many tested results cannot be used. Therefore, more specimens are needed to be tested in order to have more data to obtain more accurate bond-slip behavior.

Because the FRP debonding does not start from the tip of the major flexural/shear crack or notch in the beam specimens, and instead it starts from a diagonal crack close to the notch (about 25 *mm*) in random direction, it is recommended to simulate the diagonal crack along with the notch in beam specimens in order to control the debonding initiation and direction. It helps to attach the strain gages in locations at the debonding initiation points and through the pre-defined direction. The simulation of the diagonal crack along the notch can be done by placing steel or wooden plate in the shape that shown in Figure 8.1 in the forms before concrete pouring.
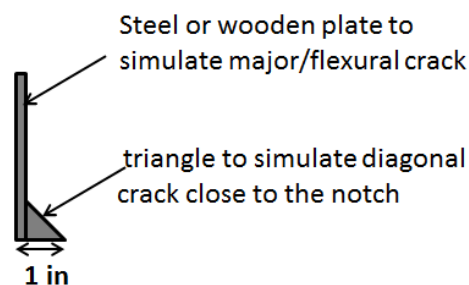

Steel or wooden plate to simulate major/flexural crack

triangle to simulate diagonal crack close to the notch

1 in

Figure 8.1 Steel or wooden plate to simulate the diagonal crack along with notch in beam specimens

Since the diagonal cracks observed in the experiments form inside the concrete through the width of the FRP plate, 2D analysis cannot model it efficiently. Three dimensional (3D) extended finite element analysis is able to calculate the strain distribution of FRP and stress state through the FRP/concrete interface width and model the diagonal cracks. Therefore, using 3D numerical analysis should produce more precious FRP debonding failure simulation. However, more calculation power is needed for the 3D analysis. Some supercomputing capacity is needed for this in the future research.

FRP is widely used to repair/strengthen concrete bridges, in which fatigue load should be considered in design. The models developed in this study are founded on quasi-static fracture test results. However, it would be interesting to conduct a study that focuses on the fatigue characteristics of the bond between FRP and concrete. It is well known that fatigue loads are much lower than static failure loads yield failures in adhesive joints. Therefore, future studies are needed to identify the primary mechanisms and the bond-slip behavior when the specimens are subjected to fatigue load.

Currently, many design equations or bond-slip models come from experimental data regression. Additional data will cause the change of some parameters in such equations. Using Brownian motion method proposed in this research, we can find a range for the interfacial fracture energy by using limited experimental test data. Then we can confidently predict the range of the interfacial fracture energy (with predefined confidence level, e.g., 95% in this study) in those untested specimens or in real structure using the same materials as those tested specimens. Then we may be able to avoid those parameters, which are simply obtained from data regression, in our design equation in

future. However, only linear relationship between load and deflection is used in this study to derive the governing equations for the Brownie motion. Nonlinear relationship should be considered in future research. Standard normal distribution of the data is assumed in this research, other distributions (e.g., Weibull distribution) are needed to be examined in future to better represent the real world situation.

BIBLIOGRAPHY

Abaqus/Standard User's Manual, (2013), *Dassault Systémes Simulia Corp.,* Providence, RI.

Abdelouahed, T. (2006) "Improved Theoretical Solution for Interfacial Stresses in Concrete Beams Strengthened with FRP Plate" *International Journal of Solids and Structures,* 43 (14-15): 4154 – 74.

ACI 318.R, (2013) "Building Code Requirements for Reinforced Concrete" *Reported by American Concrete Institute (ACI) Committee 318.*

ACI 440.2R, (2008) "Guide for the Design and Construction of Externally Bonded FRP Systems for Strengthening Concrete Structures" *Reported by American Concrete Institute (ACI) Committee 440.*

Aprile, A., Spacone, E. and Limkatanyu S. (2001) "Role of Bond in RC Beams Strengthened with Steel and FRP Plates" *Journal of Structural Engineering,* 127(12): 1445–52.

ASTM C39 (2010) "Standard Test Method for Compressive Strength of Cylindrical Concrete Specimens" *Book of ASTM Standards*, Vol.0402.

ASTM C78 (2010) "Standard Test Method for the Flexural Strength of Concrete (Using Simple Beam with Third Point Loading)" *Book of ASTM Standards*, Vol. 0402.

ASTM C496 (2010) "Standard Test Method for Splitting Tensile Strength of Cylindrical Concrete Specimens" *Book of ASTM Standards*, Vol. 0402.

Bakis, C.E., Bank, L.C., Brown, V.L., Cosenza, E., Davalos, J.F. and Lesko, J.J. (2002) "Fiber-Reinforced Polymer Composites for Construction State-of-the Art Review" *Journal of Composites for Construction,* 6(2):73–87.

Baky, A., Ebead, U.A. and Neale, K.W. (2012) "Nonlinear Micromechanics-Based Bond–Slip Model for FRP/Concrete Interfaces" *Engineering Structures*, 39: 11-23.

Bank, L.C. (2006), Composites for Construction: Structural Design with FRP Materials, John Wiley & Sons. LTD., West Sussex, England.

Bazant, Z.P. and Becq-Giraudon, E. (2002) "Statistical Prediction of Fracture Parameters of Concrete and Implications for Choice of Testing Standard" Cement and Concrete Research, 32: 529–556.

Belytschko, T. and Black, T. (1999) "Elastic Crack Growth in Finite Elements with Minimal Remeshing" *International Journal for Numerical Methods in Engineering*, 45(5): 601- 620.

Benjeddou, O., Ouezdou, M.B. and Bedday, A. (2007) "Damaged RC Beams Repaired by Bonding of CFRP Laminates" *Construction and Building Materials*, 21(6): 1301-10.

Benvenuti, E., Vitarelli, O. and Tralli, A. (2012) "Delamination of FRP-Reinforced Concrete by Means of an Extended Finite Element Formulation" *Composites Part B: Engineering*, 43(8):3258-69.

Billingsley, P. (1986), *Probability and Measure*, Wiley, 2nd edition, New York.

Bizindavyi, L. and Neale, K.W. (1999) "Transfer Lengths and Bond Strengths for Composites Bonded to Concrete" *Journal of Composites for Construction*, 3(4): 153–60.

Brosens, K. and Gemert, D. (1997) "Anchorage Stresses between Concrete and Carbon Fiber Reinforced Laminates" *Non-Metallic (FRP) Reinforcement for Concrete Structures, Proceedings of Third International Symposium*, 271-278.

Buyukozturk, O., Gunes, O. and Karaca, E. (2004) "Progress on Understanding Debonding Problems in Reinforced Concrete and Steel Members Strengthened Using FRP Composites" *Construction and Building Materials,* 18(1): 9–19.

Chajes, M.J., Finch, W.W., Januszka, T.F. and Thomas, T.A. (1996) "Bond and Force Transfer of Composite Material Plates Bonded to Concrete" *ACI Structural Journal,* 93(2): 208–217.

Chang, X., Wang, Q. and Zhang, P. (2012) "Modeling of Single-Flexural Crack Induced Debonding of FRP Plate Strengthened Concrete Beams Based on an Assumption of Heterogeneity" *Composites Part B: Engineering,* 43(3): 1598-1603.

Chen, J. and Teng, J. (2001) "Anchorage Strength Models for FRP and Steel Plates Bonded to Concrete" *Journal of Structural Engineering*, 127(7): 784–791.

Chen, J., Yang, Z. and Holt, G. (2001) "FRP or Steel Plate-to-Concrete Bonded Joints: Effect of Test Methods on Experimental Bond Strength" *Steel and Composite Structures*,1(2): 231–244.

Coronado, C. and Lopez, M. (2008) "Experimental Characterization of Concrete-Epoxy Interfaces" *Journal of Materials in Civil Engineering*, 20(4): 303-312.

Dai, J., Ueda, T. and Sato, Y. (2005) "Development of the Nonlinear Bond Stress-Slip Model of Fiber Reinforced Plastics Sheet-Concrete Interface with a Simple Methods" *journal of composites for construction*, 9(1): 52-62.

Dai, J., Wan, B., Yokota, H. and Ueda, T. (2009) "Fracture Criterion for Carbon Fiber Reinforced Polymer Sheet to Concrete Interface Subjected to Coupled Pull-out and Push-off Actions" *Advances in Structural Engineering*,12(5): 663-682.

Drucker, D.C. and Prager, W. (1952) "Soil mechanics and Plastic Analysis for Limit Design" *Quarterly of Applied Mathematics*, 10(2): 157–165.

Einstein, A. (1905) "On the Movement of Small Particles Suspended in a Stationary Liquid Demanded by the Molecular-Kinetic Theory of Heat" *Annual Physics*, 17.

Faella, C., Martinelli, E. and Nigro, E. (2008) "Formulation and Validation of a Theoretical Model for Intermediate Debonding in FRP-Strengthened RC Beams" *Composites Part B: Engineering*, 39 (4): 645-655.

Ferracuti, B., Savoia, M. and Mazzotti, C. (2007) "Interface Law for FRP–Concrete Delamination" *Composite Structures*, 80: 523–531.

FHWA, (2011) "Bridge Preservation Guide" *Publication Number: FHWA-HIF-11042.*

Fib-CEB-FIP. (2001) "Externally Bonded FRP Reinforcement for RC Structures" *Technical report bulletin 14, Task gruop9.*

Fukuzawa, K., Numao, T., Wu, Z., Yoshizawa, H. and Mitsui, M. (1997) "Critical Strain Energy Release Rate of Interface Debonding between Carbon Fiber Sheet and Mortar" *Non-Metallic (FRP) Reinforcement for Concrete Structures*, Vol. 1: 295–301.

Gartner, A.L., Douglas, E.P., Dolan, C.W. and Hamilton, H.R. (2011) "Small Beam Bond Test Method for CFRP Composites Applied to Concrete" *ASCE Journal of Composites for Construction*, 15(1): 52-61.

Gunes, O., Buyukozturk, O. and Karaca, E. (2009) "A Fracture-Based Model for FRP Debonding in Strengthened Beams" *Engineering Fracture Mechanics*, 76(12): 1897-1909.

Harries, K., Eveslage, T., Aidoo J. and Bro W. (2010) "Towards a Standard Test Method for Assessing FRP to Concrete Bond Characteristics" *CICE 2010, The 5th international conference on FRP composites in civil engineering*, Sep 27-29, Beijing, china.

Harries, K., Hamilton, H.R., Kasan J. and Tatar, J. (2012) "Development of Standard Bond Capacity Test for FRP Bonded to Concrete" *6th international conference on Fiber Reinforced Polymer (FRP) Composites in Civil Engineering (CICE)*, Rome, Italy.

Higham, D.J. (2001) "An Algorithmic Introduction to Numerical Simulation of Stochastic Differential Equations" *SIAM Review 200*, 43(3): 525-545.

Hillerborg, A., Modeer, M. and Petersson, P. (1976). "Analysis of Crack Formation and Crack Growth in Concrete by Means of Fracture Mechanics and Finite Elements" *Cement and Concrete Research,* 6(6): 773-782.

Hollaway, L C. (2010), *Applications of Fiber-Reinforced Polymer Composite Materials in ICE Manual of Construction Materials: Polymers and Polymer Fiber Composite*, Thomas Telford Limited, London: 109-127.

Karbhari, V.M. and Engineer, M. (1996) "Investigation of Bond between Concrete and Composites: Use of a Peeling Test" *Journal of Reinforced Plastics and Composites*,15: 208–227.

Karbhari, V.M., Niu, H. and Sikorsky, C. (2006) "Review and Comparison of Fracture Mechanics-Based Bond Strength Models for FRP-Strengthened Structures*" Journal of Reinforced Plastics and Composites,* 25(17): 1757–94.

Kosmatka, S.H., Kerkhoff, B. and Panvarease, W.C. (2002), *Design and Control of Concre Mixtures*, 14th Edition, EB001.14T, Portland Cement Association, Skokie, IL.

Krueger, R. (2004) "Virtual Crack Closure Technique: History, Approach, and Applications" *Applied Mechanics Reviews*, 57 (2): 109-143.

Lee, J. and Fenves, L.G. (1998) "Plastic-Damage Concrete Model for Earthquake Analysis of Dams" *Earthquake Engineering Structure Dynamics*, 27(9): 937–956.

Leung, C.K.Y. and Tung, W.K. (2006) "Three-Parameter Model for Debonding of FRP Plate from Concrete Substrate" Journal of Engineering Mechanics, 132(5):509–518.

Liu, S.T., Oehlers, D.J. and Seracino, R. (2007) ''Study of Intermediate Crack Debonding in Adhesively Plated Beams'' Journal of Composites for Construction, 11(2): 175-183.

Lu, X.Z., Teng, J.G., Ye, L.P. and Jiang, J.J. (2005) "Bond–Slip Models for FRP Sheets/Plates Bonded to Concrete*" Engineering Structures*, 27: 920–937.

Lu, X.Z., Teng, J.G., Ye, L.P. and Jiang, J.J. (2007)" Intermediate Crack Debonding in FRP-Strengthened RC Beams: FE Analysis and Strength Model" *Journal of Composites for Construction,* 11(2): 161–74.

Lubliner, J., Oliver, J., Oller, S. and Onate, E. (1989) "Plastic-Damage Model for Concrete" *International Journal of Solid Structure*, 25(3): 299–326.

MacGregor, J.G. and Bartlett, F.M. (1999), *Reinforced Concrete: Mechanism and Design,* Pearson Education, 1th edition, Canada.

Mazzotti, C., Savoia, M. and Ferracuti, B. (2008) "An Experimental Study on Delamination of FRP Plates Bonded to Concrete" *Construction and Building Materials*, 22: 1409–1421.

Meier, U. (1995) "Strengthening of Structures Using Carbon Fiber/Epoxy Composites" *Construction and Building Materials*, 9(6): 341-405.

Melenk, J.M. and Babuöka, I. (1996) "The Partition of Unity Finite Element Method: Basic Theory and Applications" *Computer Methods in Applied Mechanics and Engineering*, 139: 289-314.

Moës, N., Dolbow,J. and Belystschko, T. (1999) "A Finite Element Method for Crack Growth without Remeshing" *International Journal for Numerical Methods in Engineering,* 46(1): 131-150.

Nakaba, K., Kanakubo, T., Furuta, T. and Yoshizawa, H. (2001) "Bond Behavior between Fiber-Reinforced Polymer Laminates and Concrete" *ACI Structural Journal*, 359-367.

Niu, H., Karbhati, V.M. and Wu Z. (2006) "Diagonal Micro-Crack Debonding Mechanisms in FRP Rehabitation Concrete" *Composites: Part (B)*, 37: 627-641.

Obaidat, Y.T., Heyden, S. and Dahlblom, O. (2010) "The Effect of CFRP and CFRP/Concrete Interface Models When Modelling Retrofitted RC Beams with FEM" *Composite Structures*, 92(6): 1391-98.

Oehlers, D.J. and Seracino R. (2004), *Design of FRP and Steel Plated RC Structures: Retrofitting Beams and Slabs for Strength, Stiffness and Ductility,* Elsevier LTD. Oxford, England.

Øksendal, B. (2003), *Stochastic Differential Equations, an Introduction with Applications*, Springer-Verlag, 6th edition, Berlin.

Ouyang, Z., Wan B. (2008) "Experimental and Numerical Study of Water Effect on Bond Fracture Energy between FRP and Concrete in Moist Environments" *Journal of Reinforced Plastics and Composites*, 27(2): 205-223.

Pan, J. and Leung, C.K. (2007) "Debonding Along the FRP–Concrete Interface under Combined Pulling/Peeling Effects" *Engineering Fracture Mechanics*, 74(1-2): 132-150.

Popovics, S. (1973) "A Numerical Approach to the Complete Stress–Strain Relation for Concrete" *Cement Concrete Research,* 3(5): 583–599.

Rabinovitch, O. (2008) "Debonding Analysis of Fiber-Reinforced-Polymer Strengthened Beams: Cohesive Zone Modeling Versus a Linear Elastic Fracture Mechanics Approach" *Engineering Fracture Mechanics*,75(10): 2842-59.

Remmers, J. J. C., Borst, R. and Needleman, A. (2008) "The Simulation of Dynamic Crack Propagation using the Cohesive Segments Method" *Journal of the Mechanics and Physics of Solids*, 56(1): 70–92.

Rosenboom, O. and Rizkalla, S. (2008) "Modeling of IC Debonding of FRP-Strengthened Concrete Flexural Members" *Journal of Composites for Construction,* 12(2): 168–179.

Serbescu, A., Guadagnini, M. and Pilakoutas, K. (2013) "Standardized Double-Shear Test for Determining Bond of FRP to Concrete and Corresponding Model Development" *Composites Part B: Engineering,* 55: 277-297.

Shah, S.P. and McGarry, F.J. (1971) "Griffith Fracture Criterion and Concrete" *Journal of the Engineering Mechanics Division*, 97: 1663-1676.

Shah S.P, Swartz S.E. and Ouyang C. (1995), *Fracture Mechanics of Concrete: Applications of Fracture Mechanics to Concrete, Rock, and other Quasi-brittle Materials*, John Wiley & Sons. LTD., New York.

Song, J. H., Areias, P.M. and Belytschko, T. (2006) "A Method for Dynamic Crack and Shear Band Propagation with Phantom Nodes" *International Journal for Numerical Methods in Engineering*, 67(6): 868–893.

Taljsten, B. (1997) "Defining Anchor Lengths of Steel and CFRP Plates Bonded to Concrete" *International Journal of Adhesion and Adhesives*, 17(4): 319–327.

Teng, J.G., Chen, J.F., Smith, S.T. and Lam, L. (2002), *FRP-Strengthened RC Structures,* John Wiley & Sons. LTD. West Sussex, England.

Teng, J.G. and Chen, J.F. (2009) "Mechanics of Debonding in FRP-Plated RC Beams" *Structures and Buildings*, 162(5): 335–45.

Teng, J.G., Smith, S.T., Yao, J. and Chen, J.F. (2003) "Intermediate Crack-Induced Debonding in RC Beams and Slabs" *Construction and Building Materials*, 17(6-7): 447–462.

Teng, J.G. and Yao, J. (2007) "Plate End Debonding in FRP-Plated RC Beams—II: Strength model" *Engineering Structures*, 29(10): 2472-86.

Todeschini, C.E., Bianchini, A.C. and Kesler, C.E. (1964). "Behavior of Concrete Columns Reinforced with High Strength Steels" *Proceedings of the journal of American Concrete Institute (ACI)*, 61(6): 701-716.

Tounsi, A., Hassaine Daouadji, T., Benyoucef S. and Addabedia E.A. (2009) "Interfacial Stresses in FRP-Plated RC Beams: Effect of Adhered Shear Deformations" *International Journal of Adhesion and Adhesives*, 29 (4): 343 – 351.

Toutanji, H., Han, M. and Ghorbel, E. (2012) "Interfacial Bond Strength Characteristics of FRP and RC Substrate" *Journal of Composites for Construction,* 16(1): 35–46.

Toutanji, H., Ueno, S. and Vuddandam, R. (2013) "Prediction of the Interfacial Shear Stress of Externally Bonded FRP to Concrete Substrate Using Critical Stress State Criterion" *Composite Structures,* 95: 375 – 380.

Wan, B., Sutton, M.A., Petrou, M.F., Harries, K. and Li, N. (2004) "Investigation of Bond between Fiber Reinforced Polymer and Concrete Undergoing Global Mixed-Mode

I/II Loading" *Journal of Engineering Mechanics,* 103 (12): 1467–75.

Wiener, N. (1923) "Differential Spaces" *Journal of Mathematical Physics*, 58: 131-174.

Wight, J.K. and MacGregor, J.G. (2012), *Reinforced Concrete: Mechanism and Design,* Pearson Education, 6th edition, New Jersey.

Wittmann, F.H. (2002) "Crack Formation and Fracture Energy of Normal and High Strength Concrete" *Sadhana (India),* 27(4): 413-423.

Wu, E.M. and Reuter R.C. (1965) "Crack Extension in Fiberglass Reinforced Plastics" *T&A. M Report*, University of Illinois, No.275.

Yao, J. and Teng, J.G. (2007) "Plate End Debonding in FRP-Plated RC Beams—I: Experiments" *Engineering Structures,* 29: 2457–71.

Yoshizawa, H., Wu, Z., Yuan, H. and Kanakubo, T. (2000) "Study on FRP-Concrete Interface Bond Performance" *Transactions of Japanese Society of Civil Engineering*, No.662/V-49: 105-119.

Yuan, H., Teng, J.G., Seracino, R., Wu, Z.S. and Yao, J. (2004) "Full-range Behavior of FRP-to-Concrete Bonded Joints" *Engineering Structures*, 26(5): 553–565.

Yuan, H., Lu, X., Hui, D. and Feo, L. (2012) "Studies on FRP-concrete Interface with Hardening and Softening Bond-Slip Law" *Composite Structures*, 94 (12): 3781-92.